

THE RESPONSE OF STREAMFLOW AND EVAPOTRANSPIRATION TO CHANGES IN  
SNOWMELT ACROSS THE WESTERN UNITED STATES

by

THEODORE BASILE BARNHART

B.A., Whitman College, 2010

M.S., Idaho State University, 2013

A dissertation submitted to the  
Faculty of the Graduate School of the  
University of Colorado for the degree of

Doctor of Philosophy

Department of Geography

2018

This dissertation for the Doctor of Philosophy entitled:  
The Response of Streamflow and Evapotranspiration to Changes in Snowmelt Across the  
Western United States

written by Theodore Basile Barnhart  
has been approved for the Department of Geography

---

Noah P. Molotch

---

Suzanne P. Anderson

---

Peter D. Blanken

---

Ben Livneh

---

Roger C. Bales

---

Date

The final copy of this dissertation has been examined by the signatories,  
and we find that both the content and the form meet acceptable presentation standards  
of scholarly work in the above mentioned discipline.

## ABSTRACT

Barnhart, Theodore Basile (Ph.D., Geography)

The Response of Streamflow and Evapotranspiration to Changes in Snowmelt Across the  
Western United States

Dissertation directed by Associate Professor Noah P. Molotch

Mountain regions disproportionately produce streamflow for downstream ecosystems and communities. In the western United States this snowmelt derived water is valued in the trillions of dollars. Given the high value of snowmelt-derived water, understanding how streamflow production and vegetation water use from mountain regions may change is of critical importance. Snowmelt rate, timing, and amount are forecast to change under future climate, potentially altering streamflow and evapotranspiration patterns. This dissertation investigates the relationship between snowmelt rate, timing, and amount and runoff or streamflow at the plot and regional scales across the western United States. Additionally, the effects of future land cover, precipitation, and air temperature changes on streamflow from a headwaters catchment are investigated.

At the plot scale, observations and hydrologic modeling were used to investigate how changes in snowmelt rate, timing, and amount affect snowmelt season runoff production and subsurface water storage in Colorado (CO) and California (CA). The snowmelt modeling experiment was designed to eliminate the observed multicollinearity between snowmelt rate, timing, and amount. Results indicate that runoff was most

sensitive to snowmelt timing and rate at CO and CA, respectively (sensitivity = -0.31 vs. 0.22 and sensitivity = -0.31 vs. 0.67 for snowmelt timing vs. rate, respectively). Snowmelt season changes in subsurface storage were most sensitive to snowmelt timing at both CO and CA (sensitivity = -0.24 vs. 0.18 and sensitivity = -0.474 vs. 0.466 for snowmelt timing vs. rate, respectively).

At the watershed scale, the Landscape Disturbance and Succession (LANDIS) land cover evolution model was used in conjunction with the Regional Hydro-Ecologic Simulation System (RHESSys) to investigate how changes in climate and land cover may alter streamflow from 2000 to 2100 in a catchment on the Colorado Front Range. As forest cover in the catchment increased, counter intuitively, the simulated streamflow also increased by 29-44% by 2100 driven by reductions in wind-scour of snow out of the catchment and decreases in evapotranspiration. These changes in streamflow were partially attributed to land cover change but also to air temperature driven changes in snowmelt timing.

At the regional scale, a long-term hydrometeorology data set was used to elucidate a possible mechanism linking snowmelt rate to streamflow production. An ensemble of Budyko streamflow anomalies (BSA), a measure of streamflow production, at ~20,000 Variable Infiltration Capacity model grid cells was computed. BSA was correlated with simulated baseflow efficiency ( $r^2=0.64$ ) and snowmelt rate ( $r^2=0.42$ ). A strong correlation between snowmelt rate and baseflow efficiency ( $r^2=0.73$ ) links these relationships and supports a possible streamflow generation mechanism wherein greater snowmelt rates increase subsurface flow and streamflow production.

## ACKNOWLEDGEMENTS

This work would not have been possible without the support of my family and friends. In particular I would like to thank my fiancé Metta Gilbert and our dog Osa for tolerating my obsession with snowmelt and for being great companions on many adventures. Thank you to the friends and colleagues I have made in the Mountain Hydrology Group, the Geography department, and Boulder, Colorado. This support network was critical to my success.

Thank you to my advisor Noah Molotch for his guidance throughout my dissertation and to my dissertation committee members Ben Livneh, Suzanne Anderson, Peter Blanken, and Roger Bales for their thoughtful comments and support of my work. I am grateful for Adrian Harpold, Dominik Schneider, Emily Baker, Taylor Winchell, John Knowles, and Keith Jennings for acting as sounding boards throughout my time at the University of Colorado. Lastly, thank you to my coauthors Christina Tague, John Knowles, Ben Livneh, Noah Molotch, Adrian Harpold, Dominik Schneider, Jelena Vukomanovic, and Patrick Bourgeron for their help on the three projects that comprise this dissertation.

The work presented herein was supported by and used data sets made possible by the following: USDA - NSF Water Sustainability and Climate Grant (2012-67003-19802), NSF Boulder Creek CZO (EAR-9810218), NSF Hydrological Sciences (EAR-1141764), NSF (EAR-1144894), USDA NIFA (NEV05293), NSF Niwot Ridge LTER (DEB-1027341), the Ameriflux Network, the USDA-NRCS SnoTel network, the National Oceanic and Atmospheric Administration Climate Reference Network, a CUAHSI Pathfinder Fellowship, the James A. and Jeanne B. DeSana Graduate Research Scholarship, and the University of Colorado Geography Department Gilbert White Fellowship.

## TABLE OF CONTENTS

Chapter 1: Introduction	1
1.1 Context for the Dissertation	1
1.1.1 Problem Statement	3
1.1.2 Research Objectives and Design	4
1.2 Summary	8
Chapter 2: The Influence of Snowmelt Rate and Timing on Runoff Generation	10
Abstract	10
2.1 Introduction	11
2.2 Study Areas	14
2.3 Methods	16
2.3.1 Observational Analysis	19
2.3.2 Hydrologic Model Setup and Calibration	22
2.3.3 Hydrologic Model Experiment Snowmelt Scenario Design	24
2.3.4 Hydrologic Model Experiment Analysis	28
2.4 Results	29
2.4.1 Observed Relationships	29
2.4.2 Hydrologic Model Calibration	31
2.4.3 Snowmelt Modeling Experiment	33
2.4.4 Changes in Snowmelt Season Subsurface Storage	38
2.5 Discussion	40
2.6 Conclusion	44
Chapter 3: Future Land Cover and Climate Drive Decreases in Snow Scour and Transpiration, Increasing Streamflow	47
Abstract	47
3.1 Introduction	48
3.2 Methods	51
3.2.1 Site Description	52
3.2.2 LANDIS-II Land Cover Simulations	54
3.2.3 RHESSys Hydrologic Modeling	56
3.2.4 Modeling Experiment Design	64
3.3 Results	67
3.3.1 Model Calibration	67
3.3.2 Changes in Catchment Land Cover	67
3.3.3 Coupled Land Cover, Precipitation, and Air Temperature Changes	68
3.3.4 Current Land Cover with Precipitation Changes	74
3.3.5 Current Land Cover with Air Temperature Changes	75
3.3.6 Current Land Cover, Future Precipitation, and Future Temperature	76
3.3.7 Comparison of Scenarios	78
3.4 Discussion	79
3.4.1 Coupled Land Cover, Precipitation, and Air Temperature Changes	79
3.4.2 Changes in Streamflow	80
3.4.3 Changes in Evapotranspiration	81
3.4.4 Implications	83
3.5 Conclusion	85
Chapter 4: Snowmelt Rate Dictates Streamflow	88
Abstract	88

4.1 Introduction	89
4.2 Data and Domain	91
4.3 Methods	93
4.3.1 Snowmelt rate	94
4.3.2 The Budyko Framework	94
4.3.3 Regional Analysis	97
4.3.4 Model Validation	97
4.4 Results	98
4.4.1 Snowmelt Rate Controls Hydrologic Partitioning	98
4.4.2 Regional Sensitivity to Changes in Snowmelt Rate	101
4.5 Discussion	103
4.5.1 Snowmelt Rate Controls Hydrologic Partitioning	103
4.5.2 Regional Sensitivity to Changes in Snowmelt Rate	105
4.5.3 Snowmelt rate and snowfall fraction	107
4.6 Conclusion	108
Chapter 5: Conclusion	110
5.1 Review of Findings	110
5.2 Avenues for Future Work	116
Bibliography	118
Appendix A: Chapter 2 Supporting Information	129
A.1 Calculation of Plant Available Water Storage	129
Appendix B: Chapter 4 Supporting Information	130
B.1 Introduction	130
B.2 Snow Fall Fraction Calculation	130

## LIST OF TABLES

Table 2.1: Instrumentation used.	21
Table 2.2: Observed runoff ratios.	30
Table 2.3: Observed runoff ratio sensitivity to snowmelt.	31
Table 2.4: Optimal parameters and performance statistics.	33
Table 2.5: Simulated evapotranspiration totals.	34
Table 3.1: Model optimization parameters.	64
Table 3.2: Model experiment scenarios.	66
Table 3.3: Comparison of model experiment results.	70
Table B.1: Ensemble fitting parameters and statistics.	134
Table B.2: Budyko streamflow anomaly – snowmelt rate relationship parameters.	134
Table B.3: Budyko streamflow anomaly – baseflow relationship parameters.	135
Table B.4: Budyko streamflow anomaly – snowmelt rate relationship parameters by ecoregion.	136
Table B.5: Fitted Budyko curve parameters and mean snowmelt rate by ecoregion.	139
Table B.6: Snowfall fraction – Budyko streamflow anomaly relationship parameters.	139

## LIST OF FIGURES

Figure 2.1: Location map.	15
Figure 2.2: Precipitation climatology.	16
Figure 2.3: Geometric simplification of niveographs.	18
Figure 2.4: Observed and simulated snowpack variability at both sites.	26
Figure 2.5: Day of water year – snowmelt rate relationships.	27
Figure 2.6: Simulation optimization results.	32
Figure 2.7: Example experiment evapotranspiration time series.	34
Figure 2.8: Experiment runoff response surfaces.	36
Figure 2.9: Experiment multiple regression runoff analysis results.	37
Figure 2.10: Multiple regression analysis sensitivity to plant available water storage.	38
Figure 2.11: Experiment change in subsurface storage response surface.	39
Figure 2.12: Experiment multiple regression change in storage analysis results.	40
Figure 3.1: Study location.	53
Figure 3.2: Elevation and vegetation controls on solid precipitation.	60
Figure 3.3: Analysis of changes in catchment subsurface storage.	62
Figure 3.4: Hydrologic model optimization.	67
Figure 3.5: Future changes in catchment land cover.	68
Figure 3.6: Simulated future precipitation.	69
Figure 3.7: Simulated future mean peak snow water equivalent.	71
Figure 3.8: Simulated future runoff ratios.	72
Figure 3.9: Simulated future monthly streamflow and evapotranspiration.	73
Figure 3.10: Simulated future changes to monthly streamflow and evapotranspiration.	74
Figure 3.11: Simulated streamflow and evapotranspiration with only future air temperature.	76
Figure 3.12: Monthly streamflow and evapotranspiration with current land cover and future air temperature and precipitation.	77
Figure 3.13: Simulated future vapor fluxes.	82
Figure 3.14: Simulated changes to monthly transpiration and evaporation.	83
Figure 4.1: Analysis domain and ecoregion location map.	93
Figure 4.2: Whole-domain relationships.	99
Figure 4.3: Regional analysis relationships.	102
Figure B.1: Example Budyko analysis methods.	131
Figure B.2: Comparison with other data sets.	132
Figure B.3: Snowfall fraction – Budyko streamflow anomaly relationship.	132
Figure B.4: Snowfall fraction – snowmelt rate relationship.	133

# Chapter 1: Introduction

## 1.1 Context for the Dissertation

Globally, mountainous areas contribute disproportionately to streamflow, often in the form of snowmelt [Barnett *et al.*, 2005; Viviroli *et al.*, 2007]. Streamflow from mountain regions represents the majority of global renewable freshwater [Vörösmarty *et al.*, 2005]. This snowmelt-derived streamflow provides a necessary resource to one-sixth of the global population [Barnett *et al.*, 2005]. In addition to their water resources, mountain regions, especially in the Western United States, serve as carbon sinks [Schimel *et al.*, 2002]. Given the ecosystem services that mountain regions supply to downstream communities, understanding how streamflow will change from these regions in the future is important as mountain systems are bellwethers for environmental change [Williams *et al.*, 2011].

In the western United States, 60 million people rely on snowmelt for drinking water, agricultural, industrial, and recreational uses [Bales *et al.*, 2006]. The mountain snowpack provides natural storage of winter precipitation for spring and summer, when water demand is greatest [Mote *et al.*, 2005]. Thus, winter snowpack acts to synchronize water availability and water demand. Climate change is shifting the timing of spring snowmelt and streamflow earlier in the year [Cayan *et al.*, 2001; Stewart *et al.*, 2005]. This has implications for the amount and intensity of streamflow and could reduce the margin of acceptable error in reservoir management [Stewart *et al.*, 2004]. The western United States may experience a 2-7 °C temperature increase by 2100 [IPCC, 2014], which could profoundly alter snowpack magnitude, snowmelt timing, and snowmelt rate in

mountainous regions [Musselman *et al.*, 2017]. Additionally, climate warming driven shifts in land cover have the potential to decrease streamflow due to tree-line expansion at high elevations [Goulden and Bales, 2014] and shrub conversion at lower elevations [Bart *et al.*, 2016; Rother and Veblen, 2016]. These trends necessitate the study of how climate warming induced changes in snow hydrology and land cover will cascade to changes in forest water use (evapotranspiration, ET) and streamflow (Q). Furthermore, non-stationarity in hydrologic systems, induced by climate warming, necessitates improved process understanding through the use of both observational studies and process based hydrologic modeling to inform both water resources and land management decisions [Milly *et al.*, 2008].

Many studies have shown that the onset of spring is occurring earlier in the year [Cayan *et al.*, 2001; Stewart *et al.*, 2005] and that these changes can be attributed to warming in the winter and spring [Stewart *et al.*, 2005]. Similarly, the proportion of precipitation that falls as snow is in decline across the western United States and this decline is attributable to increases in storm minimum temperatures during the winter months [Knowles *et al.*, 2006]. These trends suggest that mountain snowpacks with temperatures close to freezing will be most sensitive to warming [Knowles *et al.*, 2006; Nolin and Daly, 2006]; however, trends in snow water equivalent from Colorado and the intermountain western United States suggest that cold, continental snowpacks are melting earlier due to warmer air temperatures as well [Clow, 2010; Harpold *et al.*, 2012].

Across the western United States there are consistent patterns linking peak snow water equivalent (SWE) to snowmelt rate and timing. Trujillo and Molotch [2014] show that, generally, a deep snowpack persists later into the spring and melts more rapidly than

a shallow snowpack, which melts earlier and more slowly. These differences are due to increased solar radiation driven snowmelt later in spring. When a shallow snowpack ripens early in the spring there is not as much available energy to drive melt, which then results in slower snowmelt [Trujillo and Molotch, 2014; Musselman et al., 2017]. This is because there is less radiative forcing earlier in the year when the sun is low in the sky [Trujillo and Molotch, 2014]. When these patterns are considered with the body of evidence describing earlier snowmelt and spring snowmelt driven streamflow, it suggests a close linkage between snowmelt rate and streamflow; however, the mechanism linking snowmelt to streamflow remains elusive.

### **1.1.1 Problem Statement**

As climate warming decreases the mountain snowpack, the importance of understanding the linkage between snowmelt and runoff production increases. The aim of this dissertation is to broadly investigate how changes in snowmelt are reflected in changes in streamflow and evapotranspiration at point, watershed, and regional scales. This line of questioning is complicated by inter-site heterogeneity, future changes in land cover, and regional differences in snowpack regimes. Each of these components is addressed by the following science questions: I) What is the relative influence of snowmelt rate, timing, and amount on runoff generation? II) How do changes in snowmelt and land cover affect streamflow in a snow-dominated headwaters catchment? And III), what are the regional differences in snowmelt rate - streamflow production relationships across the western United States? Throughout this dissertation, runoff will be used to describe water produced from small landscape elements such as modeling patches or grid cells less than 1 km<sup>2</sup> while

streamflow will be used to describe water produced from larger, integrating landscape elements such as catchments and land surface model grid cells greater than 1 km<sup>2</sup>.

### **1.1.2 Research Objectives and Design**

Science questions I-III listed above will be addressed via three tasks moving from the smallest analysis scale (I) to the largest (III). Task 1, investigates the roles of snowmelt rate, timing, and amount across two mountainous locations in the western United States using observations and a hydrologic modeling experiment designed to separate the multicollinearity of snowmelt rate, timing, and amount. Task 2, investigates the effects of changes in land cover and climate warming on streamflow production at a snow-dominated watershed on the Colorado Front Range. Task 3, investigates snowmelt controls on streamflow production at the regional scale across the western United States.

#### **Question I: What is the relative influence of snowmelt rate, timing, and amount on runoff generation?**

Snowmelt rate has been linked to streamflow production across the mountainous regions of the western United States [*Barnhart et al.*, 2016]. This relationship was determined using a hydrologic modeling data set spanning the continental United States; however, in natural systems, snowmelt rate, timing, and amount are interrelated [*Trujillo and Molotch*, 2014] making it difficult to statistically assess the influence of these components of snowmelt on snowmelt season runoff production. This portion of the dissertation seeks to disentangle the relationship between runoff and snowmelt rate, timing, and amount at two forested, snow-dominated sites in the western United States. I address this question by building one-dimensional Regional Hydro-Ecologic Simulation

System (RHESSys) [Tague and Band, 2004] model simulations for each site, forcing and calibrating each model using observational data, and applying a synthetic snowmelt experiment to each site.

The synthetic snowmelt experiments used snowmelt scenarios designed for each site based on snow pillow observations of snowmelt rate, timing, and amount. Constant probability distributions of snowmelt rate, timing, and amount were developed for each site and used to construct 10,000 snowmelt scenarios with no internal multicollinearity. These scenarios were used as input for the calibrated, one-dimensional implementations of RHESSys. Using snowmelt amount for normalization, simulation output was analyzed to understand the influence of snowmelt rate and timing on snowmelt season runoff production as well as the snowmelt season change in subsurface storage, as this quantity is important for sustaining late-season streamflow and vegetation productivity.

## **Question II: How do changes in snowmelt and land cover affect streamflow in a snow-dominated headwaters catchment?**

Colorado is expected to experience an annual average 2.5-5 °C increase in air temperature by 2050 and potentially a slight increase in precipitation, although the anticipated change in precipitation is more poorly constrained [Lukas *et al.*, 2014]. These forecasted changes in air temperature and precipitation will impact the proportion of precipitation falling as snow, snowpack accumulation, and snowmelt across the region [Rasmussen *et al.*, 2011]. Additionally, the pattern of vegetation cover in the region may also change in response to more mild temperatures and changes in precipitation [Harsch *et al.*, 2009]. In this portion of the dissertation I investigate how changes in snowmelt, driven

by warmer air temperatures and altered precipitation, interact with simulated futures of land cover for a headwater catchment on the Colorado Front Range that spans the alpine – subalpine transition.

To carry out this investigation, I created a RHESSys [Tague and Band, 2004] model simulation for Como Creek, a 5.0 km<sup>2</sup> headwaters catchment on the Colorado Front Range, and calibrated the simulation using streamflow observations. Land cover futures were generated from the LANdscape DIsturbance and Succession (LANDIS-II) model [Scheller and Mladenoff, 2004] every decade from calendar year 1990 through 2100 using two forcing tracks. Both forcing tracks include a 4 °C/century increase in air temperature with one track experiencing a 15% increase in precipitation by 2100 and the other track experiencing a 15% decrease in precipitation by 2100. The first ten years of the LANDIS-II simulation are considered model spin up and as such year 2000 is considered as control for this experiment. As LANDIS-II is a stochastic model, three iterations of the model were used for each forcing track. Land cover and biomass from the LANDIS-II simulations were converted into maps of land cover type and leaf area index for ingestion into the RHESSys model.

Regional Hydro-Ecologic Simulation System instances were run using a gridded meteorology forcing data set for water year 1991 through water year 2012 with air temperature and precipitation inputs matched to the perturbations used to generate the LANDIS-II land cover futures. The first two water years of each hydrologic model simulation were omitted to allow model stores to spin-up. These simulations were used as part of a larger model experiment with simulations where only air temperature and

precipitation were altered to separate changes in streamflow due to land cover change from streamflow changes due to increased air temperature and precipitation change.

**Question III: what are the regional differences in snowmelt rate - streamflow production relationships across the western United States?**

Across the western United States, much of the streamflow used for irrigation, municipal use, ecological flows, and recreation is sourced from snowmelt [*Bales et al., 2006*]. Understanding controls on streamflow production at broad spatial scales is important as this may identify broad hydrologic relationships as well as differential sensitivities in streamflow production to environmental change at spatial scales relevant to land management. Recent work has shown a relationship between the proportion of precipitation falling as snow versus rain and climate corrected streamflow production across the United States [*Berghuijs et al., 2014*]; however, this relationship lacks an explanatory mechanism. In this portion of the dissertation I seek to elucidate a mechanistic control between snowmelt and streamflow production in the mountainous ecoregions of the western United States [*Commission for Environmental Cooperation, 2006*].

To investigate the relationship between snowmelt and streamflow I used a Variable Infiltration Capacity [*Liang et al., 1994*] model-based hydrometeorology modeling data set [*Livneh et al., 2015*] subset to the ten mountainous ecoregions of the western United States that produce much of the streamflow for the region. These data were used to compute an ensemble of Budyko style streamflow anomalies for the domain [*Zhou et al., 2015*], which represent the propensity of each grid cell to over or under produce streamflow within an available water and energy framework [*Budyko, 1974*]. I then developed relationships

between simulated snowmelt rate and the streamflow anomaly ensemble across the entire domain and for each of the component ecoregions within the domain. I also optimized the Zhang et al. [2001] Budyko-style equation for each ecoregion and compared the y-axis asymptotes of the optimized equations to the mean snowmelt rates of each ecoregion to confirm, via a different pathway, the linkage between snowmelt rate and streamflow production across the domain.

## **1.2 Summary**

Via the three tasks outlined above, this dissertation advances the understanding of how changes in snowmelt and land cover may alter water availability in the western United States. A variety of observations and numerical simulations are used to accomplish the three tasks and the scope of each science question increases in scale from the plot- to the regional-scale. At the plot-scale, understanding how changes in snowmelt rate, timing, and amount influence runoff production will help water managers anticipate how runoff may change in the future in response to localized changes in snowmelt. At the watershed-scale, this work aims to understand how air temperature, precipitation, and land cover change alter streamflow production in a snow-dominated headwaters catchment using a land cover evolution model and a hydrologic model. This approach gives an estimate of how future land cover and climatology may change streamflow from snow-dominated catchments that span the alpine-subalpine transition. Finally, at the regional-scale the relationship between snowmelt rate and climate-corrected streamflow production is elucidated using a long-term hydrometeorology data set. Although distinct, these three distinct investigations advance our understanding of the linkage between snowmelt and

water availability in a region dependent on snowmelt for agricultural, human, and ecologic uses.

## Chapter 2: The Influence of Snowmelt Rate and Timing on Runoff Generation<sup>1</sup>

### Abstract

The mountain snowpack, a critical water resource for one-sixth of the global population, is expected to decline, melt earlier, and melt more slowly as the climate warms. Previous work has shown that lower snowmelt rates are associated with decreases in runoff production. Conversely, others have shown that earlier snowmelt may increase runoff production because vegetation water use is lower in early versus late spring. The relative importance of these factors with regard to runoff production is inherently linked to site-specific conditions such as plant available water storage and vegetation phenology. In order to disentangle the effects of snowmelt rate and timing on runoff production, we conduct a hydrologic modeling experiment at sites in Colorado (CO) and California (CA) designed to eliminate the observed multicollinearity between snowmelt rate and timing. We tested the sensitivity of snowmelt season runoff production (R) and changes in subsurface storage ( $\Delta S$ ) to snowmelt rate and timing using multiple linear regressions. Model results confirm that R is governed by the competing influence of snowmelt rate and timing. At CO, R and  $\Delta S$  were most sensitive to snowmelt timing versus snowmelt rate ( $\beta = -0.31$  vs.  $0.22$  and  $\beta = -0.24$  vs.  $0.18$ , respectively). At CA, R was most sensitive to snowmelt rate versus snowmelt timing ( $\beta = 0.67$  vs.  $-0.31$ ) and  $\Delta S$  was most sensitive to snowmelt timing versus snowmelt rate ( $\beta = -0.474$  vs.  $0.466$ ). Results suggest that future changes in R

---

<sup>1</sup> Manuscript for publication with coauthors C.L. Tague and N.P. Molotch

will be disproportionate to decreases in snowpack volumes due to the influences of snowmelt rate and timing.

## 2.1 Introduction

Mountainous regions are responsible for approximately 32% of the global freshwater discharge [Meybeck *et al.*, 2001] and within that, snow-dominated regions provide water for one-sixth of the global population [Barnett *et al.*, 2005]. Snowpack changes associated with climate warming have been valued in the trillions of dollars globally [Sturm *et al.*, 2017], indicating the importance of understanding how changes in snowpack will cascade into changes in runoff production. In the western United States alone, approximately 70% of runoff is derived from snowmelt [Sturm *et al.*, 2017]. Given the social, ecological, and economic value of mountain-derived water it is imperative to understand how changes in snowmelt will manifest as changes in runoff.

Changes in the timing and magnitude of snowmelt have been inferred using streamflow timing as a proxy for snowmelt [Stewart *et al.*, 2004; Stewart, 2009]. A decrease in snowfall fraction across the western United States has also been documented and attributed to increases in minimum storm temperature [Knowles *et al.*, 2006]. Shifts in observed peak snow water equivalent (SWE) and timing of snowmelt have also been observed across the western United States [Clow, 2010; Harpold *et al.*, 2012]. There is wide agreement across observational and modeling studies showing decreases in peak SWE and earlier snowmelt over the past three to four decades [Mote *et al.*, 2005; Clow, 2010; Harpold *et al.*, 2012]. First principles suggest that runoff volumes will scale with precipitation and snowpack magnitude. Questions remain, however, as to how changes in snowmelt

magnitude, rate, and timing are translated into changes in runoff volumes. Earlier snowmelt timing or faster rates, for example, may also change the partitioning of snowmelt between runoff and evapotranspiration.

Analysis of SWE observations across the western United States have revealed interrelationships between peak SWE, snowmelt timing, and snowmelt rate [Trujillo and Molotch, 2014]. For a given region or site, a large snowpack will tend to melt later and more quickly while a small snowpack will tend to melt earlier and more slowly [Trujillo and Molotch, 2014]. Recent modeling work in the Western United States confirms that snowmelt rates will decline in the future as snowmelt shifts earlier [Musselman et al., 2017]. Furthermore, previous work suggests the importance of snowmelt rate to runoff production and provides a possible subsurface mechanism through which this linkage occurs [Barnhart et al., 2016].

The multicollinearity between snowmelt rate, timing, and amount make it difficult to separate out the relative sensitivities of runoff production to these factors [Trujillo and Molotch, 2014]. Shallow snowpacks tend to melt earlier in the year and therefore melt more slowly because solar irradiance is lower earlier in the year. Barnhart et al. [2016] illustrated that this reduction in snowmelt rate reduces runoff production because slower melt results in less sub-surface runoff production. Complicating this behavior is the fact that energy availability for driving evapotranspiration is also reduced earlier in the year. Hence, on the one hand, earlier and slower snowmelt acts to reduce streamflow while at the same time earlier snowmelt and reduced available energy acts to reduce evapotranspiration (ET). We can then think of snowmelt driven runoff production as the residual of two competing rates, the input of water into the system, i.e. the snowmelt rate,

and atmospheric demand, i.e. ET. When snowmelt rates are relatively high, the rate of input (i.e. snowmelt) is increasingly greater than the rate of output (i.e. ET), resulting in greater soil moisture and greater sub-surface drainage. Snowmelt timing is critical to this behavior because evapotranspiration rates increase into the late spring [Moore *et al.*, 2008]. Additionally, snowmelt amount is also important because streamflow generation will not occur until the soil water deficit is overcome [Chauvin *et al.*, 2011].

Previous work has shown the importance of subsurface pathways in generating runoff from snow-dominated locations across the western United States. Results from end member mixing analyses from the Sierra Nevada and the Southern Rocky Mountains indicates the importance of subsurface water in streamflow [Liu *et al.*, 2004; 2008; 2012]. Observational and numerical modeling work from the Sierra Nevada also indicate that snowmelt is effective at entering the subsurface as snowmelt rates rarely exceed bedrock permeability, suggesting that subsurface and groundwater flow pathways are critical for snowmelt driven runoff production [Flint *et al.*, 2008]. Indeed, detailed observations from an instrumented hill slope in northern New Mexico show that lateral subsurface flow dominated runoff production from snowmelt events [Wilcox *et al.*, 1997]. Changes in snowmelt rate have been linked to changes in streamflow production via the subsurface [Barnhart *et al.*, 2016] necessitating further work understanding how changes in snowmelt rate and timing will influence not only runoff production, but also subsurface water stores for late season streamflow and vegetation water use.

In this work we use a hydrologic model to infer how changes in snowmelt rate and timing influence the storage and unsaturated and saturated flow of water within the soil column with the final goal of assessing the influence of these factors on runoff generation at

the plot scale and ultimately streamflow. The interrelation of snowmelt timing, rate, and amount as well as the competing snowmelt and evaporative fluxes on the moisture state of the soil column make it difficult to identify how sensitive runoff production is to changes in the snowpack. To address this knowledge gap we use observations and a hydrologic modeling experiment to investigate the sensitivity of runoff generation to changes in snowmelt rate and timing. We describe the sites selected in Section 2.2, the observational analysis and hydrologic model experiment design in Section 2.3, present observed patterns of snowmelt and runoff generation and model experiment results in Section 2.4, and discuss our findings in Section 2.5.

## **2.2 Study Areas**

Two sites within the United States National Science Foundation funded Critical Zone Observatory Network were selected for this work to capture a range of climatic conditions within the western United States. The Niwot Ridge US-NR1 AmeriFlux site is located in the Southern Rocky Mountain ecoregion [*Commission for Environmental Cooperation, 2006*] and is situated in a subalpine forest at 3,050 m asl on the eastern side of the Colorado Front Range to the west of Boulder, Colorado (Figure 2.1a). The Providence Creek site is located within the Sierra Nevada ecoregion at 1,950 m a.s.l. on the western slope of the Sierra Nevada mountain range (Figure 2.1b) in California. These two sites will be referred to as CO and CA, respectively.

Collocated at each site is an eddy covariance tower, to measure evapotranspiration (ET), a snow pillow, to measure SWE, and a meteorological station, to measure air temperature and precipitation (P, Figure 2.1). These data were used both for observational

analysis of snowmelt controls on hydrologic partitioning of precipitation between ET and runoff, hydrologic model calibration, and snowmelt scenario design.

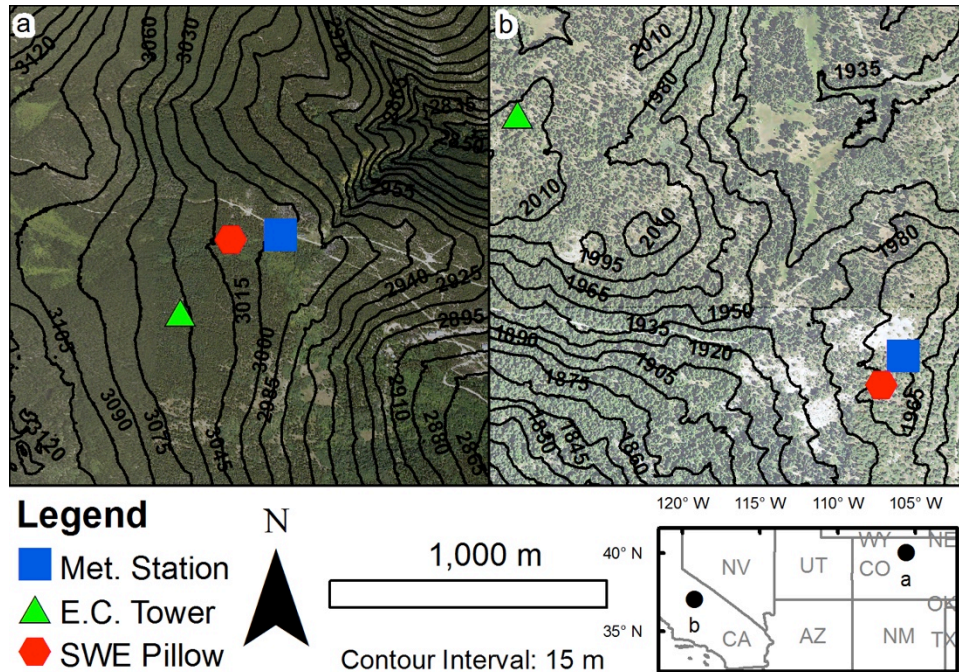


Figure 2.1: Aerial photography, topography, and instrumentation for the CO (a) and CA (b) sites with their locations within the United States indicated by the inset map. Snowmelt experiment simulations were built for the eddy covariance (E.C.) tower locations at each site.

The two sites span a range of precipitation (Figure 2.2) and snowpack climatologies. At CO, the precipitation seasonality is largely flat with slightly larger peaks during the winter months and during the summer monsoon (Figure 2.2a). Mean annual temperature at CO was 3.5 °C from 2010 to 2012 [Cowie *et al.*, 2017]. The precipitation pattern at CA is indicative of a Mediterranean climate, with most of the precipitation falling in the fall and winter and a distinctive summer dry period (Figure 2.2b) [Goulden and Bales, 2014]. The mean annual temperature at CA was 8.6 °C from 2004 to 2007 [Hunsaker *et al.*, 2012].

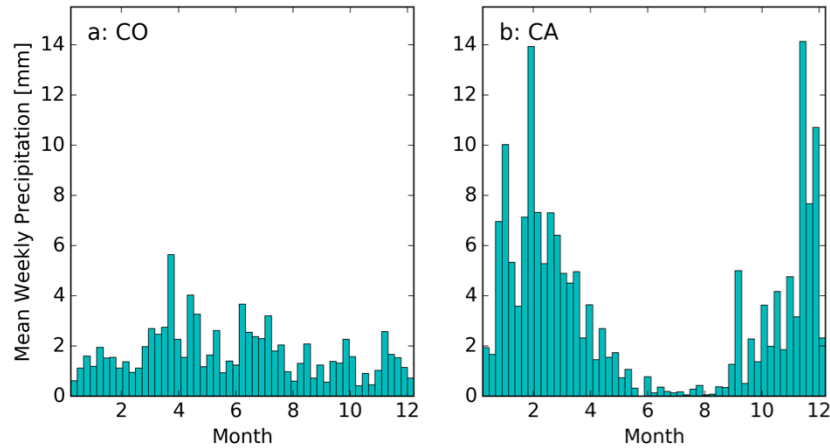


Figure 2.2: Weekly mean precipitation at CO (a) and CA (b). Precipitation was averaged over the period of 1952 – 2012 for CO and 2007 – 2014 for CA.

In addition to the inter-site differences due to precipitation timing and snowpack accumulation, both sites have different geologic settings and legacies, which shape the parent material and soil characteristics of each site. The CO site is underlain by granitic and siliceous metamorphic rock [Bilodeau *et al.*, 1987] with a glacial moraine covering the bedrock [Gable and Madole, 1976]. At CA, the soils are derived from crystalline intrusive rocks with compositions ranging from granite to diorite [Bales *et al.*, 2011]. Both sites have vegetation dominated by mixed conifer forests [Huxman *et al.*, 2003; Bales *et al.*, 2011] with key differences in soil parent material and snowpack climatology. This allows for a unique comparison of runoff generation across two locations representative of forested sites that develop a seasonal snowpack.

## 2.3 Methods

We conducted two sets of analyses to address how changes in snowmelt rate, timing, and amount influence runoff production: (1) analysis of snowmelt, precipitation, and evapotranspiration observations and (2) a hydrologic modeling experiment using the

Regional Hydro-Ecologic Simulation System (RHESys) [Tague and Band, 2004]. From the observational data we extracted a metric of runoff production, water year discharge normalized by water year precipitation ( $Q/P$ ), as well as the snowmelt rate, timing, and amount for each water year that records were available for each site. We then computed how sensitive  $Q/P$  was to snowmelt rate, timing, and amount using water years with high and low peak SWE in the period of record for each site. Snowmelt rate, timing and amount were distilled from observed niveographs (Figure 2.3a) via translation into a triangle that defines key points in the snow accumulation and melt period [Trujillo and Molotch, 2014](Figure 2.3b). In Figure 2.3b, snowpack accumulation begins at A and builds to peak SWE at B where the position of B along the y-axis denotes the magnitude of peak SWE and the position of B along the x-axis denotes the timing of peak SWE as well as the timing of snowmelt onset. The absolute value of the slope between B and C in Figure 2.3b is the mean snowmelt rate for a water year or site where C is the last day of snowmelt at the site. The range of the observed annual snowpack features can be shown by drawing a polygon around the ABC triangle where the upper edge of the polygon denotes the largest peak SWE amount and latest snowmelt timing while the lower edge of the polygon denotes the smallest peak SWE amount and earliest snowmelt timing recorded at the site (Figure 2.3b).

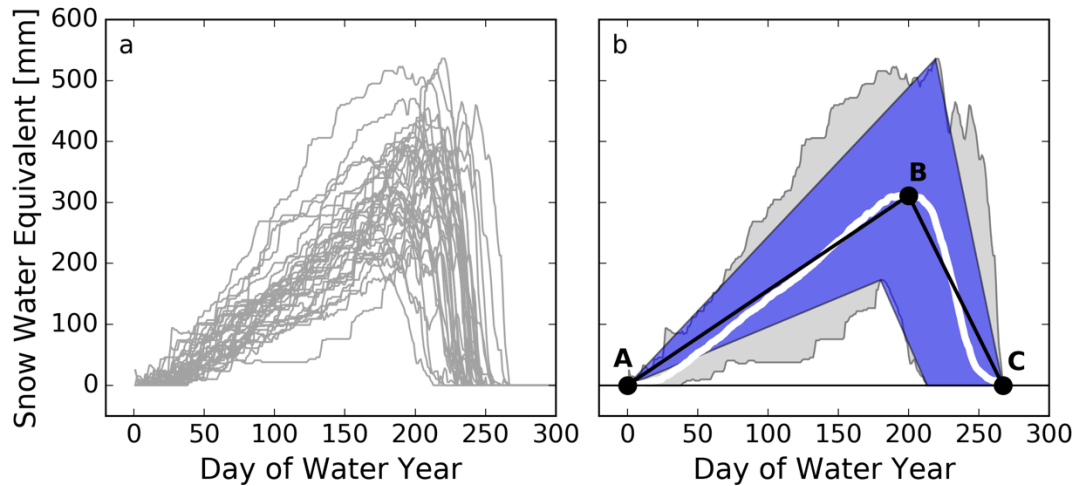


Figure 2.3: (a) Niveograph traces from the CO snow pillow from water years 1982 – 2014 and (b) simplified niveograph distilled from (a) showing the variability in the snowpack averaged over one water year (grey shaded region), the mean niveograph (white trace), and the decomposition of the niveograph into its components following Trujillo and Molotch [2014]. A denotes the beginning of the accumulation season, the position of B along the y-axis denotes the magnitude of peak SWE, the position of B along the x-axis denotes the timing of peak SWE and the timing of snowmelt, and C denotes when the snowpack has fully melted out. The absolute value of the slope between B and C denotes the mean snowmelt rate for the site or water year. Data used for this figure are available at <https://wcc.sc.egov.usda.gov/nwcc/site?sitenum=663>.

As each site has only limited availability of overlapping observational information, we extend the available observations by applying snowmelt-modeling scenarios generated from continuous uniform probability distributions of snowmelt rate, timing, and amount. The use of uniform distributions allows the generation of snowmelt scenarios that cover a wide snowmelt rate, timing, and amount parameter space where any combination of these parameters are equally likely. This allows us to separate the multicollinearity between snowmelt rate, timing, and amount in our experimental design. For the hydrologic modeling experiment, we pass each snowmelt scenario for each site to the corresponding hydrologic model for each site and extract a metric of snowmelt season runoff production (R) and use multiple linear regressions to assess the response of R to changes in snowmelt

rate and timing. Additionally, we investigate the snowmelt season change in storage ( $\Delta S$ ) for each scenario and use multiple linear regression to assess the sensitivity of  $\Delta S$  to changes in snowmelt rate and timing. We repeat these experiments for a range of plant available water storage capacities.

### 2.3.1 Observational Analysis

For each water year (October 1 – September 30), the SWE, ET, and P records (Table 2.1) were analyzed to extract the average snowmelt rate, peak SWE, and timing of peak SWE as well as the one-dimensional runoff ratio for each site. Snowmelt rate was calculated as the mean of the snowmelt season melt events, between the date of peak SWE and the date of melt out. Peak SWE was calculated as the peak in recorded SWE for each water year (vertical position of B in Figure 2.3b) and the timing of peak SWE (horizontal position of B in Figure 2.3b) was the date for which peak SWE occurred. The runoff ratio was computed for each water year at both sites assuming the simple water balance

$$Q = P - ET + \Delta S \quad (2.1)$$

We assume that  $\Delta S$  is zero in Equation 2.1 to allow a runoff ratio to be computed from a eddy covariance tower location on an annual basis. This assumes that there is no carryover storage at the site because carryover storage is often small relative to other annual fluxes [Sivapalan *et al.*, 2011]. The runoff ratio was derived from (2.1) by dividing both sides of the expression by P.

$$\frac{Q}{P} = 1 - \frac{ET}{P} \quad (2.2)$$

This allows a metric of hydrologic partitioning and runoff generation to be computed at the plot scale for sites where there are measurements of ET, but not discharge; however,

because we neglect  $\Delta S$ ,  $Q/P$  will be overestimated and should be treated as long-term potential runoff. We computed the sensitivity of  $Q/P$  for each site to a unit change in snowmelt rate, snowmelt timing, and snowmelt amount using the low and high snow years from the observed record at each site.  $Q/P$ , snowmelt rate ( $sm_r$ ), snowmelt timing ( $sm_t$ ), and snowmelt amount ( $sm_a$ ) were first standardized to allow their comparison using

$$sm_{r,s} = \frac{sm_r - \overline{sm_r}}{sm_{r,sd}} \quad (2.3)$$

$$sm_{a,s} = \frac{sm_a - \overline{sm_a}}{sm_{a,sd}} \quad (2.4)$$

$$sm_{t,s} = \frac{sm_t - \overline{sm_t}}{sm_{t,sd}} \quad (2.5)$$

where  $_s$  denotes the standardized variable,  $\overline{\quad}$  denotes the mean of the original variable, and  $sd$  denotes the standard deviation of the variable. The sensitivity of  $Q/P$  to unit changes in  $sm_r$ ,  $sm_t$ , and  $sm_a$  was then computed as

$$\frac{\Delta \frac{Q}{P}}{\Delta sm_{r,s}} = \frac{\frac{Q}{P}_{high} - \frac{Q}{P}_{low}}{sm_{r,s,high} - sm_{r,s,low}} \quad (2.6)$$

$$\frac{\Delta \frac{Q}{P}}{\Delta sm_{t,s}} = \frac{\frac{Q}{P}_{high} - \frac{Q}{P}_{low}}{sm_{t,s,high} - sm_{t,s,low}} \quad (2.7)$$

$$\frac{\Delta \frac{Q}{P}}{\Delta sm_{a,s}} = \frac{\frac{Q}{P}_{high} - \frac{Q}{P}_{low}}{sm_{a,s,high} - sm_{a,s,low}} \quad (2.8)$$

where  $_{high}$  and  $_{low}$  refer to water years with high and low snowpacks.

Table 2.1: Observations and Instrumentation.

<u>Site</u>	<u>Measurement</u>	<u>Measurement Height (m)</u>	<u>Instrument</u>	<u>Source</u>
CO	Precipitation (P)	1.5	Geonor T-200B wind-shielded, heated, weighing rain gauge	<a href="https://www.ncdc.noaa.gov/crn/">https://www.ncdc.noaa.gov/crn/</a>
CO	Air Temperature	1.5	Thermometrics Corporation PT1000 Platinum Resistance Thermometer	<a href="https://www.ncdc.noaa.gov/crn/">https://www.ncdc.noaa.gov/crn/</a>
CO	Evapotranspiration (ET)	21.5	Li-Cor 6262 Gas Analyzer, Campbell Scientific CSAT3 sonic anemometer	<a href="http://ameriflux.lbl.gov/sites/siteinfo/">http://ameriflux.lbl.gov/sites/siteinfo/</a> US-NR1
CO	Snow Water Equivalent (SWE)	0	Sensotec 100 inch pressure transducer	<a href="https://wcc.sc.egov.usda.gov/nwcc/site?sitenum=663">https://wcc.sc.egov.usda.gov/nwcc/site?sitenum=663</a>
CA	Precipitation (P)	3	Belfort 30 inch Alter-shielded precipitation gauge with Tedeo-Huntleigh Model 1042 load cell	<a href="http://criticalzone.org/sierra/data/dataset/2406/">http://criticalzone.org/sierra/data/dataset/2406/</a>
CA	Air Temperature	4	Vaisala HMP45C	<a href="http://criticalzone.org/sierra/data/dataset/2406/">http://criticalzone.org/sierra/data/dataset/2406/</a>
CA	Evapotranspiration (ET)	5-10 above canopy top	Li-Cor LI7000 Gas Analyzer	<a href="http://criticalzone.org/sierra/data/dataset/3654/">http://criticalzone.org/sierra/data/dataset/3654/</a>
CA	Snow Water Equivalent (SWE)	0	120 inch Sensotec pressure transducer	<a href="http://criticalzone.org/sierra/data/dataset/2406/">http://criticalzone.org/sierra/data/dataset/2406/</a>

### 2.3.2 Hydrologic Model Setup and Calibration

Hydrologic model simulations were carried out using one-dimension RHESSys models [Tague and Band, 2004] constructed for each of the two sites. We apply RHESSys in two distinct ways to accomplish the hydrologic modeling experiment. First we implement the full RHESSys model at each site in one dimension (e.g computing vertical hydrologic fluxes for a single model element) in order to calibrate drainage and storage parameters and to assess model performance. Second we replace the internally generated RHESSys snowmelt input time series with manufactured time series to explore the impact of different snow melt scenarios on runoff production. We describe these below.

RHESSys simulates hydrologic processes at an hourly to daily time step including snow accumulation and melt (although here we replace these with manufactured time series), soil water dynamics, interception of precipitation, evaporation, and transpiration. RHESSys models water storage and fluxes between vegetation canopy layers, litter, rooting zone storage, and unsaturated store, and a shallow subsurface saturated zone. In some cases, RHESSys also includes a deeper ground water store that accounts for bypass flow within permeable bedrock modeled as a linear reservoir. Additionally, RHESSys simulates biogeochemical cycling and accounts for meteorological and nutrient limitations on plant carbon and water cycling [Tague and Band, 2004]. Because RHESSys separately accounts for surface, plant accessible water and other subsurface water stores, as well as interactions between radiation, atmospheric and plant physiological controls on ET at a daily time step, it provides a useful, but relatively simple, approach for designing a multi-

factorial experiment to compare the impact of variations in the timing, intensity, and duration of water delivery during the snowmelt period.

RHESSys has been used to simulate the hydrology of watersheds in the Oregon Cascades [Tague and Grant, 2009; Tague et al., 2013], the California Sierra Nevada mountains [Tague et al., 2007; Jefferson et al., 2008; Tague and Peng, 2013; Son, 2015; Bart et al., 2016], and in the Jemez Mountains of New Mexico [Grant et al., 2013], including analysis of streamflow, evapotranspiration, and forest productivity sensitivity to climate change [Christensen et al., 2008; Tague et al., 2009; Grant et al., 2013; Tague and Peng, 2013]. RHESSys has also been used successfully in the Colorado Rockies where blowing snow and steep elevation and temperature gradients complicate modeling efforts [Hartman et al., 1999].

For each site, one-dimensional RHESSys simulations were constructed using published elevation data sets [Anderson et al., 2012; Guo and Bales, 2012]. Leaf area index (LAI) in the model was parameterized based on published LAI values for each site [Huxman et al., 2003; Bart et al., 2016]. Soil textural properties were extracted from the Web Soil Survey [Soil Survey Staff, 2016] and converted to the range of model parameters for saturated hydrologic conductivity, pore size index, and air entry pressure based on Dingman [2002]. These ranges informed the physically realistic parameter space use for calibration of each site.

Although for model experiments, we will replace RHESSys snowmelt estimates with our scenario values, for calibration of water storage parameters, we need estimates of actual snowmelt to drive the model. Prior to hydrologic model parameter calibration, the snowpack parameters for each site were calibrated against observed SWE using Monte

Carlo sampling. Model parameters calibrated in this step were minimum rainfall temperature, maximum snowfall temperature, air temperature melt coefficient, and maximum snowpack energy deficit. The later two parameters dictate the sensitivity of snowmelt to air temperature and the maximum energy deficit (i.e. cold content) of the snowpack in RHESSys. Nash-Sutcliffe efficiency (NSE) was used as the objective function for this calibration phase [Nash and Sutcliffe, 1970].

RHESSys model parameters for soil water bypass to groundwater, groundwater release, soil air entry pressure, soil pore size index, rooting depth, saturated hydraulic conductivity, and the decay of saturated hydraulic conductivity with soil depth were optimized using the shuffled complex evolution algorithm [Duan *et al.*, 1994] with the goal of matching monthly observed and modeled ET at each site. NSE was used as the objective function for the model optimization.

### **2.3.3 Hydrologic Model Experiment Snowmelt Scenario Design**

For each site, we construct 10,000 snowmelt scenarios based on snow pillow observations of snowmelt rate, timing, and amount. These scenarios are then run across a 15-member ensemble of PAWS parameterizations for each site. For this work, RHESSys was altered to accept a snowmelt input bypassing its internal snowmelt model for the purposes of this model experiment. This experimental design removes the multicollinearity between snowmelt rate, timing, and amount to explore the influence of snowmelt rate and timing on runoff generation. Through the ensemble of subsurface parameterizations we also explore how sensitive our analysis is to uncertainty in the subsurface parameterization (PAWS values) and actual spatial heterogeneity in these parameters.

To generate the snowmelt scenarios, we first built uniform probability distributions of  $sm_r$ ,  $sm_t$ , and  $sm_a$  based on the mean values and twice the standard deviation of these quantities from snow pillow observations at each site (Figure 2.4a,b). Scenarios were then generated for each site by drawing 10,000 sets of snowmelt rate ( $sm_r$ ), timing ( $sm_t$ ), and amount ( $sm_a$ ) values from the uniform probability distributions for each of these three variables constructed for each site (Figure 2.4c,d). These values were then used to generate a time series of snowmelt values for each scenario that were passed to the RHESys simulations for each site. Daily snowmelt rates generated for each site based on a linear relationship between day of water year and snow pillow observed snowmelt events at each site allowing the daily snowmelt to increase through the melt season (Figure 2.5). These values were then scaled so that the melt season average snowmelt rate for each scenario matched the value drawn from the uniform probability distribution of snowmelt rate (e.g. the absolute value of the ablation season slope between B and C in Figure 2.3b). This technique, while more complicated, allowed daily snowmelt rates to increase through the ablation season, as they tend to do in natural systems, while also maintaining a mean-scenario snowmelt rate that is consistent with the prescribed rate for the scenario. Additionally, during simulated snowmelt, precipitation was set to zero to reduce experiment complexity. While precipitation during the snowmelt season does occur with significant frequency, the objectives of the work presented here is to explore snowmelt dynamics explicitly and hence this simplification is necessary. The snowmelt scenarios were all prescribed over the same meteorological forcing data (i.e. minimum, average, and maximum air temperature, and precipitation) for the RHESys model over one water year

with the modification of precipitation during the snowmelt season to reflect daily snowmelt inputs samples described above.

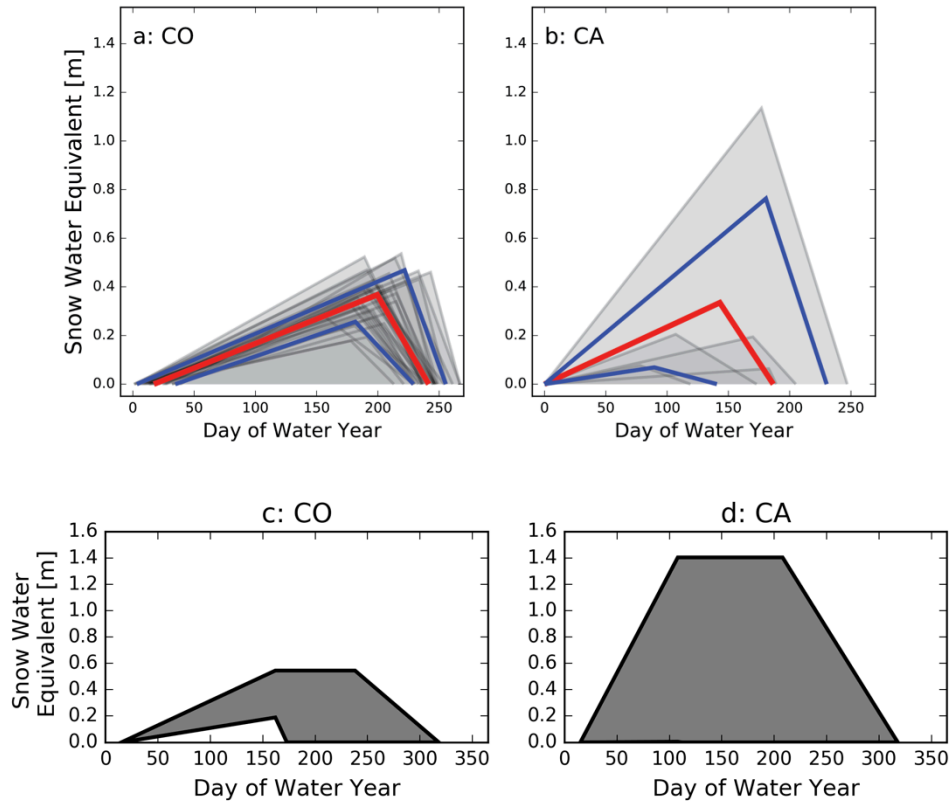


Figure 2.4: Snowpack triangles (gray) for (a) CO and (b) CA showing the mean (red) and the 10% and 90% percentiles (blue) for each site and snowmelt experiment polygons representing the ranges of snowmelt rate, timing, and amount covered by the snowmelt scenarios for (c) CO and (d) CA. The shaded region in each panel shows the range of combinations of snowmelt rate, timing, and amount used for each site based on snow pillow observations. Data used for (a) were from water years 1982-2014 and data used for (b) were from water years 2011-2015.

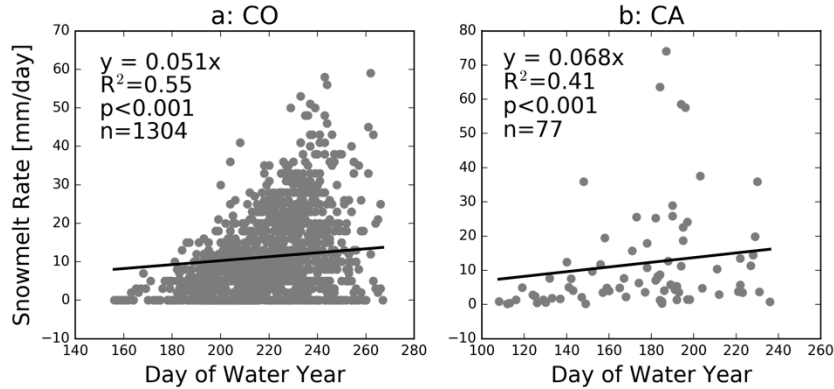


Figure 2.5: Linear relationships between the timing of daily snowmelt events and the rate of daily snowmelt events at CO (a) and CA (b). These relationships were used to parameterize the seasonal increase in snowmelt rate through each snowmelt scenario at each site. The time periods of the data used in (a) and (b) are the same as in Figure 2.4.

As the soil parameterization within the hydrologic modeling framework we use may influence runoff sensitivity analyses [Tague and Peng, 2013], we explore the effects of uncertainty in plant available water storage (PAWS) on the model experiment results as this may influence how snowmelt is partitioned between runoff and evaporative fluxes [Brooks et al., 2015]. To examine the sensitivity of the runoff-snowmelt relationship to the sub-surface water storage parameterization of RHESSys, we conduct our model experiment using an ensemble of sub-surface parameterizations. The ensemble of 15 PAWS parameterizations was generated by multiplying the optimized rooting depth from each site by values ranging from 0.01 to 60 and PAWS was computed following Appendix A. Prior to running the snowmelt experiments for each site and subsurface parameterization, the hydrologic model was initialized using an average water year for each site repeated for ten years to allow the modeled hydrologic stores to stabilize under each of the different subsurface parameterizations.

### 2.3.4 Hydrologic Model Experiment Analysis

Similarly to Equation 2.2, each snowmelt scenario simulation output was analyzed to extract the snowmelt period runoff ratio as:

$$R = 1 - \frac{ET_{sm}}{sm_a} \quad (2.9)$$

Where  $R$  is snowmelt season the runoff ratio,  $ET_{sm}$  is the total modeled evapotranspiration during the snowmelt period (between B and C in Figure 2.3b), and  $sm_a$  is the snowmelt amount for the snowmelt experiment, which is equivalent to peak SWE.  $R$  was used as the dependent variable in multiple regression analysis to investigate how sensitive snowmelt season runoff production is to changes in snowmelt rate and snowmelt timing with the form

$$\hat{R} = \beta_0 + \beta_1 sm_r + \beta_2 sm_t \quad (2.10)$$

where  $\hat{R}$  are the predicted  $R$  values,  $\beta_0$  is the intercept of the model,  $\beta_1$  is the coefficient for  $sm_r$ , snowmelt rate, and  $\beta_2$  is the coefficient for  $sm_t$ , snowmelt timing. Snowmelt rate ( $sm_r$ ) and  $sm_t$  here are taken from the parameters used to construct each snowmelt experiment (Section 2.3.3). Snowmelt amount ( $sm_a$ ), i.e. peak SWE, was not used as an independent variable because it would fall on both sides of the multiple regression equation.

Additionally, because first principles suggest that  $R$  increases with increased SWE, we focused our analysis on snowmelt rate and timing. Multiple regression analysis was carried out using StatsModels [Perktold et al., 2016]. The dependent and independent variables in the multiple regression analysis were standardized to allow comparison of the model coefficients for snowmelt rate and snowmelt timing using Equation 2.3.

For the experiment analysis, we use a simple water balance to compute the snowmelt season change in subsurface storage ( $\Delta S$ ) and assume that this store will be used as either runoff, via drainage to the stream as subsurface flow later in the season or at longer time scales [Liu *et al.*, 2004], or evapotranspiration. We computed  $\Delta S$  as

$$\Delta S = SWE_{peak} - Q_{sm} - ET_{sm} \quad (2.11)$$

Where  $Q_{sm}$  is the total simulated snowmelt season discharge. Positive values of  $\Delta S$  indicate that snowmelt remains in the subsurface while negative values of  $\Delta S$  indicate that streamflow and evapotranspiration during the snowmelt season have decreased subsurface storage and that no additional snowmelt water remains in the subsurface. We evaluated the sensitivity of  $\Delta S$  to snowmelt rate and snowmelt timing using regression analysis in the following form

$$\hat{\Delta S} = \beta_0 + \beta_1 sm_r + \beta_2 sm_t \quad (2.12)$$

where  $\hat{\Delta S}$  are the predicted  $\Delta S$  values. The independent variables were standardized in the same way as in Equation 2.8. The multiple regression analysis of both R and  $\Delta S$  was carried out for all 15 soil water storage (PAWS) parameter sets for each site.

## 2.4 Results

### 2.4.1 Observed Relationships

CO and CA had mean  $\pm$  standard deviation Q/P values of  $0.16 \pm 0.16$  and  $0.54 \pm 0.16$ , respectively from water years 2004-2014 and 2011-2015. CA had a Q/P range between observed low and high snow years of 0.38, while CO had a range of 0.14 (Table 2.2). These ranges of Q/P values were converted to sensitivities of Q/P to unit changes in standardized

snowmelt rate, timing, and amount to allow inter-comparison of the sensitivities using Equations 2.6-8 (Table 2.3).

Table 2.2: Observed R/P for high and low snow years at CO and CA. Season average snowmelt rate as well as snowmelt amount and snowmelt timing are also given. DOWY is an abbreviation for day of water year.

Site	Water Year	Snowmelt Rate [mm/day]	Snowmelt Amount [mm]	Snowmelt Timing [DOWY]	Q/P
CO	2012	3.82	279	156	0.11
CO	2011	19.64	432	234	0.25
CA	2015	1.86	76	78	0.40
CA	2011	16.22	1135	177	0.78

Runoff production was most sensitive to a change in snowmelt amount at both sites (Table 2.3). At CO, runoff production was similarly sensitive to snowmelt rate and snowmelt timing with computed sensitivities of 0.04 for both (Table 2.3). At CA, runoff production was more sensitive to changes in snowmelt timing (0.07) than to snowmelt rate (0.06, Table 2.3). The signs of all the sensitivities computed were positive across both sites and all metrics of snowmelt. Given that the energy available for transpiration increases with late snowmelt, we would expect that the sensitivity of Q/P to snowmelt timing would be negative with later snowmelt leading to less runoff generation; however, this is not shown by these data due to the multicollinearity between snowmelt rate, timing, and amount present in this observational data set [Trujillo and Molotch, 2014].

Table 2.3: Change in Q/P to a unit change in snowmelt rate, timing, and amount for CO and CA. Snowmelt rate, timing, and amount values were standardized using Equation 2.3 to allow comparison of sensitivity values.

Site	$\Delta Q/P / \Delta \text{Snowmelt Rate}$	$\Delta Q/P / \Delta \text{Snowmelt Amount}$	$\Delta Q/P / \Delta \text{Snowmelt Timing}$
CO	0.04	0.06	0.04
CA	0.06	0.06	0.07

Additionally, the observational sensitivities presented in Table 2.3 fit with first principles in that Q/P is most sensitive to snowmelt amount at CO and CA. Generally, we would expect that Q/P would increase with increased precipitation (i.e. snowmelt amount) [Chauvin *et al.*, 2011; Luce *et al.*, 2013]. The lack of different Q/P sensitivities to snowmelt timing and snowmelt rate at CO indicates the difficulty in comparing different descriptors of snowmelt with runoff production from observations alone due to the multicollinearity between snowmelt rate, timing, and amount [Trujillo and Molotch, 2014]. Given the short data records available at both of these sites, statistical separation of the effects of snowmelt rate and timing on runoff production is difficult to assess. Furthermore, the period of record of the observations used, not just the number of observations, may influence these results. The hydrologic modeling experiment presented herein addresses these shortcomings by varying snowmelt rate, timing, and amount using uniform probability distributions to eliminate the multicollinearity between these factors.

### 2.4.2 Hydrologic Model Calibration

Calibration of soil and groundwater parameters at both sites yielded simulations that estimated the general seasonal patterns of observed ET on a monthly basis (Figure 2.6, Table 2.4). At CO, the model achieved a monthly ET NSE of 0.32, overestimating peak ET

and underestimating winter ET. At CA, simulated ET overestimated some peak ET events and overestimated winter ET with a monthly NSE of 0.29. There is likely to be differences between modeled and observed ET associated with spatial variation within the tower fetch as well as differences associated with uncertainty in meteorologic forcing data and snow parameters. Given this, we argue that model-observation correspondence is acceptable given the goal of using the model to show how manufactured snowmelt drivers influence runoff.

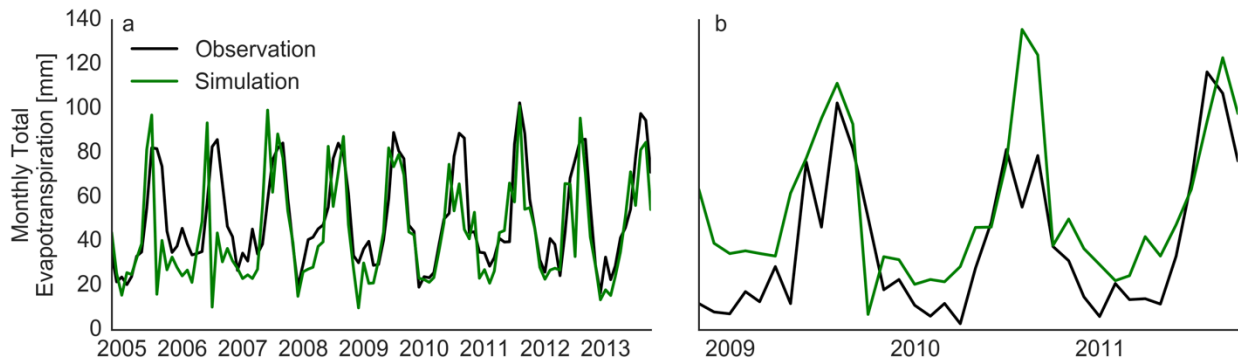


Figure 2.6: Evapotranspiration observations (black lines) and simulated fluxes (green lines) for CO (a) and CA (b). Vertical axes in (a) and (b) are the same.

Table 2.4: Calibration parameters and statistics for CO and CA. Abbreviations are as follows: decay of saturated hydrologic conductivity with depth (m), saturated hydrologic conductivity (ksat), pore size index (po), soil air entry pressure (pa), proportion of precipitation routed to groundwater store (gw1) and proportion of ground water store released as streamflow (gw2), and Nash-Sutcliffe efficiency (NSE).

Site:	CO	CA
m [1/m H2O]	13.39	0.04
ksat [m/day]	338.84	213.63
soil depth [m]	4.38	4.11
rooting depth [m]	0.38	1.11
po [1]	2.27	2.6
pa [m H2O]	0.05	0.85
gw1 [%]	0.21	0.12
gw2 [%]	0.6	0.37
minimum rain temperature [degC]	-1.657	3.07
maximum snow temperature [degC]	3.007	3.37
snowmelt temperature coefficient [m H2O/degC]	0.0967	0.0003
maximum snowpack energy deficit [degC/day]	-52.72	-160.2
NSE	0.32	0.29

### 2.4.3 Snowmelt Modeling Experiment

We first explore the snowmelt experiment output at each site by comparing and contrasting the ET time series at three different snowmelt rate bins: slow (lowest 10%, Figure 2.7a), medium (middle 10%, Figure 2.7b), and fast (highest 10%, Figure 2.7c) taken from the middle 10% of the snowmelt amount values present in the scenarios for each site, e.g. between the 45<sup>th</sup> and 55<sup>th</sup> snowmelt amount percentiles. To show how snowmelt rate interacts with snowmelt timing, we present time series depicting the difference between ET from the latest and earliest snowmelt scenarios within each snowmelt bin for each day since the start of snowmelt. There was a clear transition during the snowmelt season at CO in all three panels of Figure 2.7 where the site transitioned from having greater ET with late season snowmelt to slightly greater ET for early season snowmelt. This effect only

occurs at CO, which may indicate that continental snowpacks are more sensitive to changes in snowmelt timing. At CA, late season ET was always greater than early season ET (Figure 2.7a,b,c) suggesting that the timing of water delivery with respect to energy availability is critical for forest water use. At CO and CA, it was clear that later snowmelt results in greater hydrologic partitioning to the atmosphere (ET) under a range of snowmelt rate conditions (Table 2.5). The influence of snowmelt rate on ET was also more difficult to examine from these time series (Figure 2.7) and will be investigated below.

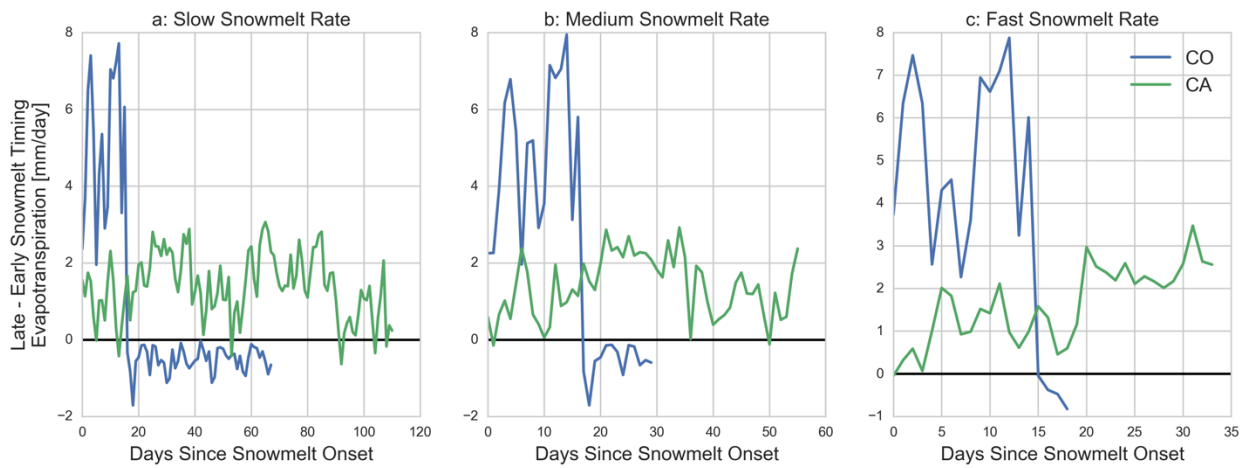


Figure 2.7: Example time series from the hydrologic modeling experiment showing the difference between early and late snowmelt timing evapotranspiration for scenarios with slow snowmelt (a), medium snowmelt (b), and fast snowmelt (c). Time series are drawn from scenarios controlled for snowmelt amount to illustrate the effects of changes in snowmelt timing and rate on hydrologic partitioning.

Table 2.5: Snowmelt season ET totals from the scenarios presented in Figure 2.7.

Snowmelt Timing	CO		CA	
	Early Snowmelt [mm]	Late Snowmelt [mm]	Early Snowmelt [mm]	Late Snowmelt [mm]
Slow	35	90	88	242
Medium	16	92	27	105
Fast	10	87	12	67

We interrogate how simulated R was influenced by changes in snowmelt rate and timing by mapping the R values to the snowmelt rate and timing values for each scenario and each site (Figure 2.8). Mapping R in this way allows gradients in the R surface with respect to both snowmelt rate and snowmelt timing to be identified. Snowmelt season runoff generation at CO and CA was greatest in the upper left and least in the lower right corners of the plot (Figure 2.8a,b). At CO, the downward curve of the R surface with lessening snowmelt rates and later snowmelt timing suggests that R is similarly sensitive to both factors with slower snowmelt and later snowmelt timing generating less R (Figure 2.8a). At CA, the R surface decreases most notably with slower snowmelt and only slightly with later snowmelt timing suggesting that R is most sensitive to snowmelt rate at this site (Figure 2.8b). We note that these are qualitative descriptors of the R behavior at each site and that the gradients presented in Figure 2.8 are partially dictated by the range of snowmelt rate and timing considered for each site.

The mean snowmelt rate and timing for each site (from water years 1981-2015 and 2008-2014 for CO and CA, respectively) are plotted as stars on the response surfaces in Figure 2.8 and allow projection of R at each site under future changes in snowmelt rate and timing. For example, we expect future snowmelt to be slower [Musselman *et al.*, 2017] and to occur earlier in the year [Harpold *et al.*, 2012], resulting in a translation of mean snowmelt timing and rate to the lower left in Figure 2.8; however, the relative changes in snowmelt rate and timing will dictate the exact direction and length of the translation and the response of a site. At CO and CA, this would generally result in a decrease in R.

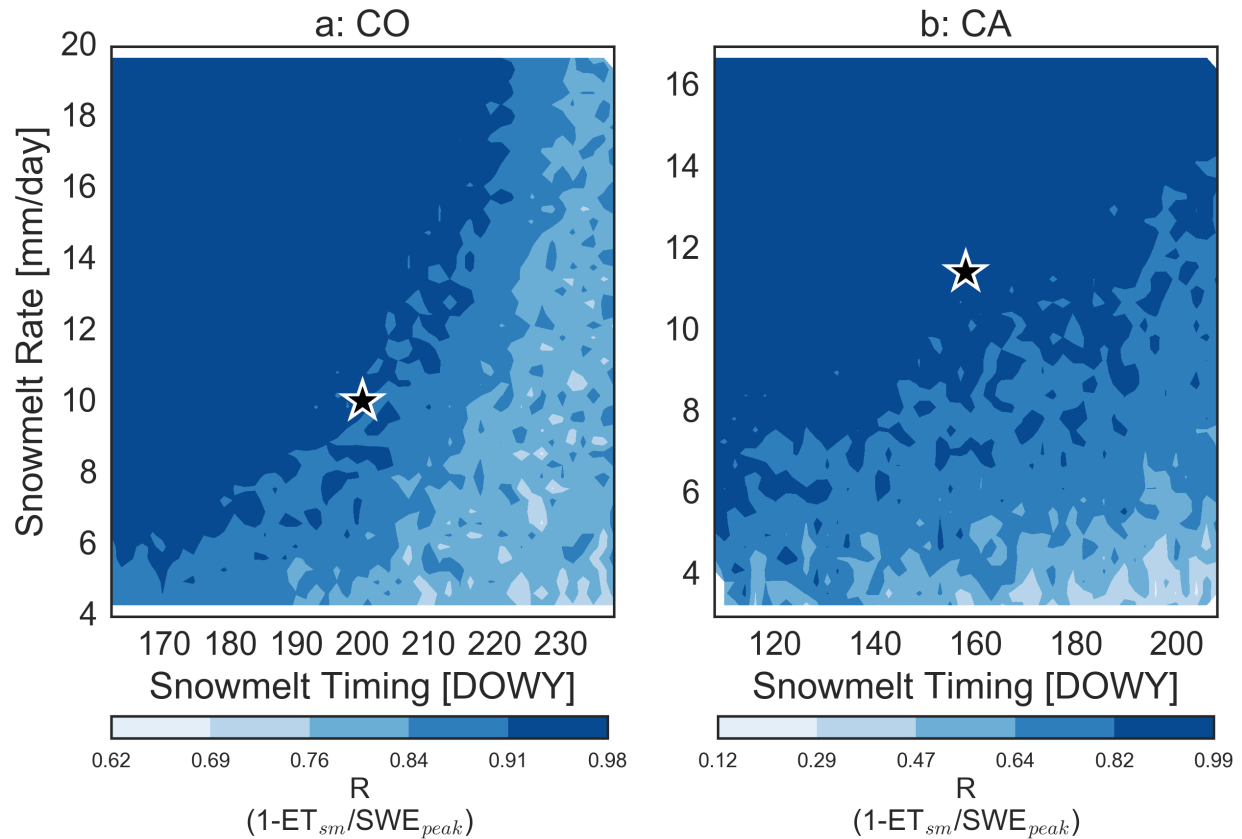


Figure 2.8: Simulated runoff production (R) mapped across the experimental ranges of snowmelt timing and snowmelt rate for CO (a) and CA (b). Observed average snowmelt rate and snowmelt timing for each site are indicated by the star in each plot.

Multiple regression coefficients from the best parameter set for each site from the snowmelt scenario experiment show that snowmelt rate was more important for CA snowmelt season runoff production while snowmelt timing was more important for runoff production at CO. CO had a snowmelt rate coefficient of 0.22, while CA had a coefficient of 0.67 (Figure 2.9). Both sites had a snowmelt timing coefficient of -0.31 (Figure 2.9). The multiple regression models for CO and CA had  $r^2$  values of 0.68 and 0.61, respectively ( $p < 0.001$ ). At CO and CA, the difference in the sign of the regression coefficients for snowmelt rate and snowmelt timing illustrates the competition between snowmelt timing

and snowmelt rate in snowmelt season runoff production with later snowmelt timing resulting in less runoff and more rapid snowmelt resulting in more runoff.

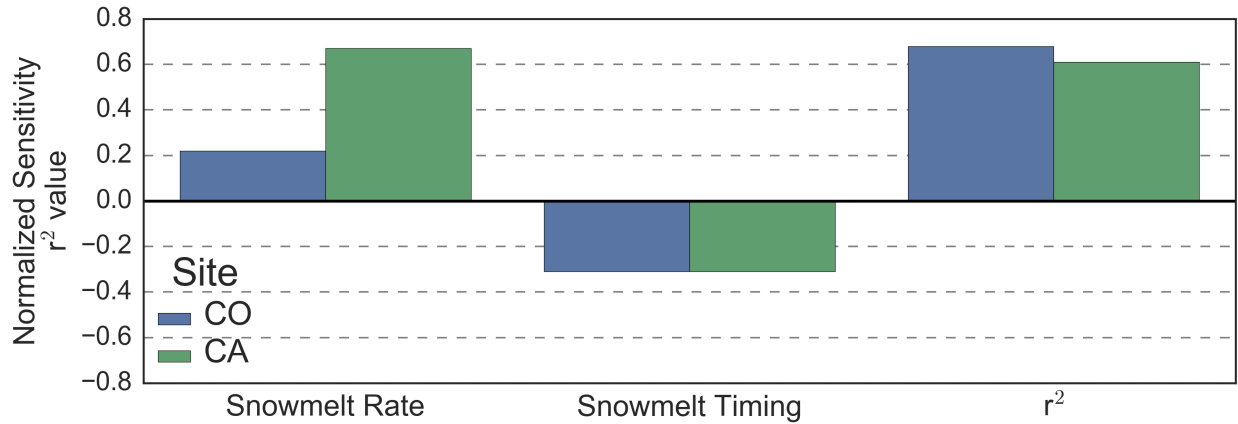


Figure 2.9: Comparison of snowmelt experiment multiple regression coefficients between CO and CA. All relationships were significant with  $p < 0.001$ .

Multiple regression results across the range of PAWS values for each site show the sensitivities of the snowmelt season runoff multiple regression coefficients to different soil storage conditions (Figure 2.10). At CO and CA the snowmelt rate coefficient increased with increasing PAWS while the snowmelt timing coefficient decreased with increasing PAWS (Figure 2.10). This shows that, as PAWS increases, the sensitivity of R to both snowmelt rate and snowmelt timing increases and underscores the importance of soil water storage capacity in mediating the partitioning of snowmelt between R and ET.

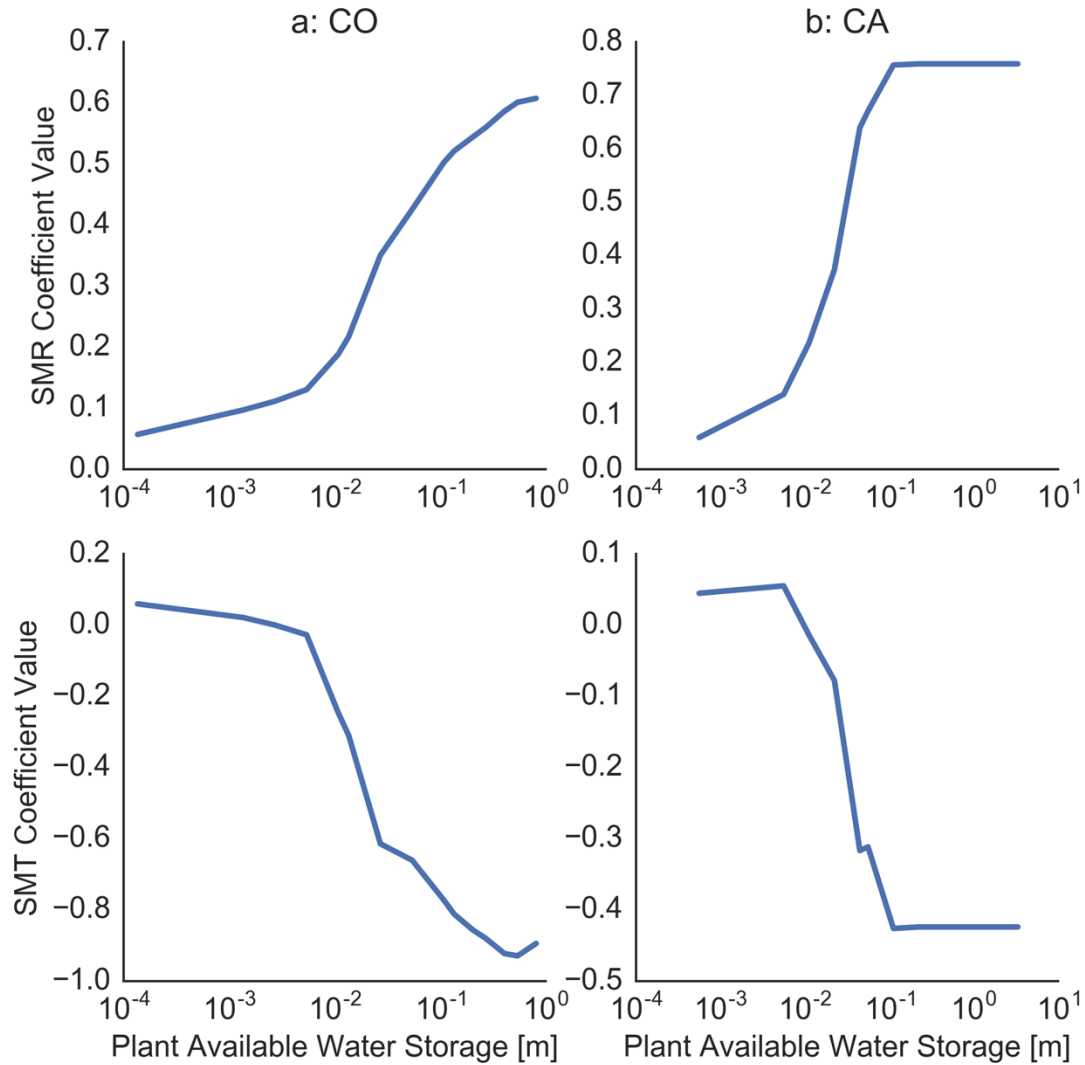


Figure 2.10: Snowmelt rate (top row) and snowmelt timing (bottom row) coefficients across a range of PAWS values for CO (a) and CA (b). All relationships are significant with  $p < 0.001$ .

#### 2.4.4 Changes in Snowmelt Season Subsurface Storage

To investigate changes in snowmelt season subsurface storage we analyzed snowmelt season water balance closure,  $\Delta S$ , during the snowmelt experiment simulations for each site. At CO and CA,  $\Delta S$  decreased with later and slower snowmelt similar to the R response (Figure 2.11). The decrease in  $\Delta S$  at CO appears to be uniform along the snowmelt

rate and snowmelt timing axes suggesting that the sensitivity of  $\Delta S$  to changes in snowmelt rate and timing was similar (Figure 2.11a). At CA, the  $\Delta S$  surface declines more noticeably with respect to snowmelt rate than with respect to snowmelt timing (Figure 2.11b). As with Figure 2.8, the stars shown in Figure 2.11 represent the mean snowmelt rate and timing for each site. As snowmelt rates become slower and snowmelt timing (i.e. the timing of the start of snowmelt) moves earlier in the year the location of each star will move down and to the left transitioning both sites to a regime with a smaller  $\Delta S$  and therefore less subsurface water to sustain late season streamflow and vegetation productivity.

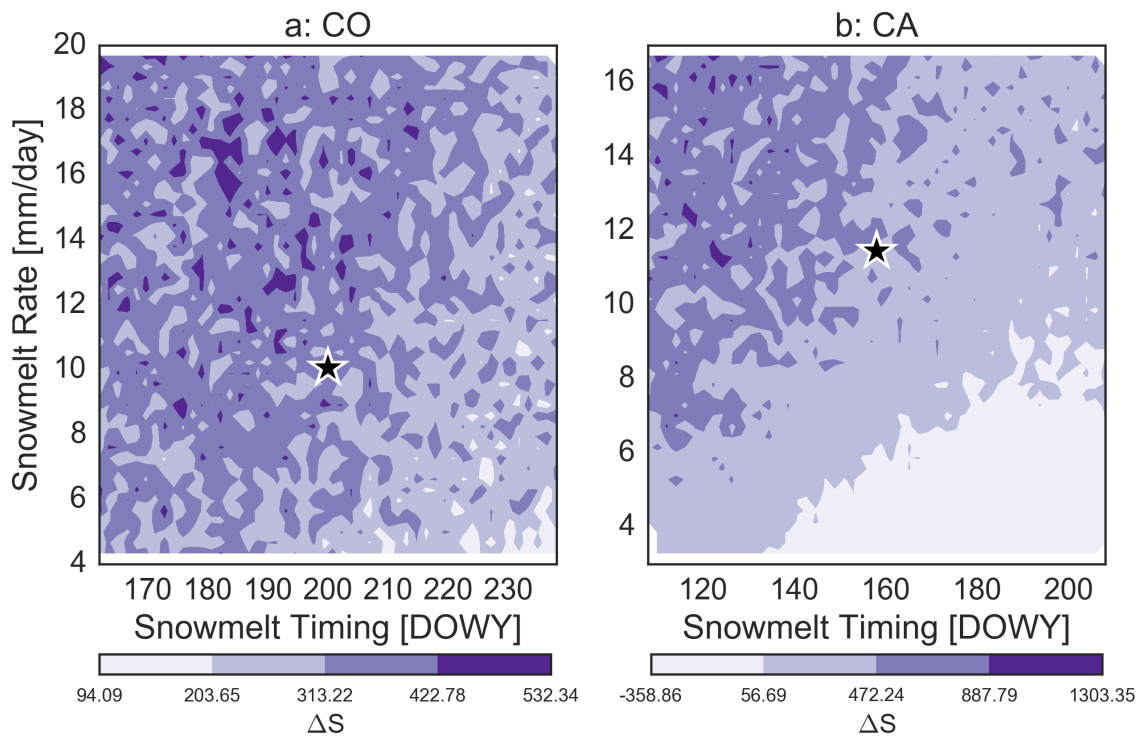


Figure 2.11: Simulated  $\Delta S$  mapped to different snowmelt rate and timing scenarios at (a) CO and (b) CA.

At CO, multiple regression analysis showed that  $\Delta S$  was most sensitive to changes in snowmelt timing with a negative snowmelt timing coefficient suggesting that as snowmelt occurs earlier in the year  $\Delta S$  will increase (Figure 2.12). At CA,  $\Delta S$  was most sensitive to a

change in snowmelt timing; however, the coefficient for snowmelt was similar in magnitude suggesting that changes in snowmelt rate and timing have similar effects, albeit with opposite signs, on snowmelt season subsurface storage (Figure 2.12). Similar to Figure 2.9, the coefficients for snowmelt rate and snowmelt timing in Figure 2.12 partially balance where losses in  $\Delta S$  due to slower snowmelt are partially offset by gains in  $\Delta S$  due to earlier snowmelt timing.

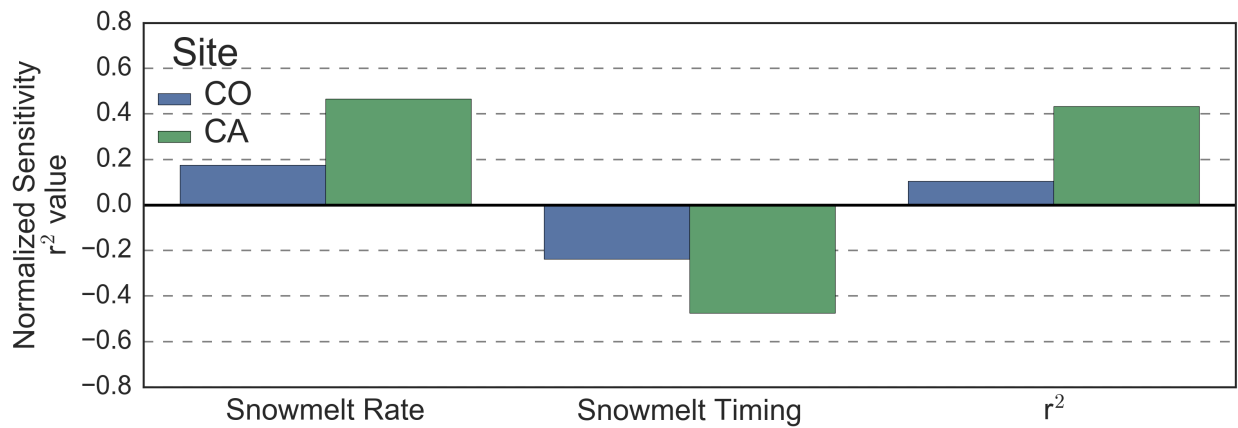


Figure 2.12: Snowmelt season  $\Delta S$  multiple regression coefficient values and  $r^2$ . All relationships are significant with  $p < 0.001$ .

## 2.5 Discussion

Air temperature warming simulations across the western United States suggest that peak SWE will be reduced in the future and that snowmelt will occur earlier and more slowly [Musselman *et al.*, 2017]. The interaction of these changes in snowmelt then suggests that runoff will not decrease proportionally to decreases in peak SWE but with additional decreases attributed slower snowmelt [Barnhart *et al.*, 2016]. Work presented herein suggests that, depending on site-specific conditions, runoff gained from earlier snowmelt timing may not be great enough to offset the runoff loss due to slower snowmelt

(Figure 2.9). Previous work has focused on identifying changes in snowmelt timing and amount [Clow, 2010; Harpold et al., 2012] and changes in streamflow amount and timing [Stewart et al., 2004; Rood et al., 2005]; however, we focus on distinguishing the respective effects of changes in snowmelt rate and snowmelt timing on runoff production. At both sites we show that when the multicollinearity between snowmelt rate and timing is experimentally removed, that runoff increases due to earlier snowmelt timing have the potential to be offset by runoff decrease due to slower snowmelt (Figure 2.9).

Trends towards earlier snowmelt timing have been clearly identified in the Rocky Mountains [Clow, 2010; Harpold et al., 2012] and in the Sierra Nevada [Stewart et al., 2005]. Furthermore, recent findings indicate that snowmelt rate will decrease in the future across the western United States [Musselman et al., 2017]. Our findings, when coupled to documented trends in earlier snowmelt and slower snowmelt, suggest that individual site or basin runoff production sensitivity to changes in snowmelt rate and timing will dictate the degree to which increased runoff production from earlier snowmelt may counteract decreased runoff production due to slower snowmelt. At CO, more runoff is generated due to earlier snowmelt than is lost to slower snowmelt (Figure 2.9). At CA, more runoff is lost due to slower snowmelt than is gained due to earlier snowmelt timing (Figure 2.9). Work from the Northern Rocky Mountains and the northwestern United States shows decreases in streamflow volumes across the historic measurement record [Rood et al., 2005] suggesting that the net effect of earlier snowmelt timing and slower snowmelt will be decreasing runoff production [Barnhart et al., 2016]; however, part of this decrease in streamflow may be due to increased ET from elevated vapor pressure deficits under warmer conditions.

Recent, regional-scale work from across the western United States has highlighted snowmelt rate as a driver of runoff production using a gridded hydrometeorology data set and a Budyko-style analysis [Barnhart et al., 2016]. The work presented herein is congruent with Barnhart et al. [2016] in that it reinforces the importance of snowmelt rate on runoff production. We cannot evaluate our snowmelt timing results against Barnhart et al. [2016]; however, because they did not test the influence of snowmelt timing on runoff production. Our findings indicate that changes in both snowmelt rate and timing influence snowmelt season subsurface storage changes ( $\Delta S$ ), which is important for late season streamflow and vegetation water use. The relationships we found for CO and CA between snowmelt rate and timing and  $\Delta S$  fit with the proposed mechanism within Barnhart et al. [2016] where rapid snowmelt saturates the root zone, driving runoff production via a pathway isolated from atmospheric demand. Our work also highlights that early snowmelt may also be able to drive increases in  $\Delta S$  when snowmelt occurs before high vegetation water use (Figure 2.12). Furthermore, the importance of snowmelt timing (Figure 2.9) further supports the findings of Jeton et al. [1996] where runoff production is dependent on the timing of water delivery and vegetation water use.

Additionally, the work presented herein fits well with work evaluating watershed-scale response to increased air temperature. In the Sierra Nevada, a hydrologic modeling study investigated the effect of a 3 °C increase in air temperature on watershed-scale hydrologic fluxes [Tague and Peng, 2013]. Similar to the work presented herein, the 3 °C increase in air temperature resulted in earlier and slower snowmelt and a slight decrease (-3%) in streamflow, although interannual variability caused streamflow to vary from -30% to 20% under the warming scenario [Tague and Peng, 2013]. This fits with our analysis in

that the competing influence of slower snowmelt rates, which decrease runoff, and earlier snowmelt, which increases runoff, may partially cancel resulting in a small net effect.

Pervious work reporting the sensitivity of ET to changes in subsurface storage in the Colorado Rockies, Oregon Cascades, and California Sierra Nevada [Garcia and Tague, 2015] shows that the sensitivity of annual ET to changes in subsurface storage decreases at 0.265 m and 0.195 m of PAWS for the Colorado Rockies and the California Sierra Nevada, respectively. Similar to Garcia and Tague [2015], we found the regression coefficients for Equation 9 at CO and to be sensitive to changes in PAWS (Figure 2.10) across a range of PAWS values. The influence of subsurface storage on the sensitivity of a site to changes in snowmelt rate and timing underscores the need to characterize the subsurface of runoff producing areas to better understand how runoff will change in the future. Examples of this have been carried out along geophysical transects within many of the United States, National Science Foundation, Critical Zone Observatories [Holbrook et al., 2014; St Clair et al., 2015]; however, further work and long-term hydrologic and meteorologic observations are needed to translate geophysical measurements into catchment-scale subsurface properties and perceptual models of critical zone hydrologic function.

It is also possible to compare the observational and simulated results from the work presented herein. Observations at CO showed similar Q/P sensitivity to both snowmelt rate and timing while the hydrologic modeling experiment indicates that R at CO is more sensitive to changes in snowmelt timing than to changes in snowmelt rate (Figure 2.9). At CA, observations showed that Q/P was more sensitive to snowmelt timing than snowmelt rate while simulation results indicated that R is more sensitive to snowmelt rate than timing (Figure 2.9). There is a sign mismatch in this comparison though, which is likely the

result of the multicollinearity within the snowmelt rate, amount, and timing data set used for the observational analysis [Trujillo and Molotch, 2014] or because the observational analysis only covers a small subset of potential snowmelt rate and timing conditions at each site. Furthermore, the observational analysis is conducted using annual values while the snowmelt simulation experiment only considers the snowmelt period. The differences between the observational and simulated results underscores the new knowledge gained by the exercise of removing the multicollinearity between snowmelt rate, timing, and amount and examining each component's influence on runoff generation. This work also highlights the need for long-term hydrologic measurements, as we were unable to statistically separate the influence of snowmelt rate and timing on runoff generation from observation data due to the period of record at the study sites.

## **2.6 Conclusion**

The impact of changing snowmelt rate, timing, and amount on snowmelt season runoff production is difficult to evaluate given the multicollinearity between these three components of snowmelt. We provide the first observation and modeling experiment aimed at disentangling the multicollinearity among snowmelt rate, timing, and amount. This work also investigated how sensitive changes in snowmelt season subsurface storage were to changes in snowmelt rate and timing. This type of work is essential as previous work has highlighted how snowmelt rate may change in the future and how this may impact regional streamflow production; however, there are also associated changes in snowmelt timing and amount, which may impact runoff generation.

Observations of runoff production and snowmelt suggest that runoff production was most sensitive to and increased with snowmelt amount at CO and CA (Table 2.3). Hydrologic modeling experiment results show that snowmelt season runoff production was most sensitive to snowmelt timing with later snowmelt leading to less runoff production at CO (Figure 2.9). At CA, runoff production was most sensitive to snowmelt rate with more rapid snowmelt leading to greater runoff production (Figure 2.9). We also showed the importance of snowmelt timing and snowmelt rate to the change in snowmelt season subsurface storage (Figure 2.12). In this regard, the change in snowmelt season subsurface storage at CO and CA was most sensitive to changes in snowmelt timing. Additionally, we found that the sensitivity of runoff production to changes in snowmelt rate and timing increased with greater plant available water storage at both sites.

This work shows that snowmelt season runoff losses due to slower snowmelt may be partially offset by runoff gains from earlier snowmelt. Given climate driven decreases in snowpack volumes, earlier snowmelt timing, and decreases in snowmelt rate, this work suggests that individual site runoff production behavior will depend on the relative sensitivity of runoff at the site to changes in snowmelt rate and timing and the plant available water storage of the site. This work highlights the importance of not just snowmelt rate, but also that of snowmelt timing with regard to hydrologic sensitivity to climate change. Future work constraining the interaction between earlier water availability in mountainous systems and vegetation water use via long-term observations is needed to fully understand how snowmelt driven runoff production may change in the future. Our results show impacts for site scale runoff production, additional work scaling results to larger watersheds with a range of snow melt dynamics is needed. We also note that the

potential declines in water availability for plants, how this may impact plant health and drought sensitivity is another avenue for future work.

# **Chapter 3: Future Land Cover and Climate Drive Decreases in Snow Scour and Transpiration, Increasing Streamflow<sup>1</sup>**

## **Abstract**

Understanding how land-cover change will impact water resources in snow-dominated regions is of critical importance as these locations produce a disproportionate amount of runoff relative to their land area. We used the Landscape Disturbance and Succession model in conjunction with a spatially explicit, physics-based, watershed process model, the Regional Hydro-Ecologic Simulation System, to simulate land-cover change and its impact on the water balance in a 5.0 km<sup>2</sup> headwater catchment that spans the alpine-subalpine transition on the Colorado Front Range. We simulated two potential futures both with greater air temperature (+4 °C/century) and more precipitation (+15%/century; MP) or less precipitation (-15%/century; LP) from 2000 - 2100. Forest cover in the catchment increased from 72% in 2000 to 84% and 83% in 2050 and to 95% and 92% in 2100 for MP and LP, respectively. Surprisingly, increases in forest cover led to mean increases in annual streamflow production of 12 and 2 mm for MP and LP (respectively) in 2050 with an annual control streamflow of 208 mm. In 2100, mean streamflow production increased by 91 and 61 mm for MP and LP. This result counters previous work as runoff production increased with forested area, highlighting the need to better understand the impacts of forest expansion on the spatial pattern of snow scour and catchment effective precipitation.

---

<sup>1</sup> Manuscript for publication with coauthors J. Vukomanovic, P. Bourgeron, and N.P. Molotch.

Identifying the hydrologic response of mountainous areas to climate warming induced land cover change is of critical importance due to the potential water resources impacts in downstream regions.

### **3.1 Introduction**

Land cover change may influence the streamflow production of headwater catchments as increased air temperature and precipitation changes allow tree line migration and increases in forested area [Harsch *et al.*, 2009; Goulden and Bales, 2014]. Mountain and forested areas produce fresh water for two-thirds of the global population [Vörösmarty *et al.*, 2005] and produce disproportional amounts of streamflow relative to their land area [Viviroli *et al.*, 2007]. Additionally, these mountain areas are important regions for carbon sequestration [Schimel *et al.*, 2002]. In the western United States, snowmelt is the primary source of water providing for agricultural and municipal uses as well as for ground water recharge [Bales *et al.*, 2006].

Across the western United States, the timing of the spring snowmelt pulse has been observed moving earlier in the year by up to one month during the 1948 – 2002 study period [Stewart *et al.*, 2005]. This is accompanied by widespread decreases in the proportion of precipitation falling as snow in the region [Knowles *et al.*, 2006], earlier snowmelt, and decreased peak snow water equivalent (SWE) [Clow, 2010; Harpold *et al.*, 2012]. In addition to these observed trends in the mountain snowpack, simulations of snowpack across the western United States suggest widespread declines in peak snowpack volumes [Hamlet *et al.*, 2005; Mote *et al.*, 2005], which are critical as a natural fresh water reservoir to provide for summer and fall streamflow and vegetation water use. In addition

to declines in snowpack volumes, future snowmelt rates are expected to decline [Musselman *et al.*, 2017] as the timing of snowmelt occurs earlier in the spring when there is less solar radiation to drive snowmelt [Trujillo and Molotch, 2014]. These changes in snowmelt rate alone are associated with decreased streamflow production across the region with streamflow production in the Southern Rocky Mountains and Middle Rocky Mountains; the headwaters of the Colorado, Snake, and Green Rivers; having been identified as particularly sensitive to changes in snowmelt rate [Barnhart *et al.*, 2016].

Coupled with these changes in the mountain snowpack are changes in land cover driven by disturbances, such as fire and insect infestation, seed dispersion, and forest succession. However, the response of streamflow to changes in land cover is variable. Disturbance oriented studies indicate a range of streamflow responses including increased streamflow [Buma and Livneh, 2015; 2017], streamflow insensitivity [Biederman *et al.*, 2015], and potential streamflow decreases [Bart *et al.*, 2016]. A previous coupled land cover and climate change study found that streamflow decreased in the future as leaf area index and rooting depth increased [Öztürk *et al.*, 2013]; additionally, they found that streamflow decreased the most compared to the baseline simulation as forested area in the basin increased.

Previous climate change motivated hydrologic modeling work from a snow-dominated catchment has shown that as air temperature increases, streamflow decreases and occurs earlier in the year [Tague and Peng, 2013]. The increase in available energy under climate warming has been shown to decrease streamflow more than the phase change in precipitation from snow to rain, although in fully coupled simulations, these two changes would be concurrent [Foster *et al.*, 2016]. These decreases in streamflow under

warmer future conditions are often accompanied by increased evapotranspiration, which may be mediated by greater plant water use efficiency as the atmospheric concentration of CO<sub>2</sub> increases [Tague *et al.*, 2009]. Conversely, tree physiology literature suggests that warming induced increases in the vapor pressure deficit will lead to decreases in plant transpiration and productivity in the summer because of stomatal closure and that transpiration may decrease or be compensated by increases in soil evaporation [Goldstein *et al.*, 2000; Huxman *et al.*, 2003; Tague and Peng, 2013].

In mountainous environments with steep air temperature and precipitation environmental gradients, understanding the impact of land cover change on hydrology is further complicated by snow-vegetation interactions wherein new vegetation elements may decrease wind driven snow scour and increase snow depths in landscape positions with previously short and sparse vegetation [Liston *et al.*, 2002]. Previous work on the spatial variability of SWE in mountain environments has focused on the interaction between wind and terrain elements [Winstral *et al.*, 2002; Erickson *et al.*, 2005]. Much of the work on blowing snow and vegetation interactions is from Arctic environments (e.g. Liston *et al.*, [2002] and may not be applicable to mountain environments. There is also considerable uncertainty in tree line expansion around the globe with some sites experiencing tree line expansion to higher elevations and others tree line retreat to lower elevations [Harsch *et al.*, 2009].

Given the uncertainty in the impact of land cover on streamflow, evapotranspiration, and snow scour and deposition in the western United States, we ask how streamflow and evaporative fluxes from a Rocky Mountain headwater catchment may change under future climate and land cover. To address this question, we inserted future

land cover scenarios from a land cover evolution model into a spatially explicit hydrologic model to run simulations from the year 2000 to year 2100 with increases in air temperature and changes to annual precipitation. Specifically, we address how streamflow and evapotranspiration will change under these conditions and whether these changes are due to the future land cover, air temperature, precipitation, or a combination of these factors. We describe the catchment, land cover evolution model, hydrologic model, and experimental setup in Section 3.2. Results and discussion of the land cover evolution model output, hydrologic model calibration, and experiment results are included in Sections 3.3 and 3.4, respectively.

## **3.2 Methods**

To investigate how streamflow from a headwaters catchment may change in response to future changes in land cover we used the Regional Hydro-Ecologic Simulation System (RHESSys), a physics-based, spatially explicit hydrologic model, with land cover futures generated from the LANdscape DIsturbance and Succession (LANDIS-II) model, a stochastic forest land cover evolution model. We include land cover futures generated every decade from the year 2000 to year 2100 from two future climate scenarios: both with increased air temperature (+4 °C/century), one with increased precipitation (+15%, more precipitation, MP), and one with decreased precipitation (-15%, less precipitation, LP). The temperature change was chosen given the central tendency of the regional future climate projections for the western United States [*van Oldenborgh et al., 2013*]. Similarly, the precipitation change was chosen to bracket the variability in future precipitation change for the region as future precipitation change is less certain [*van Oldenborgh et al., 2013*].

A 22-year meteorology record spanning from 1990 to 2012 from an adjacent weather station was perturbed as described above and used to drive RHESSys simulations with LANDIS-II land cover for years 2000 and every decade thereafter representing future land cover conditions from 2010 through 2100. In addition, hydrologic model simulations were conducted with current land cover and perturbations only to air temperature, precipitation, and air temperature and precipitation combined, without the future land cover scenarios. Hydrologic model runs used for this experiment are presented in greater detail below. This experimental design allows the isolation of streamflow changes from land cover change and from increased air temperature and from increased or decreased precipitation. Simulations used in this modeling experiment are named descriptively to allow identification of the combination of land cover, precipitation, and air temperature used. Land cover was denoted either as current land cover (CLC) or future land cover (FLC). Air temperature was denoted as either current air temperature (CT) or future temperature (FT). Precipitation was denoted as either current precipitation (CP), more precipitation (MP), or less precipitation (LP). In addition, when appropriate, the simulation year is appended to the name. For example, a simulation named FLC\_FT\_LP 2080 would be a simulation with future land cover, future air temperature, and less future precipitation for the land cover future 2080.

### **3.2.1 Site Description**

Como Creek is a 5.0 km<sup>2</sup> headwater catchment on the Colorado Front Range (Figure 3.1) that spans the alpine-subalpine transition with approximately the upper third of the catchment consisting of alpine tundra and the lower two-thirds of the catchment consisting

of subalpine forest [Knowles *et al.*, 2015]. Como Creek spans an elevation range from 2900 – 3560 m above sea level (m a.s.l.). Of the annual precipitation that falls in the catchment, 63-75% of it falls as snow [Williams *et al.*, 2011] with, on average, 21% of the snow that falls in the alpine portion of the basin sublimating via blowing snow processes [Knowles *et al.*, 2015]. A stream gauge at the outlet of the catchment recorded discharge for water years (Oct. 1 – Sept. 30) 2004 – 2012. Meteorology observations are available for calendar years 1991 – 2012 from a station just outside the catchment boundary [Jennings *et al.*, 2017] (Figure 3.1). Additionally, observations of snow water equivalent, used to correct cold-season precipitation gauge over and under catch, are available for water years 1979-2017 (Figure 3.1).

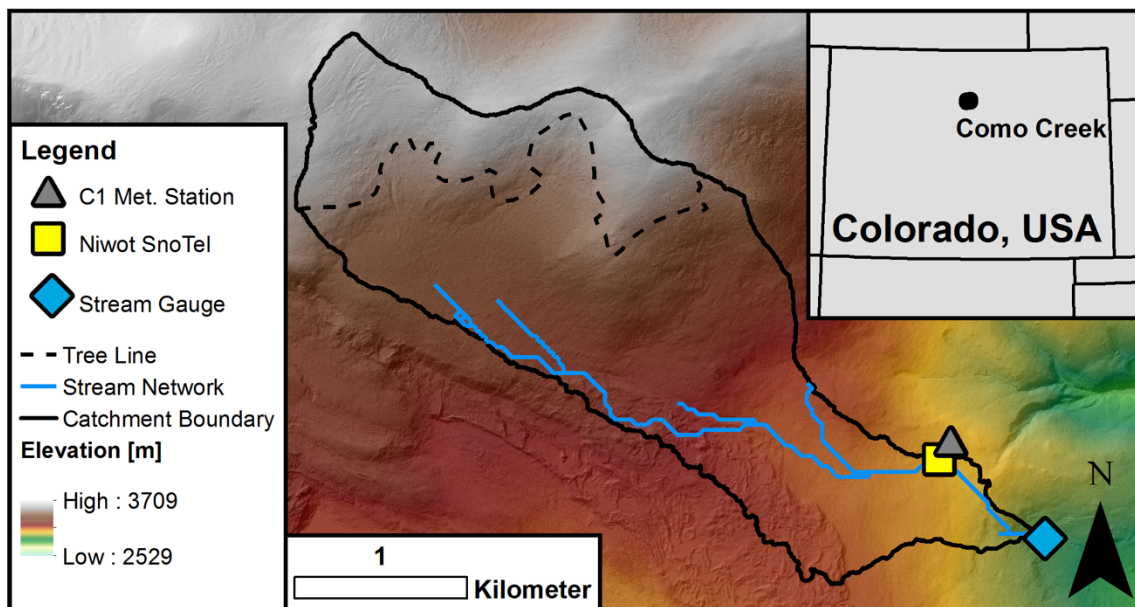


Figure 3.1: Map of the Como Creek catchment and locator map with the locations of instrumentation used.

The alpine portion of the basin is largely comprised of dry-meadow vegetation assemblages [Darrouzet-Nardi *et al.*, 2011] while the subalpine portion is a second growth mixed-conifer forest approximately 120 years old [Huxman *et al.*, 2003]. Tree species

present include *Picea engelmannii* (Engelmann spruce), *Pinus contorta* (lodgepole pine), and *Abies lasiocarpa* (subalpine fir) [Huxman *et al.*, 2003]. The bedrock of the catchment is granitic and siliceous metamorphic rock [Bilodeau *et al.*, 1987] with a glacial moraine covering the bedrock [Gable and Madole, 1976], particularly near the outlet and along the lower, southern edge of the catchment (Figure 3.1).

### 3.2.2 LANDIS-II Land Cover Simulations

The LANDscape DISTurbance and Succession II (LANDIS-II) model simulates regional-scale forest landscape disturbance, e.g. insect infestation and forest fires, forest succession, and seed dispersal [Scheller *et al.*, 2007]. LANDIS-II is able to simulate forest composition, stand age classification, aboveground biomass, and forested area expansion and contraction via forestation and disturbance, respectively. These capabilities make LANDIS-II a suitable model to provide future land cover scenarios for Como Creek. Previously, LANDIS-II has been used to study how the potential habitat ranges for eastern United States tree species under future climate scenarios [Iverson *et al.*, 2008], the impacts of microrefugia on future tree species ranges [Serra-Diaz *et al.*, 2015], climate and fire effects on forest carbon dynamics [Loudermilk *et al.*, 2013], and large-scale shifts in tree species ranges [Morin *et al.*, 2008].

For this study, LANDIS-II was run on a 50 m grid with the simulation domain covering Boulder County. The simulation time period ran from 1990 – 2100 at a ten-year time step with the initial ten years of simulation considered model spin up. As LANDIS-II simulates forest disturbance and seed dispersal stochastically, three LANDIS-II simulations were used for each future climate pathway (FT with MP and LP). The future climate

scenarios used both increased air temperature linearly increased from 0 to 4 °C by year 2100 (FT) and either a 15% increase (MP) or a 15% decrease (LP) in precipitation by year 2100 applied incrementally. For each hydrologic model simulation, perturbations to both air temperature and precipitation (Table 3.2) were applied uniformly to the daily data spanning 1990 – 2012 used to conduct each simulation. The LANDIS-II above ground biomass extension [Scheller and Mladenoff, 2004] was used for the land cover simulations to allow the transfer of LANDIS-II future land cover patterns to RHESSys. As LANDIS-II outputs are spatially explicit, LANDIS-II output for every decade of the experiment (2000-2100) were re-gridded to the 30 m cell size used in RHESSys and converted to maps of land cover type and leaf area index (LAI) using a budget for aboveground plant biomass

$$b = b_{leaf} + b_{stem} \quad (3.1)$$

where  $b$  is the total biomass,  $b_{leaf}$  is the leaf biomass, and  $b_{stem}$  is the stem biomass. We take  $r$ , the ratio of leaf to stem biomass to be

$$r = \frac{b_{leaf}}{b_{stem}} \quad (3.2)$$

Equation 3.2 can be rearranged to solve for  $b_{stem}$  such that

$$b_{stem} = \frac{b_{leaf}}{r} \quad (3.3)$$

Substituting (3.3) into (3.1) and solving for  $b_{leaf}$  gives

$$b_{leaf} = \frac{br}{1+r} \quad (3.4)$$

Leaf biomass ( $b_{leaf}$ ) was then converted to LAI using the specific leaf area (SLA) such that

$$LAI = b_{leaf} * SLA \quad (3.5)$$

The leaf-stem ratio ( $r$ ) and SLA are specified from the default RHESSys parameter file for evergreen conifer trees and are 0.0141 and 9 m<sup>2</sup>/kg, respectively.

### 3.2.3 RHESSys Hydrologic Modeling

The Regional Hydro-Ecologic Simulation System (RHESSys) is a physics-based, spatially explicit hydrologic model that simulates the accumulation and melt of snow, plant transpiration, lateral redistribution of water to adjacent model elements, and biogeochemical cycling [Tague and Band, 2004]. Additionally, RHESSys simulates subsurface water in three distinct zones covering the rooting zone, an unsaturated zone, and a shallow saturated zone. This allows RHESSys to adequately account for water in the subsurface that is available for vegetation use and drainage. RHESSys also contains a linear ground water reservoir, wherein the flux of groundwater to the stream increase linearly as ground water storage increases, to simulate deep ground water contributions to streamflow. RHESSys has been used to simulate the impacts of climate warming on watershed function [Jefferson et al., 2008; Tague and Peng, 2013; Godsey et al., 2014], the hydrologic impacts of land cover change [Bart et al., 2016; Saksa et al., 2017], and the role of groundwater in mitigating streamflow response to a warmer climate [Tague and Grant, 2009]. RHESSys has also been used to simulate the mountain snowpack in a high-elevation, mountain environment with steep gradients in temperature, precipitation, and wind redistribution [Hartman et al., 1999]. These attributes indicate that RHESSys is well suited to explore the impacts of land cover and climate change in Como Creek particularly due to the spatially explicit representation of vegetation types and properties.

#### **RHESSys Input and Simulation Construction**

In this subsection we describe the input data sets used to construct the RHESSys model used for this experiment, the forcing meteorology, addition of a loss to groundwater term,

and model parameter optimization. As Como Creek is situated at high elevation and close to the continental divide, precipitation inputs are difficult to measure because of blowing snow [Knowles *et al.*, 2015] and the spatial pattern of snow water equivalent in the area is not uniform [Jepsen *et al.*, 2012]. Since simulated streamflow is sensitive to precipitation inputs, we describe a hybrid method to distribute cold-season precipitation based on remote sensing and energy balance modeling based estimates of the spatial pattern of snow water equivalent. Additionally, because of wind scour driven relationships between vegetation and snow depth [Liston *et al.*, 2002; Blanken, 2009] we develop an empirical relationship between vegetation, elevation, and solid precipitation scaling weights to allow the formation of snow drifts and changes in snow scour under future land cover conditions. Additionally, we investigate the need for a loss to groundwater term in RHESSys to better capture the physical processes present in Como Creek.

### *Simulation Construction*

A RHESSys simulation was built for the Como Creek catchment using the 1 m LiDAR derived digital elevation model (DEM) from the Boulder Creek Critical Zone Observatory [Anderson *et al.*, 2012] aggregated to a 30 m spatial resolution by taking the mean of all the 1 m cells falling within each 30 m cell. Vegetation was parameterized using LiDAR derived estimates of leaf area index (LAI) for the Boulder Creek Critical Zone Observatory based on the methodology developed by Richardson *et al.* [2009]. As the LiDAR derived LAI does not resolve LAI in the alpine portion of the basin, we assigned grid cells in the alpine portion of the basin an LAI of  $0.5 \text{ m}^2/\text{m}^2$  [Blanken *et al.*, 2009].

### *Meteorology Forcing Data*

The RHESys simulations for this work were forced using inputs of minimum temperature (Tmin), maximum temperature (Tmax), and precipitation (P) at a daily time step over water years 1990-2012 from the adjacent C1 meteorological station [Jennings *et al.*, 2017] at 3048 m a.s.l. (Figure 3.1) distributed to a 60 m cell size grid over the catchment area. Tmin, Tmax, and P from the meteorological station were distributed based on the difference in elevation between the C1 station and the mean elevation of each grid cell following Livneh *et al.* [2014] using monthly air temperature and precipitation lapse rates from Bigler *et al.* [2007].

Warm-season (May through October) precipitation was distributed as described above; however, cold-season precipitation, which is highly prone to wind redistribution, was distributed using a map of cold-season precipitation scaling weights ( $P_w$ ) computed from a climatology of reconstructed estimates of peak snow water equivalent (RSWE) from 1996-2007 [Jepsen *et al.*, 2012] following Livneh *et al.* [2014] where the RSWE climatology grid was divided by the value of the RSWE grid cell corresponding to the C1 meteorological station to produce a grid of effective cold-season precipitation weights. Prior to distribution, cold-season C1 precipitation data were corrected for under- and over-catch against nearby snow pillow observations (Figure 3.1) following Meromy *et al.* [2015].

As the LANIDS-II simulations showed land cover change in the alpine portion of Como Creek, we investigated the relationship between snow drifts and vegetation at tree line in Como Creek. The alpine portion of Como Creek experiences mean cold season wind speeds of 13 m/s [Knowles *et al.*, 2015], which serve to transport snow and redeposit it in accordance with terrain and vegetation elements [Winstral *et al.*, 2002; Erickson *et al.*,

2005; Harpold *et al.*, 2014]. To honor the interaction of snow redistribution and vegetation in the tree line region of Como Creek (3274 – 3507 m a.s.l.), we developed a relationship between  $P_w$ , LAI, and elevation to alter the spatial pattern of cold-season precipitation weights used for the RHESSys precipitation forcing as land cover in the catchment evolves in accordance with the LANDIS-II output. This allows catchment effective precipitation, defined here as both direct precipitation to the basin and land cover induced changes in snow scour and accumulation, to evolve through time with land cover. We use the same elevation data set used to build the RHESSys simulation and Landsat derived LAI [White *et al.*, 1997] resampled to a 60 m grid cell size to match the Jepsen *et al.* [2012] derived cold-season precipitation weights (Figure 3.2). We chose to use Landsat derived LAI rather than the LiDAR derived LAI previously used because the Landsat derived LAI better captures the spatial pattern of vegetation at tree line. This relationship is used to determine the cold-season precipitation weights for each ensemble member for treed areas above 3274 m a.s.l., the lowest elevation of the diffuse krumholtz tree line in the catchment as determined by air photo analysis.

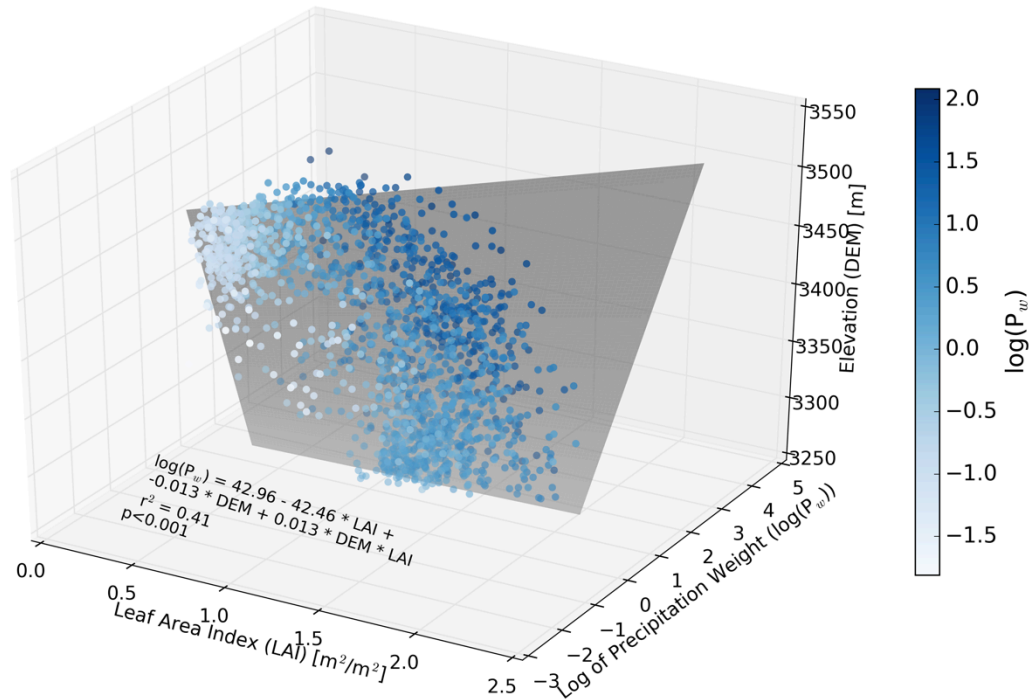


Figure 3.2: Relationship between cold season precipitation weight ( $P_w$ ), leaf area index (LAI), and elevation (DEM).

### *Loss to Ground Water*

We evaluated short- and long-term changes in subsurface water storage in Como Creek to investigate the potential for water loss to ground water from the catchment given its perched landscape position and southeastern boundary in a glacial moraine. Como Creek exhibits an unusual change in storage ( $\Delta S$ ) pattern where, over the course of five water years, only positive changes in storage were found for the catchment as a whole (Figure 3.3a) [Knowles et al., 2015]. Knowles et al. [2015] assumed a simple water balance and computed  $\Delta S$  as

$$\Delta S = P - (Q + ET + BS) \quad (3.6)$$

Where  $P$  is precipitation,  $Q$  is streamflow,  $ET$  is evapotranspiration, and  $BS$  is blowing snow. We expand upon the work of Knowles et al. [2015] by including the precipitation

estimates for Como Creek used in this study, described above, as well as by including estimates of  $\Delta S$  computed with and without the blowing snow estimates from Knowles et al. [2015] as these are highly uncertain (Figure 3.3a). Despite the precipitation estimate used and the presence or absence of sublimation from blowing snow,  $\Delta S$  for Como Creek is positive for water years 2008-2012 (Figure 3.3a). This is despite a consistent deficit in the cumulative precipitation anomaly for the catchment during that time period (Figure 3.3b). This suggests that  $\Delta S$  during this time period should be less than zero and that the catchment loses water to the ground water system.

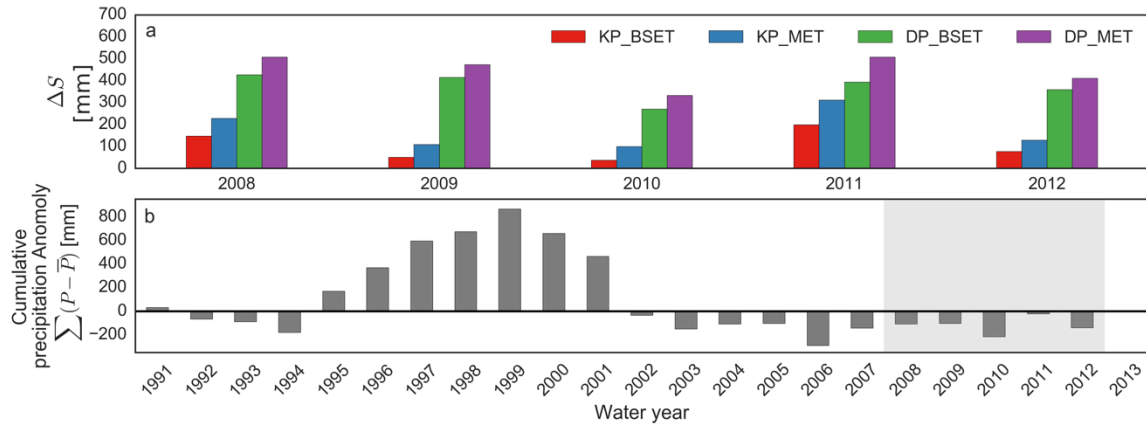


Figure 3.3: Estimates of Como Creek catchment change in storage (a). Abbreviations are as follows; Knowles et al. [2015] estimates of precipitation and catchment ET including blowing snow (KP\_BSET), Knowles et al. [2015] estimates of precipitation and measured catchment ET (KP\_MET), distributed precipitation from this study and Knowles et al. [2015] estimates of catchment ET including blowing snow (DP\_BSET) and distributed precipitation from this study and Knowles et al. [2015] measured catchment ET (DP\_MET). Cumulative precipitation anomaly for water years 1991-2013 (b) with the region that corresponds to the water years shown in (a) highlighted in grey.

To account for this loss to the regional ground water system, we added a second, non-linear reservoir to RHESSys that proportionally computes a daily flux of water leaving the catchment based on daily streamflow. We model the response curve of this reservoir as a power law such that

$$l = as^b + c \quad (3.7)$$

where  $l$  is the proportion of streamflow lost from the catchment,  $s$  is the percent of maximum streamflow, and  $a$ ,  $b$ , and  $c$  are fitting parameters controlling the shape of the loss to groundwater function. The form of (3.7) is such that as  $s$  increases,  $l$  increases non-linearly, which reflects the physical processes occurring where loss to groundwater from the catchment increases when a greater portion of the basin is saturated and head gradients in the subsurface are greater, driving greater transmission of water through the

subsurface. Similar, non-linear baseflow reservoirs are common in hydrologic modeling to represent these processes and have been used in other models [*Franchini and Pacciani, 1991; Liang et al., 1994*].

#### *3.2.3.1.4 RHESSys Model Parameter Optimization*

The parameters for the RHESSys simulation were optimized by maximizing the Nash-Sutcliffe efficiency (NSE) [*Nash and Sutcliffe, 1970*] between simulated and observed streamflow over a model training period. We chose the Shuffled Complex Evolution algorithm [*Duan et al., 1992*] to find an optimum parameter set for the training period (water years 2005-2007). Model parameters varied during the optimization procedure and optimal values are shown in Table 3.1.

Table 3.1: Parameter ranges and optimal values.

Parameter	Minimum	Maximum	Optimal	Unit
Loss to the groundwater reservoir	0.000	1.000	0.22	%
Proportion of groundwater reservoir to streamflow	0.000	1.000	0.87	%
Soil depth	0.001	50.000	24.39	m
Decay of saturated hydraulic conductivity with depth	0.004	12.000	0.72	1/m
Saturated hydraulic conductivity at the surface	0.003	1800.000	542.33	m/day
Conifer rooting depth	0.100	15.000	2.73	m
Tundra rooting depth	0.010	4.000	3.77	m
Soil pore air entry pressure	0.000	218.000	67.52	m of water
Pore size index	0.000	1.000	0.58	unitless
Minimum rain temperature	-4.000	0.000	-3.50	°C
Maximum snow temperature	0.000	4.000	3.68	°C
Snowmelt temperature coefficient	0.000	0.600	0.54	m of water / °C
Maximum snowpack energy deficit	-600.000	-0.001	-74.39	°C days
Watershed loss curve scaling parameter	0.001	15.000	10.20	unitless
Watershed loss curve shape parameter	0.001	25.000	21.23	unitless
Watershed loss curve intercept parameter	0.001	1.000	0.56	unitless
NSE	-10.85	0.73	0.73	unitless

### 3.2.4 Modeling Experiment Design

To address how coupled land cover and climate change, including both air temperature and precipitation change, will impact streamflow we first simulate a control period using six LANDIS-II simulations for year 2000 with precipitation and air temperature forcings unperturbed at current levels (Table 3.2a). All simulations are run over a period of 22 years from water year 1991 through water year 2012 (October 1, 1990

– September 30, 2012) to capture a range of interannual variability; however, we omitted the first two years of each hydrologic model simulation to allow model stores to spin-up. To test the influence of coupled land cover, increased air temperature, more precipitation (Table 3.2b), and less precipitation (Table 3.2c) we used LANDIS-II land cover futures in RHESSys for every decade from 2010 through 2100 with forcings perturbed to match the forcings used within the LANDIS-II simulations. To test the influence of increasing precipitation without land cover and air temperature change on ensembles at years 2050 and 2100 with current land cover (Table 3.2d) we used year 2000 land cover and more and less precipitation changes at 2050 and 2100. To test the influence of decreasing precipitation without land cover and air temperature change we run ensembles at years 2050 and 2100 with current land cover (Table 3.2e). To test the influence of increasing air temperature without land cover and precipitation change we run ensembles at years 2050 and 2100 with current land cover (Table 3.2f). Additionally, we mirror the coupled land cover change and air temperature and precipitation forcing perturbations (Table 3.2b,c) with ensembles with current land cover and the same air temperature and precipitation perturbations to assess the influence of land cover change independent of changes to the meteorological forcing data (Table 3.2g,h).

Table 3.2: Combinations of land cover future, simulation year, air temperature perturbation, precipitation perturbation, and number of ensemble members. Abbreviations are as follows: pseudo global warming (PGW), more precipitation (MP), less precipitation (LP), current land cover (CLC), current precipitation (CP), future land cover (FLC), current temperature (CT), current precipitation (CP), and future temperature (FT).

Land Cover Future	Simulation Year	$\Delta T$ [°C]	$\Delta P$ [%]	Ensemble Members
a. Control - current land cover, no climate warming, no precipitation change (CLC_CP_CT)				
Current (2000)	2000	0	0	6
b. Coupled land cover change, climate warming, and more precipitation (FLC_MP_FT)				
PGW_MP 2050	2050	2	7.5	3
PGW_MP 2100	2100	4	15	3
c. Coupled land cover change, climate warming, and less precipitation (FLC_LP_FT)				
PGW_LP 2050	2050	2	-7.5	3
PGW_LP 2100	2100	4	-15	3
d. Current land cover, no climate warming, and more precipitation (CLC_MP_CT)				
Current (2000)	2050	0	7.5	6
Current (2000)	2100	0	15	6
e. Current land cover, no climate warming, and less precipitation (CLC_LP_CT)				
Current (2000)	2050	0	-7.5	6
Current (2000)	2100	0	-15	6
f. Current land cover, climate warming, and no precipitation change (CLC_CP_FT)				
Current (2000)	2050	2	0	6
Current (2000)	2100	4	0	6
g. Current land cover, climate warming, and more precipitation (CLC_MP_FT)				
Current (2000)	2050	2	7.5	6
Current (2000)	2100	4	15	6
h. Current land cover, climate warming, and less precipitation (CLC_LP_FT)				
Current (2000)	2050	2	-7.5	6
Current (2000)	2100	4	-15	6

## 3.3 Results

### 3.3.1 Model Calibration

The Shuffled Complex Evolution model parameter optimization process achieved a training period NSE of 0.73 between simulated streamflow and observed streamflow (Figure 3.4).

The optimal parameter set correctly identifies the timing of peak streamflow; however, the magnitude of simulated streamflow is less than observations. Additionally, simulated baseflow is greater than observed; however, because late summer, fall and winter baseflow is so small in magnitude, these values are difficult to simulate because even a small deviation from observations results in poor objective function metrics.

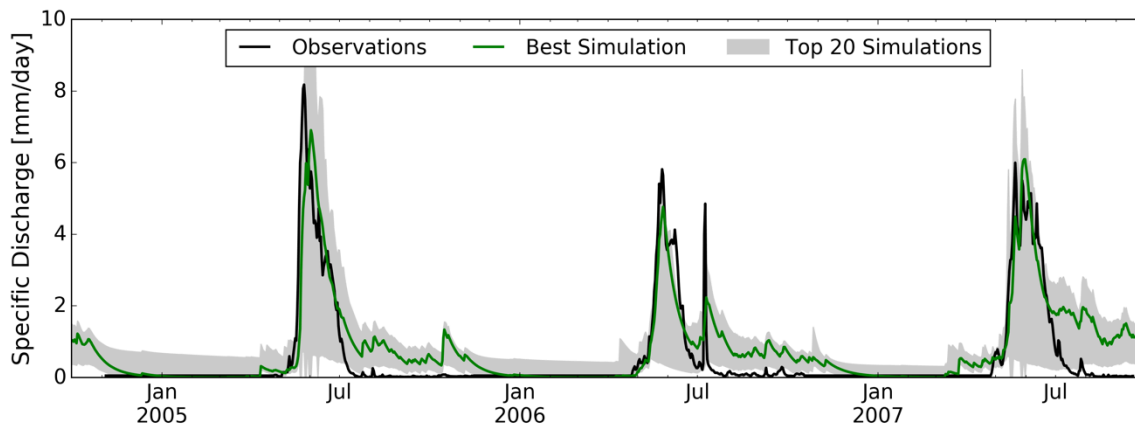


Figure 3.4: Observed and simulated streamflow in the form of specific discharge from the optimization training period. The optimal model parameter set is shown in green with the top twenty simulations shown as gray shading around the optimal parameter set.

### 3.3.2 Changes in Catchment Land Cover

Both future land cover LANDIS-II simulations with more and less precipitation by 2100 (MP and LP, respectively) show increases in watershed forested area (Figure 3.5a). Forest expansion was greater under the more precipitation scenarios and forest cover was more

variable under the less precipitation scenarios with disturbance leading to decreases in forested area in one iteration of the model during 2090. By 2100, both the MP and LP scenarios are distinctly different with no overlap between the simulations; however, up until 2090 there is considerable overlap between the two types of land cover simulations with at least one simulation from the MP scenarios having less forest cover than the simulation from the LP scenarios with the most forest cover. Mean forest biomass and catchment LAI also both increases under both the LP and MP scenarios; however, these increases are not as proportionally great at the increase in forested area, suggesting that the new forest growth is of relatively small trees (Figure 3.5 b and c).

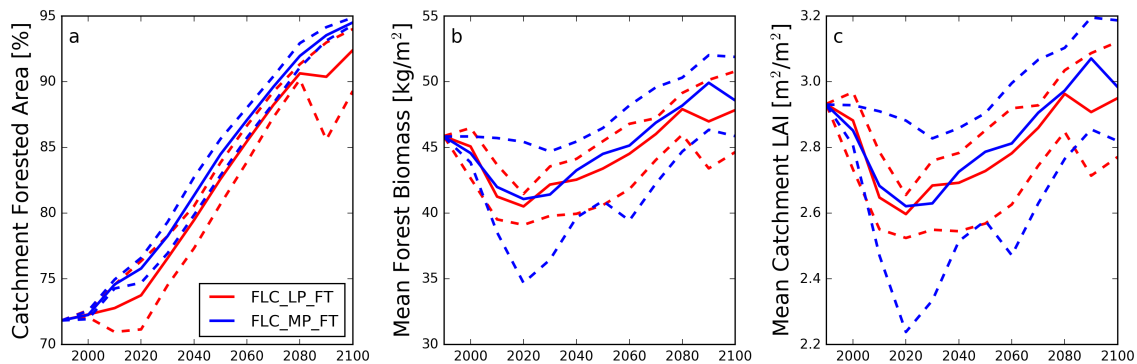


Figure 3.5: LANDIS-II simulated land cover change in the Como Creek catchment. (a) Mean forested area under future land cover (FLC) conditions with, both less precipitation (LP) and more precipitation (MP), and future temperature (FT) are show with solid lines with minimum and maximum catchment forested area shown with dashed lines. (b) Catchment mean forest biomass and (c) catchment mean LAI are also shown using the same symbology as (a).

### 3.3.3 Coupled Land Cover, Precipitation, and Air Temperature Changes

In the Como Creek basin, as forest cover expands under both MP and LP land cover change scenarios, catchment effective precipitation changes as well (Figure 3.6). Annual effective precipitation decreases by 158 mm and 62 mm (-18%, -7%) by 2050 and increases by 307

mm and 714 mm (36%, 83%) by 2100 for LP and MP scenarios, respectively (Table 3.3, Figure 3.6). The increase in catchment effective precipitation is primarily due to decreases in snow scour as the previously alpine portion of the basin is converted to forest-type vegetation (Figure 3.5a). This is shown in the gradual increase in mean peak SWE from 2060 to 2100 under both MP and LP as the land cover change driven decrease in snow scour becomes greater than peak SWE losses due to warming air temperature from 2000-2060 (Figure 3.7). By 2100, SWE has increased by an average 3% (39 mm) for MP and decreased by only 14% (-159 mm) for LP compared to decreases of 20% (-227 mm) and 24% (-275 mm) by 2060 in the MP and LP scenarios, respectively.

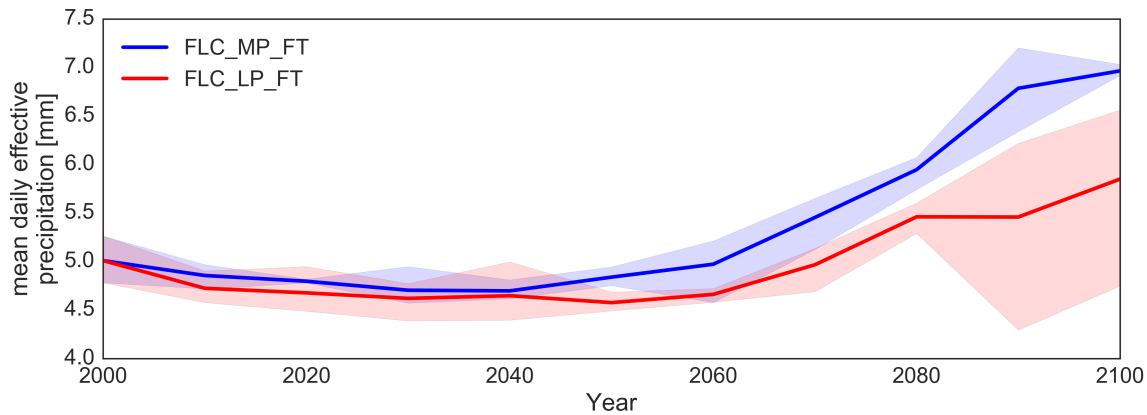


Figure 3.6: Mean daily effective precipitation in response to land cover change. Shaded regions reflect the range of land cover change ensemble members.

Table 3.3: Comparison of annual changes in streamflow, ET, loss to groundwater, and precipitation from control for all experiment simulations at 2050 and 2100.

Simulation	Change in Streamflow [mm]		Change in ET [mm]		Change in Loss to Groundwater [mm]		Change in Effective Precipitation [mm]	
	2050	2100	2050	2100	2050	2100	2050	2100
FLC_LP_FT	2	61	-8	-10	-120	301	-158	307
FLC_MP_FT	12	91	-9	-5	-55	633	-62	714
CLC_LP_CT	-5	-10	-4	-8	-108	-214	-123	-247
CLC_MP_CT	3	6	4	8	112	225	123	247
CLC_CP_FT	1	33	108	231	-79	-184	0	0
CLC_MP_FT	7	46	114	244	27	18	123	247
CLC_LP_FT	-4	16	103	217	-182	-373	-123	-247

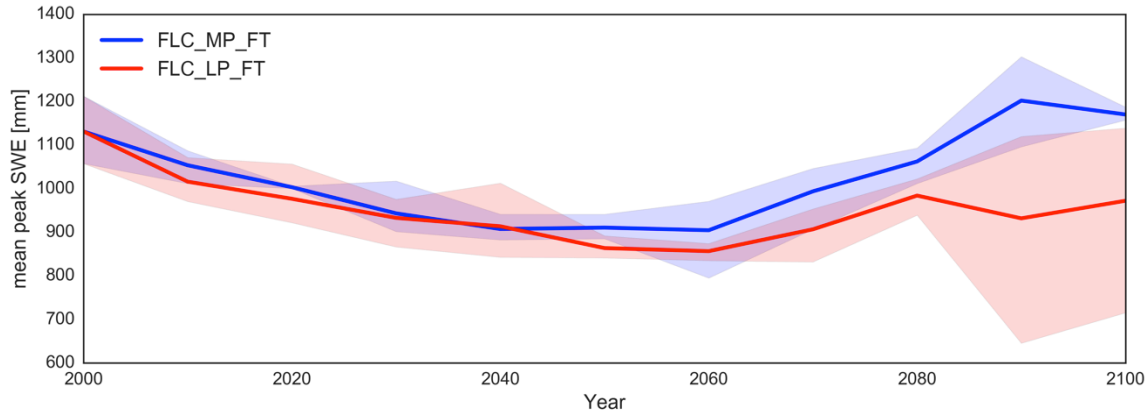


Figure 3.7: Mean peak SWE under future land cover, precipitation, and temperature. Shaded regions reflect the range of land cover change ensemble members.

In the Como Creek basin, as forest cover expands under both MP and LP land cover change scenarios, the runoff ratio of the basin increases through year 2040 to 0.13 (18%) for MP and year 2060 to 0.13 (18%) for LP (Figure 3.8). Following 2040, the MP runoff ratio declines until 2090 with an increase in Q/P occurring in year 2100 to 0.12 (9%). For LP, Q/P declines until 2080 and then increases to 0.13 (18%) by 2100; however, there is considerable variability in the LP runoff ratio after 2080 due to greater variability in forest cover in the less precipitation land cover scenarios (Figure 3.5). Although Q/P in the LP scenarios has increased more by 2100 compared to the MP scenarios, the volume of mean streamflow under the LP scenarios increased by 2 and 61 mm by 2050 and 2100, respectively, while mean streamflow increased by 12 and 91 mm by 2050 and 2100, respectively, under the MP scenarios. The above results indicate that, although the runoff ratio was greater for LP at 2100, absolute streamflow was greater for MP.

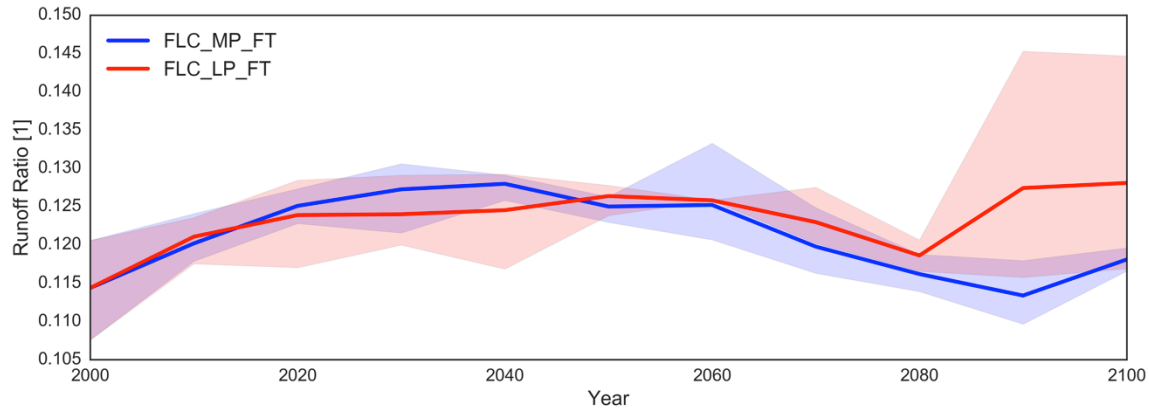


Figure 3.8: Como Creek runoff ratios under future land cover conditions including scenarios with more or less precipitation. Shaded regions reflect the range of land cover change ensemble members.

The mean monthly time series of streamflow (Figure 3.9a) shows increases in April, May, and June indicating progressively earlier snowmelt with the 2100 simulation generating earlier snowmelt than the 2050 simulation under both MP and LP scenarios. The increase in spring streamflow is offset by decreases in July and August streamflow. In both the 2050 and 2100 simulations, peak streamflow occurs approximately one month earlier with higher magnitude streamflow occurring during the 2100 simulation compared to the 2050 simulation (Figure 3.9a). There was also increased streamflow during November, December, and January, which were more pronounced during the 2100 simulation indicating that a threshold may have been crossed by this time where much of the early season precipitation is now falling as rain instead of snow. While streamflow shows changes in both the fall and spring, ET under the 2050 and 2100 simulations shows only slight increases over the control simulations until March (Figure 3.9b). Both the 2050 and 2100 simulations show increased ET in March, April, and May (21%, 35%, and 54% and 36%, 77%, and 92% for 2050 and 2100, respectively); however, after May the two simulations show decreased ET compared to the control until September. During this

period of decreased ET the 2050 simulation showed smaller decreases in ET than the 2100 simulation (Figure 3.9b).

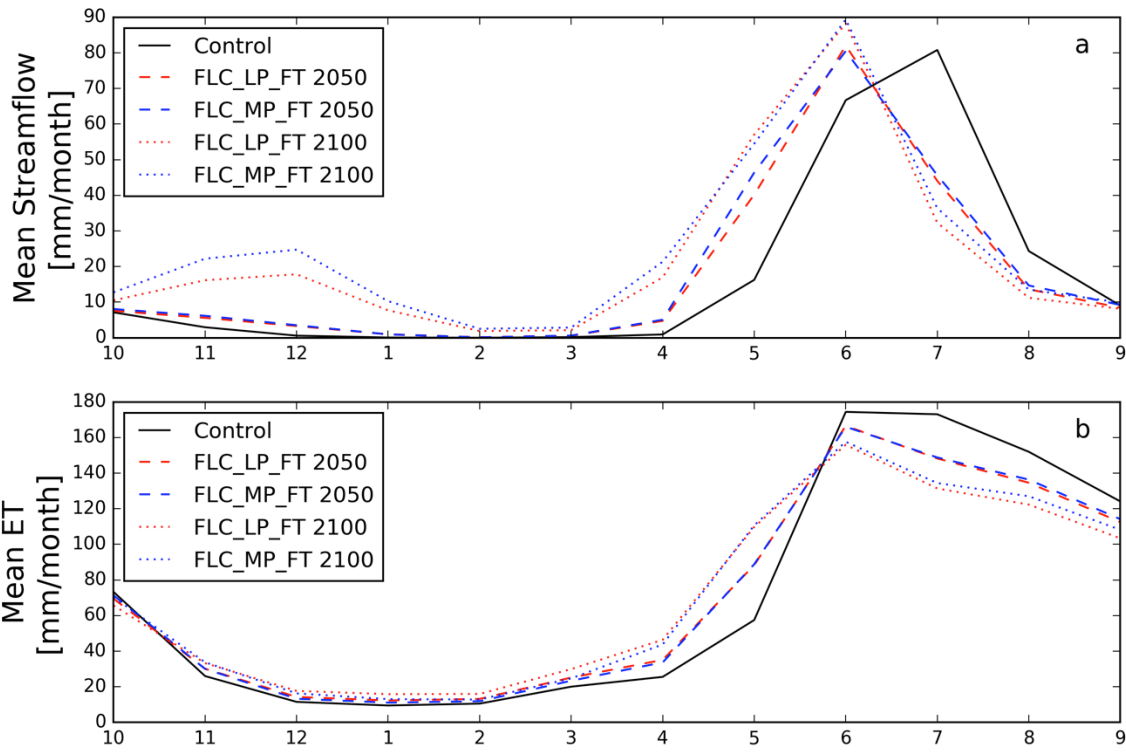


Figure 3.9: (a) Mean monthly streamflow and (b) evapotranspiration under future land cover (FLC), both more and less precipitation (MP, LP), and future temperature (FT) conditions.

For 2050 streamflow, the greatest positive changes occur in the early spring (27 and 14 mm in May and June) and are offset by similar negative changes during the summer (-36 and 10 mm in July and August, Figure 3.10a). By 2100 there are also positive streamflow changes in the fall and early winter (16 and 21 mm in November and December) in addition to greater increases in the spring (18, 40, and 22 mm in April, May, and June) and only slightly greater decreases in summer streamflow compared to 2050 (-47 and 12 mm in July and August, Figure 3.10a). The annual changes in streamflow compared to control for the 2050 and 2100 simulations are reported above. Monthly changes in ET (Figure

3.10b) show persistent increases from November to March when the increase in ET becomes greater. The change in ET becomes negative in June and persists through September for both the 2050 and 2100 simulations; however the changes in 2100 ET were more pronounced, both positive and negative, than the changes in 2050 ET. On an annual basis, mean ET decreased 9 (-1%) and 8 mm (-1%) for the MP and LP scenarios, respectively for 2050 and decreased 5 (-1%) and 10 mm (-1%) for the MP and LP scenarios, respectively for 2100.

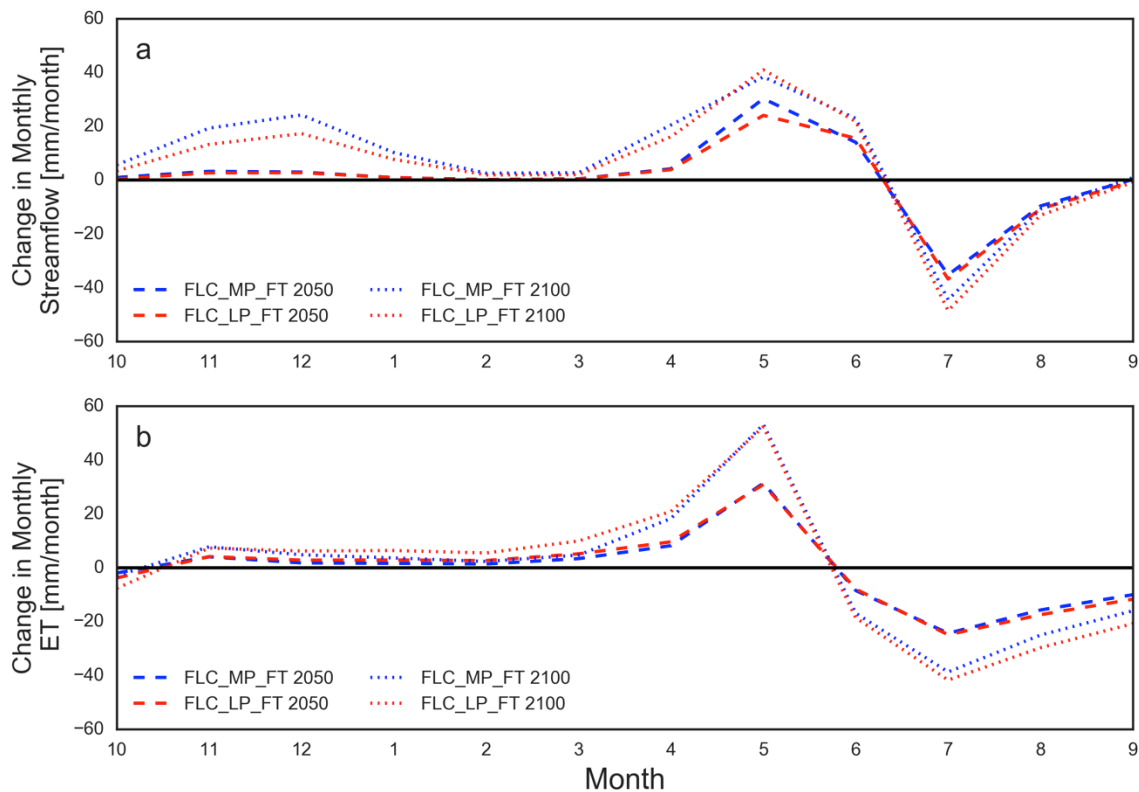


Figure 3.10: Monthly change in (a) streamflow and (b) evapotranspiration under future climate and land cover conditions compared to year 2000 land cover and climate.

### 3.3.4 Current Land Cover with Precipitation Changes

When only precipitation changes were applied to year 2000 land cover (Table 3.2) there was little effect on annual streamflow under both MP and LP scenarios. The MP scenarios

averaged 3 mm (1%) and 6 mm (3%) increases in streamflow at 2050 and 2100, respectively. The LP scenarios averaged 5 mm (-2%) and 10 mm (-5%) decreases in streamflow at 2050 and 2100, respectively. These changes in streamflow were complimented by changes in ET where the MP scenarios averaged a 4 mm (1%) and 8 mm (1%) increase in ET while the LP scenarios average ET decreased by 4 mm (0%) and 8 mm (-1%) for 2050 and 2100, respectively.

### **3.3.5 Current Land Cover with Air Temperature Changes**

When only air temperature perturbations are applied to the year 2000 land cover (Table 3.2), streamflow timing shifts progressively earlier by one month in 2050 and by one to two months by 2100 (Figure 3.11). While spring streamflow increased by 152 – 431% in March, April, and May with these temperature perturbations, there was also an increase in late fall and winter streamflow (95%, 318%, and 470% in November, December, and January) indicating that precipitation that falls during this period is falling as rain instead of snow and contributing to streamflow instead of being stored through the winter months. Increased spring streamflow was offset by decreases in summer streamflow during July and August (-43% in both months). On an annual basis, these air temperature changes translate to a 1 mm (1%) and 33 mm (16%) increases in mean streamflow by 2050 and 2100, respectively. Evapotranspiration increased 108 mm (13%) and 231 mm (27%) by 2050 and 2100, respectively. These values are balanced by decreases in loss to the regional groundwater system of 79 mm (-9%) and 184 mm (-20%).

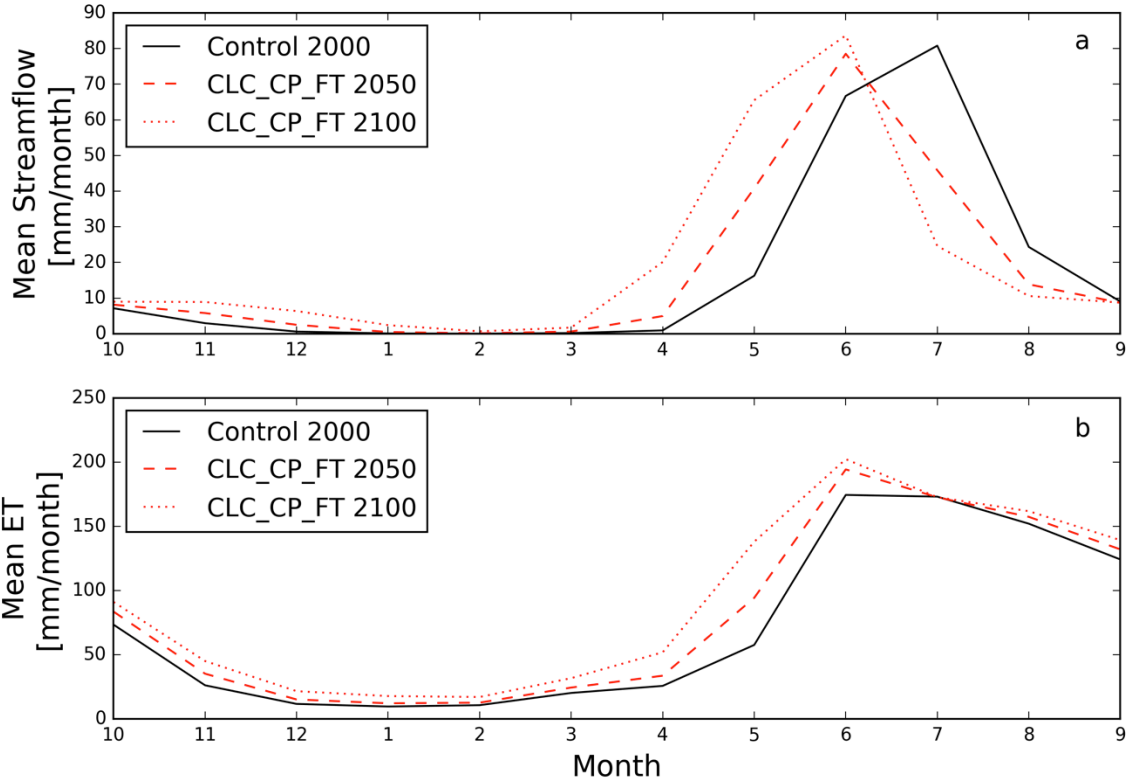


Figure 3.11: Mean monthly (a) streamflow and (b) evapotranspiration (b) from air temperature only perturbations.

### 3.3.6 Current Land Cover, Future Precipitation, and Future Temperature

Simulations with current land cover, either MP or LP, and future air temperature show the net effect of these perturbations to Como Creek without the coupled land cover change produce changes in streamflow of 7 and 46 mm for MP and -4 and 16 mm for LP at 2050 and 2100, respectively. Similarly to the simulations with only increased air temperature, streamflow occurred one month earlier at 2050 and two months earlier at 2100 (Figure 3.12a). Peak streamflow between LP and MP was very similar at 2050, while the MP scenario at 2100 increased peak streamflow above control. There were also increases in late fall and early winter streamflow, most notably under the MP 2100 scenario similar to the increased air temperature only scenario (Figure 3.12a).

At 2050 and 2100, ET increased by 114 mm and 244 mm for MP and 103 mm and 217 mm for LP. Indicating that increased air temperature at this site leads to increased ET. These increases in ET are widespread from October through March, with progressively larger increases in early spring ET under in the 2050 and 2100 scenarios for both MP and LP (Figure 3.12b). ET returns to near control levels in July, potentially indicating a more moisture-limited state during and after this time period until fall precipitation can replenish soil moisture stores (Figure 3.12b).

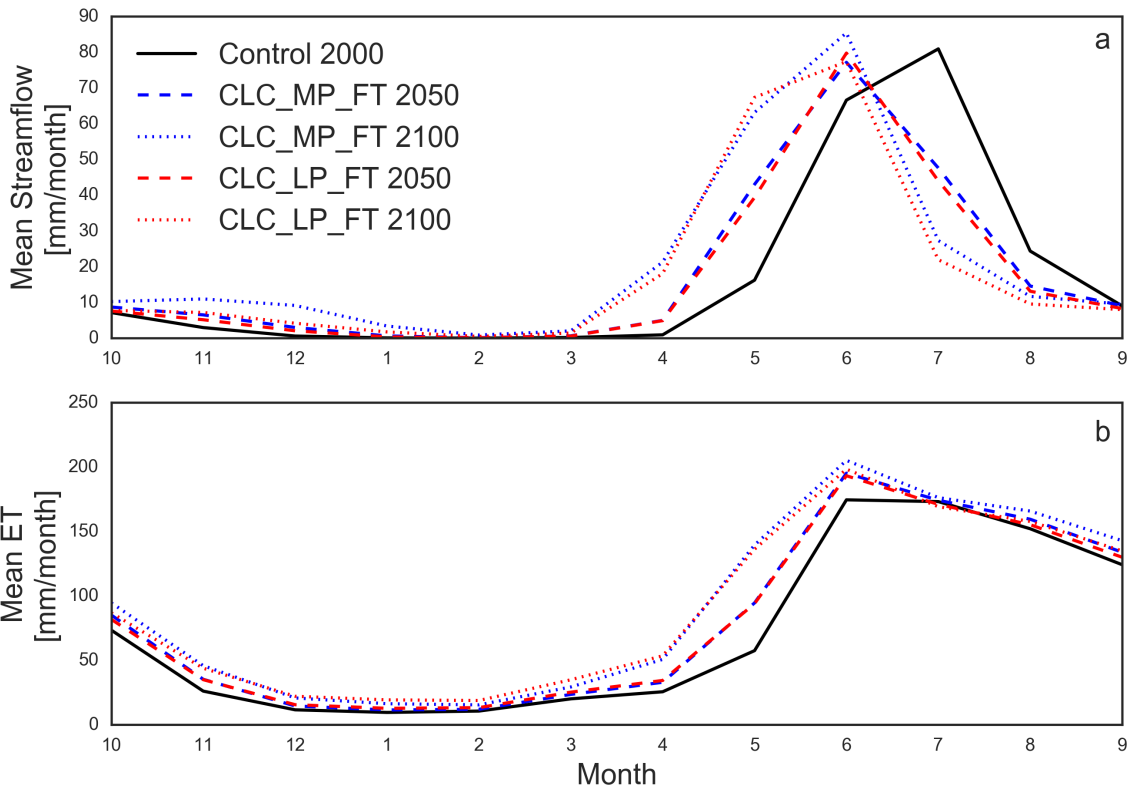


Figure 3.12: Comparison of (a) monthly streamflow and (b) evapotranspiration from simulations with current land cover, future precipitation, and future air temperature to control simulations.

### 3.3.7 Comparison of Scenarios

Comparing results across all of the simulations within this experiment illustrates which changes in streamflow, ET, and loss to groundwater were due to land cover change, air temperature increases, and changes in precipitation (Table 3.3). The largest changes observed from the simulation were to losses to groundwater from Como Creek, which were greatest under the 2100 FLC\_MP\_FT scenario (633 mm). Much of this change was due to land cover change as the CLC\_MP\_FT scenario registered only an 18 mm increase in loss to groundwater by 2100. The greatest changes in streamflow occurred at 2100 in the future land cover and temperature MP and LP scenarios with 61 mm and 91 mm of streamflow increase, respectively (Table 3.3). This is in contrast to 16 mm and 46 mm increases under the CLC\_LP\_FT and CLC\_MP\_FT scenarios, respectively (Table 3.3). This indicates that land cover change is responsible for a 45 mm (22%) increase in streamflow under both LP and MP scenarios. This is a greater increase in streamflow attributable to land cover change than under the precipitation change only simulations (CLC\_LP\_CT and CLC\_MP\_CT, Table 3.3) due to the land cover change induced decrease in snow scour (Figure 3.2), resulting in increased effective precipitation (Figure 3.6). By 2100, however, this 45 mm increase in streamflow is similar in magnitude to the 33 mm increase in streamflow from the increased air temperature only simulation (CLC\_CP\_FT) suggesting that air temperature driven shifts to earlier snowmelt timing have similar impact on streamflow production by creating a temporal mismatch between water availability and vegetation water demand in this catchment as land cover change driven increases in effective precipitation.

Evapotranspiration changes were greatest from simulations with current land cover, MP and LP, and future temperature (Table 3.3). These simulations showed ET

increases from 103-114 mm at 2050 and from 217-244 mm at 2100 compared to decreases in ET of 9 and 8 mm for MP and LP at 2050 and 5 and 10 mm at 2100 for the future land cover simulations (Table 3.3). This suggests that land cover change alters not only the streamflow response of Como Creek but also the ET response. The water remaining from the decreases in ET by 2100 is partitioned between streamflow increases (61-91 mm) and increases in the water lost to groundwater (301-633 mm, Table 3.3). These results suggest that, under future conditions, that Front Range headwater catchments may produce substantially more water for downstream use via both streamflow and additions to groundwater.

## **3.4 Discussion**

### **3.4.1 Coupled Land Cover, Precipitation, and Air Temperature Changes**

Simulations that included future land cover scenarios, changes in precipitation, and increased air temperature produced counterintuitive results in that, for MP scenarios,  $Q/P$  increased from 0.11 to 0.12 and, for LP scenarios, increased from 0.11 to 0.13 from year 2000 to year 2100. In absolute terms, this increase in proportional streamflow translates to an increase in streamflow from 209 mm in year 2000 to 300 mm and 270 mm for MP and LP scenarios, respectively, in year 2100. This increase in streamflow was driven by forest expansion in the catchment, which decreased snow scour (Figure 3.2) and resulted in catchment effective precipitation increases of 714 mm and 307 mm by 2100 for the MP and LP scenarios, respectively (Figure 3.6, Table 3.3). With 1,830 mm of average annual precipitation in the catchment at year 2000, the increase in effective precipitation by 2100

is nearly a 50% increase in annual precipitation. The integrated effect of increasing effective precipitation due to increasing forested area produces this unusual streamflow response, contrary to previous work that suggested streamflow would decrease with increased catchment forested area [Öztürk *et al.*, 2013]. We examine the streamflow and evapotranspiration underpinnings of this response below. Other workers have shown that forest area is expanding in the study area using air photo analysis [Gulick, 2016] and that forest biomass is increasing from analysis of permanent plots [Chai, 2017].

### **3.4.2 Changes in Streamflow**

Streamflow increases by 2100 were driven by two periods of increased monthly streamflow (Figure 3.10a). The first of these periods spans November through January and was present in both the MP and LP scenarios, respectively, but not to a great extent in the 2050 simulations. This suggests that shoulder season precipitation that fell as snow in 2000 and 2050 fell as rain in the 2100 simulations. The temperature threshold between which precipitation falls as snow and rain in these early, cold-season storms is crossed between 2050 and 2100. In both 2050 and 2100 there was no corresponding increase in ET during this first period of increased streamflow. Therefore, much of the precipitation that fell as rain during this period in 2100 was converted to streamflow. This conversion of shoulder-season precipitation from snow to rain is also likely happening during the spring transition; however, it is more difficult to see its direct impacts on the hydrograph because of concurrent snowmelt.

The second period of increased streamflow occurred from April to June in 2050 and from May to June in 2100 (Figure 3.10a). This period of increased streamflow is similar to

the shift in springtime streamflow from the simulations in which only air temperature was increased (Figure 3.10a). Therefore, the timing of this second period of increased streamflow in the combined land cover and climate change simulations may be attributed to the increases in air temperature. This is because by 2100, snowmelt is occurring before the vegetation in the catchment is able to utilize the water, potentially due to phenologic limitations. The magnitude of streamflow during this period, however, may be attributed to the land cover driven increases in effective precipitation in both the MP and LP scenarios (Figure 3.5).

### **3.4.3 Changes in Evapotranspiration**

As future land cover increases in both the MP and LP scenarios through time, paradoxically, the overall ET declines by 2100 (Figure 3.13). Previous work suggests that ET is expected to increase with forest cover [*Goulden and Bales, 2014*]; however, results from this site suggest the opposite. In the MP scenarios, ET was initially less than control and then became greater than control for 2020 and 2030 before becoming less than the control again through 2100 (Figure 3.13a). Similarly, for the LP scenarios, ET was initially greater than control through 2040 before becoming less than control through 2100 (Figure 3.13b). This change in ET was driven by changes in transpiration, which mirrored the overall ET response and showed a net decline by 2100 for both scenarios. Evaporation from soil, litter, and intercepted precipitation steadily increased through time with greater increases by 2100 under MP compared to LP (Figure 3.13). Snow sublimation decreased through time under both scenarios with little difference between MP and LP likely due to the air temperature driven contraction of the snow season by 2100. The net effect of these

increases in evaporation and decreases in transpiration less ET by 2100, which allows for proportional and absolute increases in streamflow by 2100 (Figure 3.8).

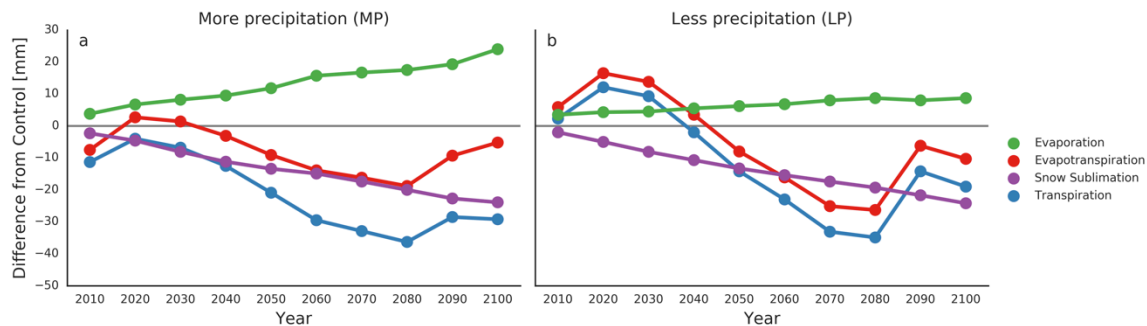


Figure 3.13: Annual differences in vapor fluxes compared to control (year 2000) under future land cover with (a) more and (b) less precipitation and future temperature scenarios. Vertical axes in (a) and (b) are the same.

Changes in the seasonal cycles of transpiration and evaporation (Figure 3.14) show how these two fluxes have been altered compared to the control scenario under future land cover and climate change scenarios. Similar to streamflow, transpiration occurs progressively earlier in the year under the 2050 and 2100 simulations with a decrease in transpiration following the spring transition (Figure 3.14a). The decrease in summer transpiration is in agreement with Huxman et al. [2003] where the warmer temperatures late in the summer do not drive additional transpiration, but instead drive increased evaporation during this time period in both the 2050 and 2100 simulations (Figure 3.14b). There is also increased evaporation during the late fall and winter due to increased atmospheric demand for water as air temperature rises by 2050 and 2100 (Figure 3.14b).

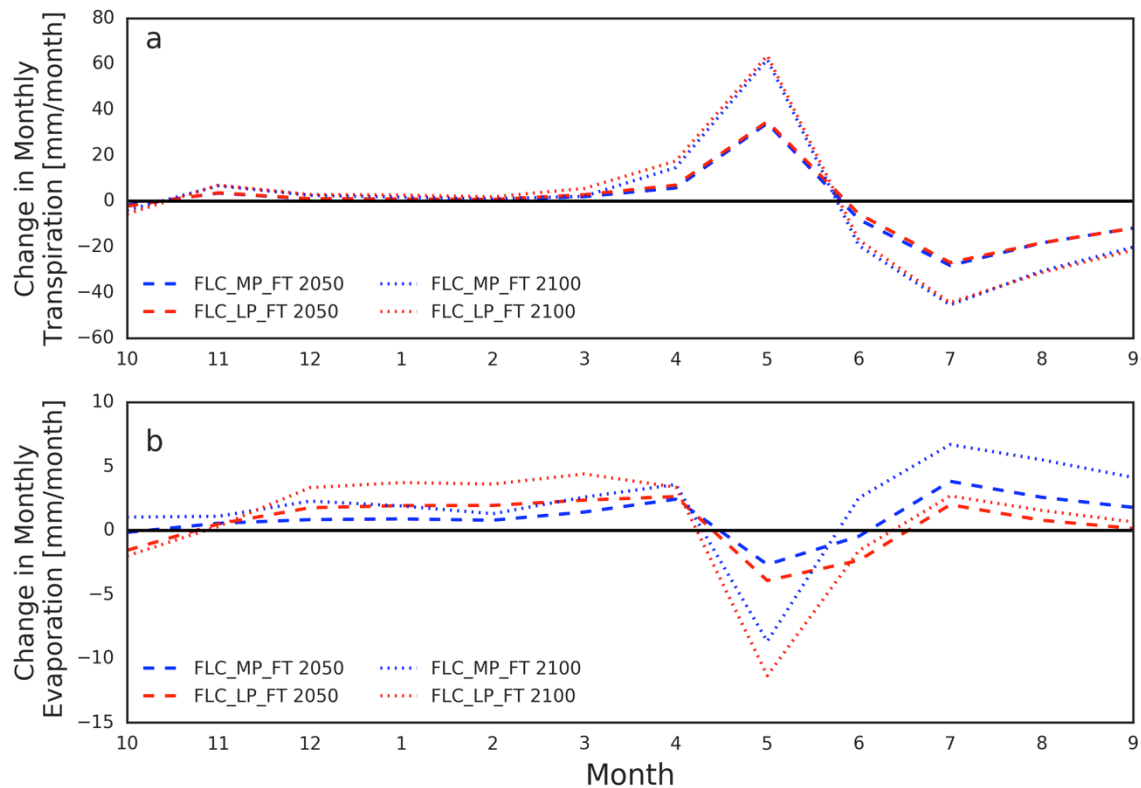


Figure 3.14: Monthly differences in (a) transpiration and (b) evaporation from the control simulations.

### 3.4.4 Implications

In high, mountainous, and windy catchments the interaction between land cover change, reduced snow scour, and increases in catchment effective precipitation produces an increase in streamflow, a counter intuitive result. Average winter wind speeds above tree line near the site are often greater than 13 m/s [Blanken *et al.*, 2009] which redistributes solid precipitation [Knowles *et al.*, 2015] into seasonally recurring patterns on the landscape [Winstral *et al.*, 2002; Erickson *et al.*, 2005]. Both Erickson *et al.* [2005] and Winstral *et al.* [2002] focused their studies on the Green Lakes Valley catchment, which is adjacent to and greater in elevation than Como Creek, but with very little vegetation; as such, they did not consider how vegetation elements could also act to trap snow. As forest

cover expands into the windy, upper portion of Como Creek, the effective precipitation in the basin increased from 1830 mm in 2000 to 2544 and 2137 mm for MP and LP scenarios, respectively by 2100. In regions where the snowpack may be insensitive to a 4 °C increase in air temperature, the interaction between greater effective precipitation due to more roughness elements high in the catchment and steep environmental gradients may produce unexpected results. We note, however, that we also see an increase in streamflow associated with a snow to rain transition during this time period, suggesting that the snowpack is not entirely insensitive to a 4 °C air temperature increase.

The alpine portion of Como Creek, with its present land cover [*Knowles et al., 2015*] is at the boundary between energy and water limited states with energy limitation occurring in wet years and water limitation occurring in dry years. As shown herein, increases in forest cover may reduce wind scour of snow from the basin (Figure 3.2) and therefore increase effective precipitation (Figure 3.6, Table 3.3). Given these increases in effective precipitation in the alpine portion of the basin energy limitation may persist or become more frequent due to increased water availability, increasing proportional streamflow for the catchment.

The change in timing of streamflow under future climate and land cover conditions in concert with the decreased evapotranspiration by 2100 suggests that the change in timing of water delivery is impacting late-season water availability for vegetation (Figure 3.13). This pattern fits in part with Jeton et al. [1996] where increased streamflow was associated with earlier water availability because vegetation may not be able to utilize so much water early in the season due to phenological limitations. The increase in streamflow by 2100 observed in Como Creek may be partially attributable to this process as we

observed a 5 and 10 mm decrease in ET by 2100 under MP and LP scenarios, respectively, and an increase in streamflow (Table 3.3). The mismatch between water availability and vegetation water use may also impact plant carbon uptake during the critical snowmelt period [Winchell *et al.*, 2016], leading to diminished forest health and susceptibility to disturbance in the future. Additionally, while these results may indicate greater streamflow in the future, the impact of earlier streamflow timing may pose challenges for reservoir management as we show streamflow increasing during both the fall and spring seasons.

### **3.5 Conclusion**

We investigated how future land cover, precipitation, and temperature changes influenced streamflow and evapotranspiration in a headwater catchment along the Colorado Front Range in the Southern Rocky Mountains from year 2000 (control) to 2100. We utilize two future land cover scenarios from the Landscape Disturbance and Succession (LANDIS-II) model. One scenario estimates future land cover changes based on a 15% increase in precipitation and a 4 °C increase in air temperature by 2100. The other scenario is based on a 15% decrease in precipitation and a 4 °C increase in air temperature. The future land cover estimates and climate scenarios were used to perturb historical hydrological simulations using the Regional Hydro-Ecologic Simulation System (RHESSys), a spatially explicit hydrologic model.

Under both the more and less precipitation land cover scenarios, the forested portion of the basin increased from 72% to nearly 95%. This caused an increase in effective precipitation from 1,830 mm in 2000 to 2,544 mm and 2,137 mm for more and less precipitation scenarios due to the interaction between blowing solid precipitation and new

vegetation roughness elements high in the catchment, which decrease wind scour of snow from the basin. During the experiment, streamflow increased from 209 mm in 2000 to 300 and 270 mm by 2100 for the more and less precipitation scenarios, reflecting the increase in precipitation and a decrease in evapotranspiration due to a mismatch between water availability and vegetation water use. We found that increased air temperature drove changes in streamflow timing and that these elevated air temperature levels also drove a phase change in fall and early winter precipitation from snow to rain that is partially responsible for increased streamflow in the catchment by 2100 as there was no evapotranspiration response to this new period of water availability.

Hydrologic model simulations using current land cover and only elevated air temperature indicated a 10.2 mm decrease in streamflow by 2050 and a 21.8 mm increase in streamflow by 2100 suggesting that greater vegetation water use is possible up to 2050 and then the temporal mismatch between water availability and vegetation water becomes too great by 2100, resulting in increased streamflow. This suggests that the streamflow response from the land cover change simulations is due to both increased effective precipitation in the catchment and a mismatch between water availability and vegetation water demand.

This work highlights the need to understand snow-vegetation interactions in the future as land cover change in areas with previously sparse vegetation may have counter intuitive hydrologic implications as described above. This may be accomplished by more nuanced land cover evolution simulations, which not only simulate biomass, but also vegetation height. Furthermore, these simulations should account for wind-driven snow vegetation interactions implicitly as these will influence water availability at tree line,

which may in turn influence seedling survival, vegetation productivity, and susceptibility to disturbance in this hydrologically critical portion of high-elevation headwaters catchments. We also did not consider how future land cover may change the spatial pattern of energy and water limitations in a catchment or how land cover and future climate may impact the overall productivity of a catchment. Understanding how these aspects of catchment function respond to changes in land cover and climate will enhance our knowledge of how biologic-hydrologic systems will respond to future conditions.

## Chapter 4: Snowmelt Rate Dictates Streamflow<sup>1</sup>

### Abstract

Declining mountain snowpack and earlier snowmelt across the western United States has implications for downstream communities. We present a possible mechanism linking snowmelt rate and streamflow generation using a gridded implementation of the Budyko framework. We computed an ensemble of Budyko streamflow anomalies (BSA) using Variable Infiltration Capacity model-simulated evapotranspiration, potential evapotranspiration, and estimated precipitation at 1/16° resolution from 1950-2013. BSA was correlated with simulated baseflow efficiency ( $r^2=0.64$ ) and simulated snowmelt rate ( $r^2=0.42$ ). The strong correlation between snowmelt rate and baseflow efficiency ( $r^2=0.73$ ) links these relationships and supports a possible streamflow generation mechanism wherein greater snowmelt rates increase subsurface flow. Rapid snowmelt may thus bring the soil to field capacity, facilitating below-root-zone percolation, streamflow, and a positive BSA. Previous works have shown that future increases in regional air temperature may lead to earlier, slower snowmelt, and hence, decreased streamflow production via the mechanism proposed by this work.

---

<sup>1</sup> Published as: Barnhart, T. B., N. P. Molotch, B. Livneh, A. A. Harpold, J. F. Knowles, and D. Schneider (2016), Snowmelt rate dictates streamflow, *Geophysical Research Letters*, 43(15), 8006–8016, doi:10.1002/2016GL069690. Reproduced here with the permission of John Wiley and Sons: License Number 4271020375886.

## 4.1 Introduction

Mountain snowpack and snowmelt-derived streamflow are a critical water resource for approximately one-sixth of the global population [Barnett *et al.*, 2005]. However, trends in observed peak snow water equivalent (SWE) and the timing of spring snowmelt indicate that the western United States (U.S.) mountain snowpack is declining and that snowmelt onset is occurring earlier in the year [Clow, 2010; Harpold *et al.*, 2012]. Correspondingly, trends in streamflow records show that snowmelt-driven streamflow is also occurring earlier in the year both in the western U.S. and globally [Cayan, 1996; Stewart *et al.*, 2004; 2005; Stewart, 2009]. These trends suggest that snowpack accumulation and melt dynamics are responding to higher near-surface air temperatures and changes in precipitation magnitude and phase driven by regional climate change [Knowles *et al.*, 2006; Luce *et al.*, 2014]. As climate change violates the critical stationarity assumption for statistical water supply forecast models [Milly *et al.*, 2008], a process-based understanding of the snowmelt-streamflow relationship, and how this relationship varies regionally, is needed to better predict water availability.

In addition to changing precipitation type, climate warming also shifts the timing of snowmelt earlier in spring [Hamlet *et al.*, 2005]. Previous work suggests that earlier snowmelt may alter streamflow production through two opposing mechanisms: (i) Earlier snowmelt, due to a warmer atmosphere, partitions a greater proportion of snowmelt to evapotranspiration (ET) than streamflow because of atmospheric warming-induced increased vapor pressure deficit (VPD) [e.g. Bosson *et al.*, 2012]. Conversely, (ii) early snowmelt disrupts the synchrony between water availability and vegetation water demand

and results in greater streamflow because water delivery occurs when vegetation is less active [Jeton *et al.*, 1996]. Recent results by Trujillo and Molotch [2014], which showed that earlier snowmelt is associated with slower snowmelt, lead us to a third hypothesis (iii) in which slower snowmelt decreases streamflow generation. This hypothesis is rooted in the soil water balance whereby snowmelt rates in excess of evapotranspiration rates may increase infiltration in excess of field capacity, leading to greater sub-surface drainage. In this way, snowmelt rate may control the relative hydrological partitioning of snowmelt between ET and streamflow production. Rapid snowmelt may thus drive subsurface flow below the root zone and/or result in melt rates that exceed infiltration rates, leading to overland flow; both mechanisms could generate high Budyko streamflow anomalies (BSA) and lead to proportionally greater streamflow. Furthermore, Hypothesis iii is consistent with previous work highlighting the coupling between snowmelt timing and peak soil moisture [Harpold and Molotch, 2015] and the distribution and magnitude of soil water for facilitating subsurface flow from variable snowmelt rates [Wilcox *et al.*, 1997; Liu *et al.*, 2004; McNamara *et al.*, 2005; Flint *et al.*, 2008; Liu *et al.*, 2008; Jencso *et al.*, 2009; Graham *et al.*, 2010; Chauvin *et al.*, 2011; Liu *et al.*, 2012; Harpold and Molotch, 2015].

In this study, we test the validity of hypothesis iii and propose a potential mechanism to explain this behavior. We do not attempt to test hypotheses i or ii in this study. We specifically investigate the relationship between snowmelt rate and streamflow production by testing to what degree (a) snowmelt rate explains Budyko-based streamflow production (BSA), (b) whether there exists a clear mechanism linking snowmelt rate to streamflow production, and (c) if regional heterogeneity in the snowmelt rate-streamflow production relationship is present across the western U.S.

## 4.2 Data and Domain

To compare the relationship between snowmelt rate and Budyko-based streamflow production, we used a gridded hydrometeorological data set [Livneh *et al.*, 2015] containing consistent daily meteorological forcings and simulated Variable Infiltration Capacity (VIC) model states and fluxes at  $1/16^\circ$  ( $\sim 6$  km) resolution from 1950-2013 [Liang *et al.*, 1994]. Daily forcing and simulated variables included station-derived precipitation (P), minimum and maximum air temperature, simulated evapotranspiration ( $ET_{VIC}$ ), potential evapotranspiration (PET), streamflow (Q), baseflow ( $Q_{bf}$ ), and SWE. Daily values of PET in VIC are calculated using the Penman-Monteith equation [Shuttleworth, 1993]. Baseflow is defined in VIC as water that passes through the soil column and is thus analogous to shallow subsurface flow. Runoff in VIC is defined as water that travels over the land surface and in the near-surface soil. Discharge (Q) is the sum of runoff and baseflow.

The VIC model has previously been applied to simulate the mountain snowpack in many studies [Hamlet and Lettenmaier, 1999; Hamlet and Huppert, 2002; Mote *et al.*, 2005; Elsner *et al.*, 2010; Vano and Lettenmaier, 2012; Vano *et al.*, 2015], and the snow model within VIC has been validated against observations [Andreadis *et al.*, 2009] and compared against other land surface models [Feng *et al.*, 2008; Chen *et al.*, 2014]. A full iterative energy balance option was selected for VIC, while an explicit frozen soil option was not selected, to ensure a conservative estimate of spring runoff magnitude and rate, acknowledging that overestimating frozen soil effects could overstate linkages between snowmelt and streamflow. Frozen soils are also rare in snow-covered, mountainous

locations because the snow acts to insulate the ground from below freezing air temperatures. The Livneh et al. [2015] dataset used for this study utilized the same VIC version number and parameterization as Livneh et al. [2013], which was validated against streamflow observations for the major river basins of the conterminous U.S. We conduct our own VIC validation in the Section 4.3.4.

We masked the Livneh et al. [2015] data set to our domain of interest, which was a composite of the major mountainous Level III ecoregions [*Commission for Environmental Cooperation*, 2006] of the western U.S. (Figure 4.1), and contained 19,983 simulation grid cells. The specific ecoregions included the Cascades, Eastern Cascades Slopes and Foothills, North Cascades, Sierra Nevada, Wasatch and Uinta Mountains, Idaho Batholith, Northern Rockies, Canadian Rockies, Southern Rockies, and Middle Rockies. We selected this domain because all these regions have appreciable snow accumulation and generate runoff for downstream communities [*Bales et al.*, 2006]. Unless otherwise stated, analyses are reported for the entire domain as a whole.

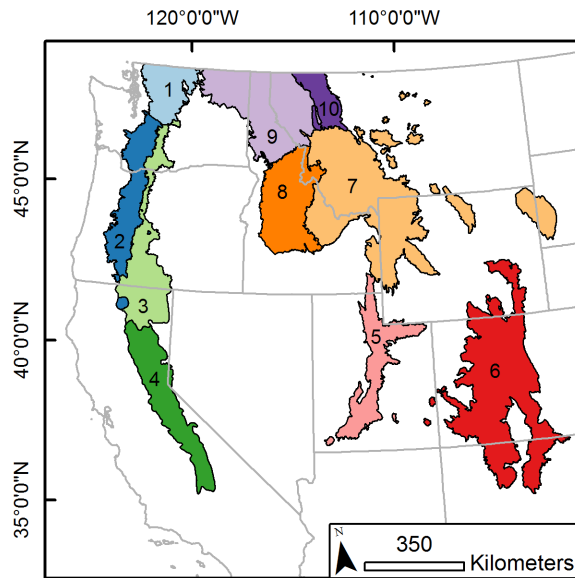


Figure 4.1: The simulation domain covers the mountainous ecoregions of the western United States. Included ecoregions are (1) North Cascades, (2) Cascades, (3) Eastern Cascades Slopes and Foothills, (4) Sierra Nevada, (5) Wasatch and Uinta Mountains, (6) Southern Rockies, (7) Middle Rockies, (8) Idaho Batholith, (9) Northern Rockies, and (10) Canadian Rockies.

### 4.3 Methods

To test hypothesis iii, we evaluated the correlation between VIC-modeled snowmelt rate and VIC-modeled BSA values for all grid cells within the domain (Figure 4.1). We then masked the domain into its component ecoregions and evaluated the inter-regional sensitivity of streamflow production to snowmelt rate. This represents an evaluation of streamflow production anomalies (Figure B.1a) that is analogous to the approach of Berghuijs et al. [2014] who used the Budyko [1974] relationship, which relates long-term ET/P to long-term PET/P. However, several works have argued that the use of universal Budyko-type functional relationships may not be appropriate over different climatic regions [Choudhury, 1999; Zhang et al., 2001; Zhou et al., 2015]. Hence, for our ecoregion-specific analysis, we also fit Zhang et al. [2001] Budyko-type equations for each ecoregion

and extracted the y-axis asymptote from these fitted Budyko-type relationships as a metric of the minimum hydrologic partitioning of precipitation to streamflow for each ecoregion (Figure B.1b). Additionally, we examined the regional variation in the BSA-snowmelt rate relationship. This approach allowed us to test the influence of snowmelt rate on Budyko streamflow production across the entire domain as well as within specific regions, using both the fitted Budyko-type equation and an ensemble of Budyko equations.

### 4.3.1 Snowmelt rate

We calculated the long-term average snowmelt rate ( $Sm_j$ ) as:

$$Sm_j = \frac{\sum \Delta SW E_{j,t}}{D_j} \quad (4.1)$$

where  $j$  is the grid cell,  $t$  is the simulation day (summed from January 1, 1950 to December 31, 2013),  $\Delta SW E_{j,t} = SW E_{j,t} - SW E_{j,t-1}$ , and  $D_j$  is the number of days where  $\Delta SW E_{j,t} < 0$ . Positive  $\Delta SW E_{j,t}$  values represent accumulation events and were forced to zero when calculating  $Sm_j$ . During the melt season we assumed that latent heat fluxes would be preferentially partitioned to melt rather than sublimation when the snowpack was isothermal [Hood *et al.*, 1999] due to the order-of-magnitude difference between the latent heats of fusion and sublimation of water (334 kJ kg<sup>-1</sup> and 2834 kJ kg<sup>-1</sup>, respectively). We also assumed negligible wind redistribution of snow across 1/16° grid cells [Tabler, 2003].

### 4.3.2 The Budyko Framework

Budyko [1974] provides a framework to compare streamflow and evaporative partitioning of different watersheds for a given amount of available energy and precipitation. This is accomplished by plotting a basin's long-term average aridity index (PET/P) on the

horizontal axis versus the long-term evaporative index (ET/P) on the vertical axis (Figure B.1a). We used an ensemble of the nine Budyko-type equations from Table 4.1 in Zhou et al. [2015], four of which incorporate fitting parameters [*Mezentsev*, 1955; *Fu*, 1981; *Choudhury*, 1999; *Zhang et al.*, 2001; 2004; *Yang et al.*, 2008; *Zhou et al.*, 2015] and five of which do not [*Schreiber*, 1904; *Ol'Dekop*, 1911; *Turc*, 1955; *Pike*, 1964; *Budyko*, 1974; *Sharif et al.*, 2007]. This type of analysis has been applied in numerous studies as an organizational framework within which to compare catchments [e.g. *Wagner et al.*, 2007; *Berghuijs et al.*, 2014; *Troch et al.*, 2015], to look at streamflow production across catchments [e.g. *Donohue et al.*, 2011], and to assess catchment-scale energy versus moisture limitation [e.g. *Jones et al.*, 2012; *Creed et al.*, 2014; *Knowles et al.*, 2015].

Accordingly, we used each Budyko-type equation from Zhou et al. [2015] to derive a theoretical ET/P, which we then compared to VIC-modeled ET/P in order to determine if a given grid cell was more or less efficient at generating streamflow than predicted by the Budyko-type equation. To relate ET/P to streamflow efficiency (Q/P), we used the long-term water balance for each grid cell, which assumes no long-term changes in storage:

$$Q = P - ET \quad (4.2)$$

and Q/P is specifically related to ET/P by:

$$\frac{Q}{P} = 1 - \frac{ET}{P} \quad (4.3)$$

Similar to Berghuijs et al. [2014], we calculated the Budyko-predicted streamflow efficiency ( $Q_{Budyko}/P$ ) for each grid cell using the long-term, simulated PET/P of each grid cell by substituting the Budyko-type equation into Equation 4.3 such that:

$$\frac{Q_{Budyko}}{P} = 1 - f\left(\frac{PET}{P}\right) \quad (4.4)$$

where  $f(\text{PET}/P)$  is one of the nine Budyko-type equations from Zhou et al. [2015].

Therefore, a grid cell with an evaporative index approaching unity partitions very little water to streamflow, while a grid cell with an evaporative index approaching zero partitions most water to streamflow. Simulated streamflow efficiency ( $Q_{VIC}/P$ ) was computed as:

$$\frac{Q_{VIC}}{P} = 1 - \frac{ET_{VIC}}{P} \quad (4.5)$$

Finally, we computed BSA (i.e. a streamflow production metric) for each grid cell as:

$$BSA = \frac{Q_{anom}}{P} = \frac{Q_{VIC}}{P} - \frac{Q_{Budyko}}{P} \quad (4.6)$$

Grid cells that plotted below the Budyko-type curve (Figure B.1a) had positive BSA values (Equation 4.6), indicating that these grid cells produced more streamflow than expected from the Budyko-type equation. Conversely, grid cells that plotted above the curve (Figure B.1a) had negative BSA values, indicating that these grid cells produced less streamflow than expected from the Budyko-type equation. For example, if a location with a positive BSA transitioned to a negative BSA, then this would represent a reduction in streamflow efficiency, which could have important implications for water availability at that location.

This approach yielded an ensemble of nine BSA estimates. For clarity, we present the mean BSA for each grid cell and the mean statistical relationships between mean BSA and snowmelt rate, baseflow efficiency ( $Q_{bf}/P$ ), and snowfall fraction as determined by linear regression. We present statistics for each BSA and independent variable combination in Appendix B.

### 4.3.3 Regional Analysis

For our regional analysis, we evaluated the correlation of VIC-derived snowmelt rate and the BSA ensemble for each ecoregion. Similar to the Budyko Framework Section, we present mean relationships and report statistics for all relationships in Appendix B. In addition, we correlated the evaporative index asymptote of the Zhang et al. [2001] Budyko-type curve, a metric of the minimum hydrologic partitioning to streamflow for each ecoregion (Figure B.1b), with mean ecoregion snowmelt rate. These two comparisons are complementary and represent two different ways of using the Budyko framework to evaluate hydrologic controls on streamflow generation. To derive asymptotes for each ecoregion, we fit the Zhang et al. [2001] Budyko-type equation for each ecoregion. We then extracted the fitted Budyko-type equation evaporative index (y-axis) asymptote (Figure B.1b). We also calculated the mean snowmelt rate for each ecoregion by taking the mean of the  $Sm_j$  values for all VIC grid cells within each ecoregion.

### 4.3.4 Model Validation

The Livneh et al. [2015] dataset was validated against observational streamflow and three gridded precipitation data sets: Daymet [Thornton et al., 1997], Maurer [Maurer et al., 2002], and the North American Land Data Assimilation System (NLDAS) [Xia et al., 2012] for 671 catchments [Newman et al., 2015]. Three precipitation datasets were used given the inherent uncertainty in precipitation estimates over mountainous terrain. We then computed the long-term streamflow coefficient (Q/P) for each catchment using VIC-simulated Q and P estimated from Livneh et al. [2015] cropped to the extent of each catchment. These VIC-derived streamflow coefficients were then compared to streamflow

coefficients generated using the observed streamflow and the three gridded precipitation datasets. The resulting VIC-simulated streamflow coefficients compared favorably against the streamflow coefficients derived using the observational data sets provided in Newman et al. [2015] with regression slopes ranging from 0.83 to 0.96 (p values < 0.001,  $r^2$  values > 0.93, Figure B.2). This demonstrates that the long-term average precipitation partitioning between ET and Q of the Livneh et al. [2015] data set was reasonable.

## **4.4 Results**

### **4.4.1 Snowmelt Rate Controls Hydrologic Partitioning**

In general, the VIC-simulated aridity and evaporative indices followed the mean Budyko curve (Figure 4.2a). However, a substantial portion of the domain fell below the curve, especially grid cells with low aridity indices; statistics for each Budyko-type equation are presented in Table B.1. The average ensemble mean BSA  $\pm$  one standard deviation for the entire domain was  $0.04 \pm 0.1$  (statistically different from zero, t-test  $p < 0.001$ ), indicating that the domain slightly over-produced streamflow for a given amount of precipitation and available energy relative to the mean Budyko curve. The domain included grid cells that both under- and over-produced streamflow with fifth and ninety-fifth percentile mean BSA values of 0.04 and 0.20, respectively (Figure 4.2b). This indicates that, while the mean was relatively close to zero, there was significant variability in streamflow production with 5% of the domain under-producing streamflow and 5% of the domain over-producing streamflow by 20% or more relative to the mean Budyko curve (Figure 4.2b).

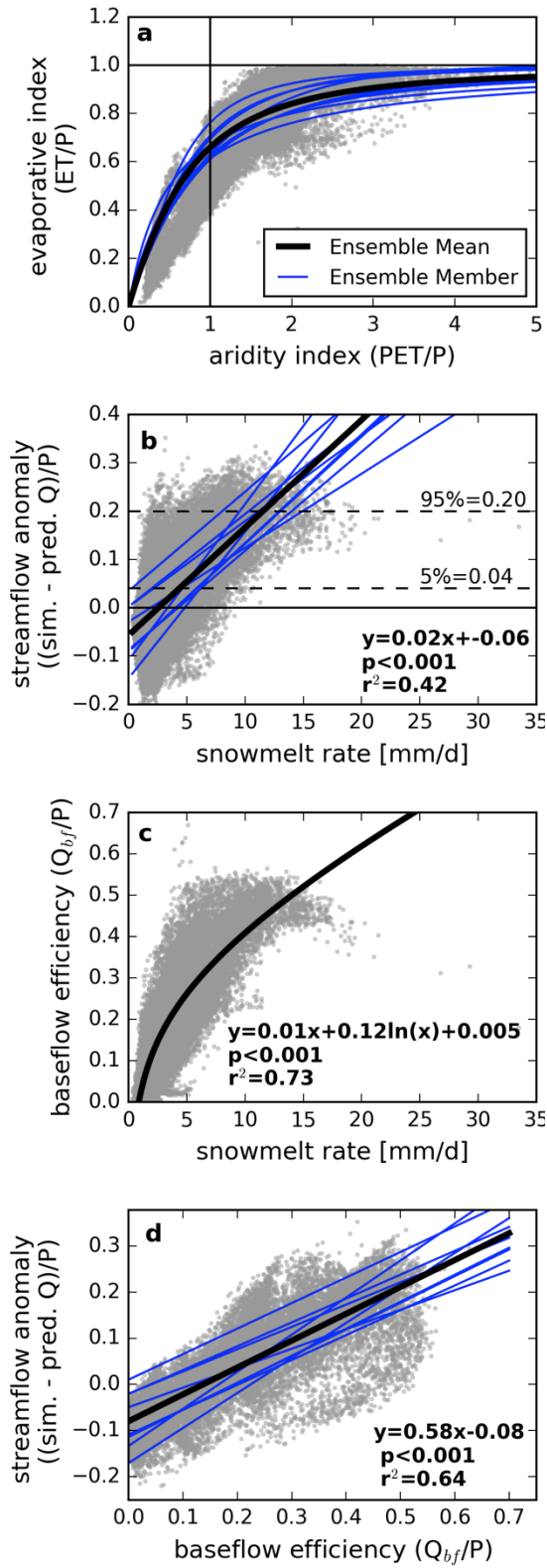


Figure 4.2: (a) Simulation grid cells (grey dots) plotted in Budyko space and the mean Budyko curve (black line). The ensemble of Budyko-type equations is shown as blue lines. (b) Relationship between snowmelt rate and mean BSA (black line). The same relationship for each Budyko-type equation is shown using blue lines. (c) Relationship between snowmelt rate and baseflow efficiency ( $Q_{bf}/P$ ). (d) Relationship between baseflow efficiency and mean BSA (black line). The same relationship for each Budyko-type equation is shown using blue lines.

The mean snowmelt rate across the domain was  $4.4 \pm 3.2$  mm d<sup>-1</sup> and the fifth and ninety-fifth percentile snowmelt rates were 1.0 and 10.7 mm d<sup>-1</sup>, respectively. Snowmelt rate significantly explained the variance in mean BSA ( $r^2=0.42$ ,  $p<0.001$ , Figure 4.2b), which demonstrates that grid cells with more rapid snowmelt often produced more streamflow than expected from the mean Budyko curve. Statistical data for the BSA-snowmelt rate relationship, for each Budyko-type equation, are given in Table B.2. We note that snowmelt rate was a poor predictor of mean BSA at snowmelt rates below 2.5 mm d<sup>-1</sup> and that mean BSA was distinctly positive at snowmelt rates above 12.5 mm d<sup>-1</sup> (Figure 4.2b).

A more complex linear regression for the mean BSA-snowmelt rate relationship ( $y=0.01x+0.06\ln(x)-0.07$ ; Figure 4.2b) yielded a slightly better fit ( $r^2$  of 0.47 compared to 0.42), but we chose to use the simple linear regression for further analysis because the slope of this linear regression is easily interpreted as a metric of the sensitivity of mean BSA to a change in snowmelt rate. Differences in the sensitivity of mean BSA to a change in snowmelt rate between ecoregions are presented in Section 4.4.2.

We also found a strong relationship between snowmelt rate and VIC-derived baseflow efficiency ( $r^2=0.73$ ,  $p<0.001$ , Figure 4.2c), linking snowmelt rate to subsurface flow production in VIC. Additionally, we found a linear relationship between baseflow efficiency and mean BSA ( $r^2=0.64$ ,  $p<0.001$ , figure 4.2d). Together, these relationships suggest that rapid snowmelt results in greater baseflow efficiency, which ultimately produces higher BSA values (Figure 4.2b-d). Statistics for the BSA-baseflow efficiency relationship for each Budyko-type equation are given in Table B.3.

#### **4.4.2 Regional Sensitivity to Changes in Snowmelt Rate**

The slope of the mean BSA-snowmelt relationship for each ecoregion shows the sensitivity of streamflow production in each ecoregion to a unit change in snowmelt rate (Figure 4.3a). Slopes for each ecoregion ranged from 0.047 in the Northern Rockies to 0.007 in the Southern Rockies. Although all relationships in Figure 4.3a were significant with  $p < 0.001$ , the amount of variance explained by each relationship varied from 74% to 9% for the Cascades and Northern Rockies, respectively. In total, eight of ten ecoregion snowmelt rate-mean BSA relationships had  $r^2 > 0.3$ . Statistical data for each snowmelt-BSA relationship and ecoregion are reported in Table B.4.

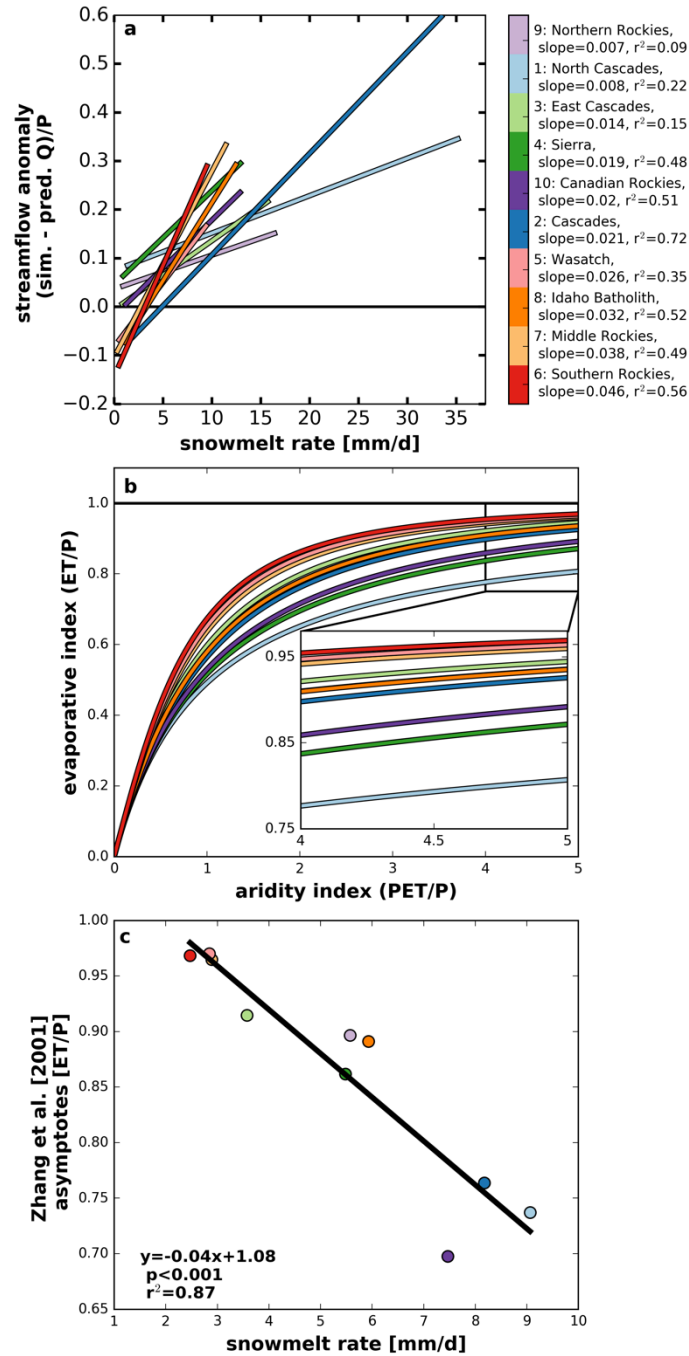


Figure 4.3: (a) Regressions between snowmelt rate and mean BSA for each ecoregion. Index numbers for each ecoregion (right) are the same as in Figure 4.1. All regressions are significant ( $p < 0.001$ ). Regression lines extend to the range of the data. (b) Zhang et al. [2001] Buydko-type equations fitted to each ecoregion with inset highlighting variability in the asymptotes. (c) Relationship between ecoregion asymptotes and mean ecoregion snowmelt rate. All panels use the same color scheme.

Fitted Zhang et al. [2001] Budyko-type equations for each ecoregion exhibited a wide range of curve asymptotes, whereby minimum partitioning to streamflow varied from 3% to 30% of precipitation (i.e. asymptotes ranged from 0.97 to 0.70; Figure 4.3b, Table B.5). The mean ecoregion snowmelt rate values for the minimum and maximum asymptotes are 2.47 and 8.18 mm d<sup>-1</sup>, respectively (Table B.5). The variability in fitted Zhang et al. [2001] asymptotes is well explained by mean ecoregion snowmelt rate ( $r^2=0.87$ ,  $p<0.001$ , Figure 4.3c).

## **4.5 Discussion**

### **4.5.1 Snowmelt Rate Controls Hydrologic Partitioning**

This work demonstrates that, across the western U.S., areas with more-rapid snowmelt over-produced streamflow relative to Budyko-type model expectations (Figure 4.2b). We showed that grid cells with rapid snowmelt also have high baseflow efficiency, which strongly correlated with mean BSA (Figure 4.2b-d). This pattern fits with our hypothesis (iii) wherein rapid snowmelt is linked to high BSA values. This pattern also suggests a potential snowmelt rate-driven streamflow generation mechanism, whereby rapid snowmelt delivers water to the soil column, bringing it above field capacity, inducing percolation below the root zone, and contributing to excess soil water. Excess soil water then leads to increased subsurface flow, which results in elevated BSA values. In contrast, when this relationship is inverted, slower snowmelt corresponds to lower, even negative, BSA values, suggesting a decrease in proportional streamflow production and greater partitioning to evapotranspiration.

We note that, especially in more rain-dominated locations, field capacity may be reached in autumn prior to the development of a snowpack thereby complicating the proposed mechanism. The snowmelt rate-excess soil water mechanism described above is also invalid when the snowmelt rate is greater than the infiltration capacity of the soil, although this scenario is unlikely in the absence of bedrock or frozen soil [Wilcox *et al.*, 1997]. The strong relationship between baseflow efficiency and mean BSA suggests that infiltration excess overland flow, i.e. runoff in VIC, is not driving high BSA values.

The analysis presented here shows that rapid snowmelt promotes greater streamflow anomalies by driving greater baseflow, which is consistent with previous snowmelt-driven streamflow analyses. Previous studies have identified lateral subsurface flow as a major contributor to streamflow in snowmelt-dominated catchments using direct measurements [Wilcox *et al.*, 1997; McNamara *et al.*, 2005; Graham *et al.*, 2010; Chauvin *et al.*, 2011]. Other studies have used hydrograph separation to infer the contribution of lateral subsurface flow to streamflow [Liu *et al.*, 2004; 2008; 2012]. In line with our potential mechanism of streamflow anomaly generation, Flint *et al.* [2008] showed that rapid snowmelt rates greater than  $1.6 \text{ cm d}^{-1}$  are capable of exceeding bedrock permeability and inducing lateral subsurface flow in the Sierra Nevada, California. Given the consistency with previous work, the snowmelt-streamflow mechanism presented here may represent a broadly applicable theory for snowmelt-driven streamflow production across the western U.S. wherein snowmelt in excess of evapotranspiration brings the soil column to field capacity and drives subsurface flow.

Snowmelt has been shown to play an important role in low summer streamflow [Godsey *et al.*, 2014]. Projections of climate warming for snow-dominated locations suggest

summertime streamflow will decrease by about 30% due to earlier snowmelt and the subsequent drawdown of shallow ground water [Huntington and Niswonger, 2012]. Our study establishes a novel mechanistic link between snowmelt rate, excess soil water, and BSA to reinforce the importance of snowmelt for streamflow production via the subsurface.

Work comparing snowmelt rates observed at snowpack telemetry sites across the western U.S. showed that earlier melt occurred at a slower melt rate because there was less solar radiation to drive snowmelt earlier in the year [Trujillo and Molotch, 2014].

Additionally, Trujillo and Molotch [2014] found that, within ecoregions of the western U.S., sites that experienced greater SWE accumulations tended to peak later in the year and that these sites also experience later, more rapid snowmelt. Due to these interrelationships, snowmelt rate thus represents an integrating metric of snowpack amount and melt timing. Furthermore, for a given soil type, runoff production due to rainfall versus snowfall inputs is dictated by the balance between the rate of water delivery – i.e. rainfall and snowmelt - and the rate of evaporative losses to the atmosphere. Our analyses, when combined with previously identified negative trends in mountain snowpack and melt rates, suggest that earlier, slower snowmelt may reduce percolation below the root zone resulting in proportionally less streamflow.

#### **4.5.2 Regional Sensitivity to Changes in Snowmelt Rate**

The relationship between the Zhang et al. [2001] asymptotes and the mean ecoregion snowmelt rates (Figure 4.3c) suggests that minimum hydrologic partitioning to streamflow is controlled by snowmelt rate. This corroborates the idea that snowmelt rate controls streamflow production via a secondary analysis. When individual ecoregion BSA-snowmelt

relationships were examined for the entire study domain (Figure 4.3a), all of the regression slopes were positive and 89 of 90 relationships had slopes significantly different from zero ( $p < 0.05$ ), indicating that decreased snowmelt rate led to an overall decrease in BSA throughout the domain.

A wide range of sensitivities of mean BSA to changes in snowmelt rate were observed across the domain (Section 4.4.3, Figure 4.3a). The significant range of explained variance by the mean BSA-snowmelt relationship for each ecoregion (9-72%) also suggests that the BSA-snowmelt relationship may be dominant in some regions, while streamflow production in other locations may be due to other mechanisms. Additionally, the observed range of sensitivities and explained variance (Figure 4.3a) may be due to variable meteorological controls on snowmelt rate and streamflow production, e.g. rain during the snowmelt season and throughout the snow free portions of the year. Alternatively, these ranges could also be the result of differences in either soil properties and depth [Flint *et al.*, 2008], elevation, and/or vegetation as represented by the parameterization of the Livneh *et al.* [2015] data set.

The combination of the asymptote-snowmelt relationship (Figure 4.3b-c) and ecoregion-specific mean BSA-snowmelt relationships (Figure 4.3a) shows an interesting pattern in snowmelt rate and streamflow production across the western U.S. Namely, ecoregions that had higher BSA sensitivities to snowmelt rate in Figure 4.3a also had lower average snowmelt rates and high asymptotes in Figure 4.3c. This may be because these ecoregions were more continental with generally shallower snowpacks that melted more slowly than maritime regions with deeper snowpacks and more rapid mean snowmelt rates [Trujillo and Molotch, 2014]. For example, the same change in snowmelt rate for a site

that generally experienced slow snowmelt (e.g. the Southern Rockies) was proportionally larger than for a site that generally experienced rapid snowmelt (e.g. the North Cascades), and the subsequent effect on streamflow production was then proportionally larger for the slow snowmelt region than for the rapid snowmelt region.

### **4.5.3 Snowmelt rate and snowfall fraction**

Berghuijs et al. [2014] attributed differences in BSA values to differences in snowfall fraction ( $r^2=0.303$ ,  $p<0.001$ ) across 420 Model Parameter Estimation Experiment (MOPEX) catchments. We also found a positive correlation between snowfall fraction (as computed in Appendix B) and mean BSA ( $r^2=0.3$ ,  $p<0.001$ , Figure B.3 and Table B.6). Earlier work, however, demonstrated that sites with greater snowfall fractions tend to have greater peak SWE [Serreze et al., 1999], and that these sites melt later and more rapidly than sites with less peak SWE [Trujillo and Molotch, 2014]. We thus propose that the relationship between snowfall fraction and BSA, found by Berghuijs et al. [2014], may be due to the collinearity between snowfall fraction and snowmelt rate ( $r^2=0.31$ ,  $p<0.001$ , Figure B.4). This relationship was robust with rain-snow temperature thresholds for Equation B.2 ranging from -2 to 2 °C ( $p<0.001$ ,  $r^2=0.20$  and  $0.40$ , respectively). In this context, snowmelt rate, as shown here, provides an explanatory mechanism for future analyses of streamflow sensitivity to snowmelt dynamics. Conversely, snowfall fraction, itself, is not a streamflow generating metric. Furthermore, the data used for this study includes landscapes with significantly greater snowfall fractions than those within the MOPEX data set used by Berghuijs et al. [2014], and, therefore, may provide a more comprehensive analysis.

## 4.6 Conclusion

Shifts toward earlier, slower snowmelt from regional warming have broad hydrologic implications in the western United States and globally. This work represents a unique, grid-cell-by-grid-cell, application of the Budyko framework to the western United States, which is accompanied by detailed regional inter-comparison using fitted Budyko-type equations. We tested the hypothesis that snowmelt rate controls Budyko streamflow anomaly and thus hydrologic partitioning of snowmelt between evapotranspiration and streamflow production. The results suggested that: (1) snowmelt rate was strongly correlated with mean Budyko streamflow anomaly across the western United States ( $r^2=0.42$ ,  $p<0.001$ ), (2) locations with high snowmelt rates had greater baseflow efficiency ( $r^2=0.73$ ,  $p<0.001$ ), (3) locations with high baseflow efficiency corresponded to greater mean Budyko streamflow anomalies ( $r^2=0.64$ ,  $p<0.001$ ), and that (4) the variance in minimum ecoregion streamflow production (i.e. Zhang et al. [2001] asymptotes) was well explained by mean ecoregion snowmelt rate ( $r^2=0.87$ ,  $p<0.001$ ). These results imply that hydrologic partitioning across the western United States may be broadly controlled by snowmelt rate and that snowmelt rate-driven soil water excess may be responsible for both observed and modeled positive Budyko streamflow anomalies. At smaller scales, western United States ecoregions exhibited a wide range of mean Budyko streamflow anomaly-snowmelt rate sensitivities highlighting the potential modulating influence of meteorology and soil properties. This study provides a means to relate future changes in snowpack to streamflow dynamics across the western United States and elsewhere, towards the goal of constraining the expected streamflow response to climate change. Future efforts should concentrate on

correctly predicting changes in snowmelt rate from warming as well as understanding the regional differences in the Budyko streamflow anomaly-snowmelt rate relationship.

## Chapter 5: Conclusion

### 5.1 Review of Findings

Understanding how changes in snowmelt rate, timing, and amount will alter runoff and streamflow production at multiple scales is important as snow-dominated, mountainous regions provide a disproportionate amount of streamflow to downstream regions compared to their land area [Viviroli *et al.*, 2007]. To investigate these relationships, this dissertation considered the snowmelt-streamflow relationship at three different scales: 1) the plot scale was addressed via an observation-based hydrologic modeling experiment designed to remove the collinearity between snowmelt rate, timing, and amount in observational data sets and to assess the sensitivity of snowmelt season runoff production and subsurface storage to changes in these snowmelt factors at two sites in the Western United States. 2) The watershed scale was addressed via a hydrologic modeling experiment designed to investigate the sensitivity of streamflow and evapotranspiration to land cover and climate change driven alterations to snowmelt in a headwater catchment on the Colorado Front Range. 3) The regional scale was addressed by leveraging a long-term simulated hydrometeorologic data set to explore the linkage between snowmelt rate and climate corrected streamflow production in ten, mountainous ecoregions in the Western United States.

These three portions of the work presented herein address the same fundamental question; how will changes in snowmelt alter water availability, be it runoff from a hillslope or plot, an integrating catchment, or a water producing region? These scales also span a

gradient in the knowledge areas they represent. At the smallest scale, the plot, the theoretical nature of the snowmelt-runoff relationship was explored using synthetic snowmelt scenarios. Although many of the combinations of snowmelt rate, timing, and amount used for this portion of the dissertation are unlikely to occur in nature, using them in a hydrologic modeling experiment allows new information on the relative impacts of changes in snowmelt rate and timing on runoff production at two different sites in the western United States. At these two sites in Colorado (CO) and California (CA), observations of runoff production and snowmelt suggest that runoff production was most sensitive to, and increased with snowmelt amount at CO and CA. However, hydrologic modeling experiment results show that snowmelt season runoff production was most sensitive to snowmelt timing with later snowmelt leading to less runoff production at CO ( $\beta = -0.31$  vs.  $0.22$  for snowmelt timing vs. rate, respectively). At CA, runoff production was most sensitive to snowmelt rate with more rapid snowmelt leading to greater runoff production ( $\beta = -0.31$  vs.  $0.67$  for snowmelt timing vs. rate, respectively). We also showed the importance of snowmelt timing and snowmelt rate to the change in snowmelt season subsurface storage at both CO and CA ( $\beta = -0.24$  vs.  $0.18$  and  $\beta = -0.474$  vs.  $0.466$  for snowmelt timing vs. rate, respectively). In this regard, snowmelt season subsurface storage at CO and CA was most sensitive to changes in snowmelt timing. Additionally, we found that the sensitivity of runoff production to changes in snowmelt rate and timing increased with greater plant available water storage at both sites.

This work shows that snowmelt season runoff losses due to slower snowmelt may be partially offset by runoff gains from earlier snowmelt. Given climate driven decreases in snowpack volumes, earlier snowmelt timing, and decreases in snowmelt rate, this work

suggests that individual site runoff production behavior will depend on the relative sensitivity of runoff at the site to changes in snowmelt rate and timing and the plant available water storage of the site. This work highlights the importance of not just snowmelt rate, but also that of snowmelt timing with regard to hydrologic sensitivity to climate change. Future work constraining the interaction between earlier water availability in mountainous systems and vegetation water use are needed to fully understand how snowmelt driven runoff production may change in the future.

At the catchment scale, more relevant to land management, the integrated effect of future land cover change and climate on streamflow was explored from year 2000 to 2100. Under both the more and less precipitation land cover change scenarios, the forested portion of the basin increased from 72% to nearly 95%. This caused an increase in effective precipitation from 1,830 mm in 2000 to 2,544 and 2,137 mm for more and less precipitation scenarios (respectively) due to the interaction between blowing solid precipitation and new vegetation roughness elements high in the catchment, which trap snow. During the experiment, streamflow increased from 209 mm in the year 2000 to 300 and 270 mm by 2100 for the more and less precipitation scenarios, respectively, reflecting the increase in precipitation and a decrease in evapotranspiration due to a mismatch between water availability and vegetation water use. We found that increased air temperature drove changes in streamflow timing and that these elevated air temperature levels also drove a phase change in fall and early winter precipitation that is partially responsible for increased streamflow in the catchment by 2100 as there was no evapotranspiration response to this new period of water availability.

Hydrologic model simulations using current land cover and only elevated air temperature indicated a 10.2 mm decrease in streamflow by 2050 and a 21.8 mm increase in streamflow by 2100 suggesting that greater vegetation water use is possible up to 2050 and then the temporal mismatch between water availability and vegetation water becomes too great by 2100, resulting in increased streamflow. This suggests that the streamflow response from the land cover change simulations is due to both increased effective precipitation in the catchment and a mismatch between water availability and vegetation demand.

This work highlights the need to understand snow-vegetation interactions in the future as land cover change in areas with previously sparse vegetation may have counter intuitive hydrologic implications as described above. This may be accomplished by more nuanced land cover evolution simulations, which not only simulate biomass, but also vegetation height. Furthermore, these land cover evolution simulations should account for wind-driven snow-vegetation interactions implicitly as these will influence water availability at tree line, which may in turn influence seedling survival, vegetation productivity, and susceptibility to disturbance in this hydrologically critical portion of high-elevation headwater catchments. We also did not consider how future land cover may change the spatial pattern of energy and water limitations in a catchment or how land cover and future climate may impact the overall productivity of a catchment. Understanding how these aspects of catchment function respond to changes in land cover and climate will enhance our knowledge of how coupled biologic-hydrologic systems will respond to future conditions.

At the regional scale, applicable to understanding large-scale shifts in streamflow production in response to changing snowmelt, climate corrected streamflow anomalies were correlated to long-term snowmelt rate. This work represents a unique, grid-cell-by-grid-cell, application of the Budyko framework to the western United States, which is accompanied by detailed regional inter-comparison using fitted Budyko-type equations. We tested the hypothesis that snowmelt rate controls Budyko streamflow anomaly and thus hydrologic partitioning of snowmelt between evapotranspiration and streamflow production. The results suggested that: (1) snowmelt rate was strongly correlated with mean Budyko streamflow anomaly across the western United States ( $r^2=0.42$ ,  $p<0.001$ ), (2) locations with high snowmelt rates had greater baseflow efficiency ( $r^2=0.73$ ,  $p<0.001$ ), (3) locations with high baseflow efficiency corresponded to greater mean Budyko streamflow anomalies ( $r^2=0.64$ ,  $p<0.001$ ), and that (4) the variance in minimum ecoregion streamflow production was well explained by mean ecoregion snowmelt rate ( $r^2=0.87$ ,  $p<0.001$ ). These results imply that hydrologic partitioning across the western United States may be broadly controlled by snowmelt rate and that snowmelt rate-driven soil water excess may be responsible for both observed and modeled positive Budyko streamflow anomalies. At smaller scales, western United States ecoregions exhibited a wide range of mean Budyko streamflow anomaly-snowmelt rate sensitivities highlighting the potential modulating influence of meteorology and soil properties. This study provides a means to relate future changes in snowpack to streamflow dynamics across the western United States and elsewhere, towards the goal of constraining the expected streamflow response to climate change. Future efforts should concentrate on correctly predicting changes in snowmelt rate

from warming as well as understanding the regional differences in the Budyko streamflow anomaly-snowmelt rate relationship.

Via investigation at these three spatial scales, this dissertation has found new relationships between snowmelt rate and timing and runoff production, at the plot scale, future land cover and climate and streamflow, at the catchment scale, and snowmelt rate and streamflow production, at the regional scale. Generally, the results presented indicate that as snowmelt rate declines so will streamflow and runoff production; however, snowmelt timing and land cover change may mediate snowmelt rate driven declines in streamflow and runoff. In both Colorado and California, earlier snowmelt timing led to increased snowmelt season runoff at the plot scale; however, at the catchment scale earlier snowmelt driven increases in streamflow also led to decreased streamflow in the late summer and decreased evapotranspiration. It should also be noted that the catchment-scale portion of this dissertation occurred in an area spanning the alpine-subalpine vegetation transition where high winds and blowing snow influence the amount of effective precipitation in the catchment. This led to counter intuitive results when investigating the effect of future land cover on streamflow, and may indicate that results from this location are not widely transferable. The increase in streamflow and runoff driven by earlier snowmelt timing; however, brings up additional questions about the implication of this work on vegetation productivity and long-term forest susceptibility to disturbance not addressed by this work.

## 5.2 Avenues for Future Work

The work presented provides for several areas of future work at the three scales considered. In Chapter 2, we found that earlier snowmelt tended to increase snowmelt season runoff. Work has been done to constrain how snowmelt rate will change in the future [Musselman *et al.*, 2017]; however, we know of no work constraining how snowmelt timing will shift in the future. Providing this additional information would allow for better constraint on the runoff response to changing snowmelt rate and timing. Additionally, at the plot scale, the synthetic snowmelt scenarios were run in an uncoupled fashion, changing only the snowmelt rate, timing, and amount, not the underlying forcings to the simulation. It would also be interesting to conduct another experiment using a coupled simulation, varying precipitation and air temperature to generate a range of snowmelt scenarios. Some control in the scenario design may be sacrificed by this approach, but it may provide another view into the effect of snowmelt rate, timing, and amount on runoff.

At the catchment scale, we have uncovered the critical role that land cover change plays on effective precipitation in an area that is influenced by snow scour and deposition via wind. These physics are not in the Landscape Disturbance and Succession model (LANDIS-II) and could feed back on plant succession and disturbance risk. Making this type of addition to LANDIS-II could improve future land cover projections. Furthermore, better constraining vegetation and snow redistribution interactions could improve estimates of how effective precipitation will change and influence streamflow production in the future. Furthermore, it would be interesting to explore future land cover change at other elevations in the Boulder Creek Critical Zone observatory and other Critical Zone

Observatories as catchments not at the alpine-subalpine transition may show different sensitivities to land cover change.

At the regional scale, we showed that different regions have different streamflow production sensitivities to unit changes in snowmelt rate; however, we could not find a unifying explanation as to what controlled these differential sensitivities between regions. Further analysis into other explanatory variables such as ecoregion hypsometry or soil parameterization may elucidate why some regions are more sensitive to a unit change in snowmelt rate. Furthermore, the domain wide analysis could be expanded to include random forest analysis to assess the importance of different factors such as land cover, elevation, and snowmelt rate, timing, and amount or the Budyko streamflow anomaly to provide a hierarchical view of factors contributing to streamflow generation at a broad spatial scale. Similarly, clustering analysis could be used with the underlying hydrometeorologic used for Chapter 4 to assess which portions of the western United States behave in hydrologically similar ways, especially with regard to their snowmelt and streamflow production.

## Bibliography

- Anderson, S. P., Q. Guo, and E. G. Parrish (2012), Snow-on and snow-off Lidar point cloud data and digital elevation models for study of topography, snow, ecosystems and environmental change at Boulder Creek Critical Zone Observatory, Colorado, *Boulder Creek CZO*, doi:10.5069/G93R0QR0.
- Andreadis, K. M., P. Storck, and D. P. Lettenmaier (2009), Modeling snow accumulation and ablation processes in forested environments, *Water Resources Research*, 45(5), 1–13, doi:10.1029/2008WR007042.
- Bales, R. C., J. W. Hopmans, A. T. O'Geen, M. Meadows, P. C. Hartsough, P. Kirchner, C. T. Hunsaker, and D. Beaudette (2011), Soil Moisture Response to Snowmelt and Rainfall in a Sierra Nevada Mixed-Conifer Forest, *Vadose Zone Journal*, 10(3), 786, doi:10.2136/vzj2011.0001.
- Bales, R. C., N. P. Molotch, T. H. Painter, M. D. Dettinger, R. Rice, and J. Dozier (2006), Mountain hydrology of the western United States, *Water Resources Research*, 42(W08432), 1–13, doi:10.1029/2005WR004387.
- Barnett, T. P., J. C. Adam, and D. P. Lettenmaier (2005), Potential impacts of a warming climate on water availability in snow-dominated regions, *Nature*, 438(7066), 303–309, doi:10.1038/nature04141.
- Barnhart, T. B., N. P. Molotch, B. Livneh, A. A. Harpold, J. F. Knowles, and D. Schneider (2016), Snowmelt rate dictates streamflow, *Geophysical Research Letters*, 43(15), 8006–8016, doi:10.1002/2016GL069690.
- Bart, R. R., C. L. Tague, and M. A. Moritz (2016), Effect of Tree-to-Shrub Type Conversion in Lower Montane Forests of the Sierra Nevada (USA) on Streamflow, edited by J. A. Jones, *PLoS ONE*, 11(8), e0161805–19, doi:10.1371/journal.pone.0161805.
- Berghuijs, W. R., R. A. Woods, and M. Hrachowitz (2014), A precipitation shift from snow towards rain leads to a decrease in streamflow, *Nature Climate Change*, 4(7), 583–586, doi:10.1038/nclimate2246.
- Biederman, J. A., A. J. Somor, A. A. Harpold, E. D. Gutmann, D. D. Breshears, P. A. Troch, D. J. Gochis, R. L. Scott, A. J. H. Meddens, and P. D. Brooks (2015), Recent tree die-off has little effect on streamflow in contrast to expected increases from historical studies, *Water Resources Research*, 51(12), 9775–9789, doi:10.1002/2015WR017401.
- Bigler, C., D. G. Gavin, C. Gunning, and T. T. Veblen (2007), Drought induces lagged tree mortality in a subalpine forest in the Rocky Mountains, *Oikos*, 116(12), 1983–1994, doi:10.1111/j.2007.0030-1299.16034.x.
- Bilodeau, S. W., D. van Buskirk, and W. L. Bilodeau (1987), Geology of Boulder, Colorado, United States of America, *Environmental and Engineering Geoscience*, xxiv(3), 289–332, doi:10.2113/gseegeosci.xxiv.3.289.
- Blanken, P. D. (2009), Designing a Living Snow Fence for Snow Drift Control, *Arctic, Antarctic, and Alpine Research*, 41(4), 418–425, doi:10.1657/1938-4246-41.4.418.
- Blanken, P. D., M. W. Williams, S. P. Burns, R. K. Monson, J. F. Knowles, K. Chowanski, and T. Ackerman (2009), A comparison of water and carbon dioxide exchange at a windy alpine tundra and subalpine forest site near Niwot Ridge, Colorado, *Biogeochemistry*,

- 95(1), 61–76, doi:10.1007/s10533-009-9325-9.
- Bosson, E., U. Sabel, L.-G. Gustafsson, M. Sassner, and G. Destouni (2012), Influences of shifts in climate, landscape, and permafrost on terrestrial hydrology, *JGR*, 117(D5), D05120–12, doi:10.1029/2011JD016429.
- Brooks, P. D., J. Chorover, Y. Fan, S. E. Godsey, R. M. Maxwell, J. P. McNamara, and C. L. Tague (2015), Hydrological partitioning in the critical zone: Recent advances and opportunities for developing transferable understanding of water cycle dynamics, *Water Resources Research*, 51(9), 6973–6987, doi:10.1002/2015WR017039.
- Budyko, M. I. (1974), *Climate and Life*, Academic Press, New York.
- Buma, B., and B. Livneh (2015), Potential Effects of Forest Disturbances and Management on Water Resources in a Warmer Climate, *Forest Science*, 61(5), 895–903, doi:10.5849/forsci.14-164.
- Buma, B., and B. Livneh (2017), Key landscape and biotic indicators of watersheds sensitivity to forest disturbance identified using remote sensing and historical hydrography data, *Environmental Research Letters*, 12(7), doi:10.1088/1748-9326/aa7091.
- Cayan, D. R. (1996), Interannual climate variability and snowpack in the western United States, *Journal of Climate*, 9(5), 928–948, doi:10.1175/1520-0442(1996)009<0928:ICVASI>2.0.CO;2.
- Cayan, D. R., S. A. Kammerdiener, M. D. Dettinger, J. M. Caprio, and D. H. Peterson (2001), Changes in the onset of spring in the western United States, *Bull. Amer. Meteor. Soc.*, 399–415.
- Chai, R. K. (2017), Influences of Stand Development and Climate on Above-Ground Biomass in Subalpine Forest Permanent Plots in the Colorado Front Range, 1–51 pp. Boulder, 23 April.
- Chauvin, G. M., G. N. Flerchinger, T. E. Link, D. Marks, A. H. Winstral, and M. S. Seyfried (2011), Long-term water balance and conceptual model of a semi-arid mountainous catchment, *Journal of Hydrology*, 400(1-2), 133–143, doi:10.1016/j.jhydrol.2011.01.031.
- Chen, F. et al. (2014), Modeling seasonal snowpack evolution in the complex terrain and forested Colorado Headwaters region: A model intercomparison study, *Journal of Geophysical Research: Atmospheres (1984–2012)*, 119(13), 13795–13819, doi:10.1002/(ISSN)2169-8996.
- Choudhury, B. J. (1999), Evaluation of an empirical equation for annual evaporation using field observations and results from a biophysical model, *Journal of Hydrology*, 216(1-2), 99–110, doi:10.1016/S0022-1694(98)00293-5.
- Christensen, L., C. L. Tague, and J. S. Baron (2008), Spatial patterns of simulated transpiration response to climate variability in a snow dominated mountain ecosystem, *Hydrol. Process.*, 22(18), 3576–3588, doi:10.1002/hyp.6961.
- Clow, D. W. (2010), Changes in the Timing of Snowmelt and Streamflow in Colorado: A Response to Recent Warming, *Journal of Climate*, 23(9), 2293–2306, doi:10.1175/2009JCLI2951.1.
- Commission for Environmental Cooperation (2006), Ecological regions of North America - Levels I, II, and III, *Commission for Environmental Cooperation*, (1:10,000,000).
- Cowie, R. M., J. F. Knowles, K. R. Dailey, M. W. Williams, T. J. Mills, and N. P. Molotch (2017), Sources of streamflow along a headwater catchment elevational gradient, *Journal of*

- Hydrology*, 549, 163–178, doi:10.1016/j.jhydrol.2017.03.044.
- Creed, I. F. et al. (2014), Changing forest water yields in response to climate warming: Results from long-term experimental watershed sites across North America, *Global Change Biology*, n/a–n/a, doi:10.1111/gcb.12615.
- Darrouzet-Nardi, A., J. Erbland, W. D. Bowman, J. Savarino, and M. W. Williams (2011), Landscape-level nitrogen import and export in an ecosystem with complex terrain, Colorado Front Range, *Biogeochemistry*, 109(1-3), 271–285, doi:10.1007/s10533-011-9625-8.
- Dingman, S. L. (2002), *Physical Hydrology*, Prentice-Hall, Upper Saddle River, NJ.
- Donohue, R. J., M. L. Roderick, and T. R. McVicar (2011), Assessing the differences in sensitivities of runoff to changes in climatic conditions across a large basin, *Journal of Hydrology*, 406(3-4), 234–244, doi:10.1016/j.jhydrol.2011.07.003.
- Duan, Q., S. Sorooshian, and V. Gupta (1992), Effective and efficient global optimization for conceptual rainfall-runoff models, *Water Resources Research*, 28(4), 1015–1031, doi:10.1029/91WR02985.
- Duan, Q., S. Sorooshian, and V. K. Gupta (1994), Optimal use of the SCE-UA global optimization method for calibrating watershed models, *Journal of Hydrology*, doi:https://doi.org/10.1016/0022-1694(94)90057-4.
- Elsner, M. M., L. Cuo, N. Voisin, J. S. Deems, A. F. Hamlet, J. A. Vano, K. E. B. Mickelson, S.-Y. Lee, and D. P. Lettenmaier (2010), Implications of 21st century climate change for the hydrology of Washington State, *Climatic Change*, 102(1-2), 225–260, doi:10.1007/s10584-010-9855-0.
- Erickson, T. A., M. W. Williams, and A. Winstral (2005), Persistence of topographic controls on the spatial distribution of snow in rugged mountain terrain, Colorado, United States, *Water Resources Research*, 41(4), 1–17, doi:10.1029/2003WR002973.
- Feng, X., A. Sahoo, K. Arsenault, P. Houser, Y. Luo, and T. J. Troy (2008), The Impact of Snow Model Complexity at Three CLPX Sites, *J. Hydrometeor*, 9(6), 1464–1481, doi:10.1175/2008JHM860.1.
- Flint, A. L., L. E. Flint, and M. D. Dettinger (2008), Modeling Soil Moisture Processes and Recharge under a Melting Snowpack, *Vadose Zone Journal*, 7(1), 350–357, doi:10.2136/vzj2006.0135.
- Foster, L. M., L. A. Bearup, N. P. Molotch, P. D. Brooks, and R. M. Maxwell (2016), Energy budget increases reduce mean streamflow more than snow–rain transitions: using integrated modeling to isolate climate change impacts on Rocky Mountain hydrology, *Environmental Research Letters*, 11(4), 1–10, doi:10.1088/1748-9326/11/4/044015.
- Franchini, M., and M. Pacciani (1991), Comparative-Analysis of Several Conceptual Rainfall Runoff Models, *Journal of Hydrology*, 122(1-4), 161–219, doi:10.1016/0022-1694(91)90178-K.
- Fu, B. P. (1981), On the calculation of the evaporation from land surface [in Chinese], *Sci. Atmos. Sin.*, 5(1), 23–31.
- Gable, D. J., and R. F. Madole (1976), Geologic map of the Ward quadrangle, Boulder County, CO. U.S., *United States Geological Survey*, (1:24000).
- Garcia, E. S., and C. L. Tague (2015), Subsurface storage capacity influences climate–evapotranspiration interactions in three western United States catchments, *Hydrol. Earth Syst. Sci.*, 19(12), 4845–4858, doi:10.5194/hess-19-4845-2015.
- Godsey, S. E., J. W. Kirchner, and C. L. Tague (2014), Effects of changes in winter snowpacks

- on summer low flows: case studies in the Sierra Nevada, California, USA, *Hydrol. Process.*, 28(19), 5048–5064, doi:10.1002/hyp.9943.
- Goldstein, A. H., N. E. Hultman, J. M. Fracheboud, M. R. Bauer, J. A. Panek, M. Xu, Y. Qi, A. B. Guenther, and W. Baugh (2000), Effects of climate variability on the carbon dioxide, water, and sensible heat fluxes above a ponderosa pine plantation in the Sierra Nevada (CA), *Agricultural and Forest Meteorology*, 101(2-3), 113–129, doi:10.1016/s0168-1923(99)00168-9.
- Goulden, M. L., and R. C. Bales (2014), Mountain runoff vulnerability to increased evapotranspiration with vegetation expansion, *Proceedings of the National Academy of Sciences*, 111(39), 14071–14075, doi:10.1073/pnas.1319316111.
- Graham, C. B., W. van Verseveld, H. R. Barnard, and J. J. McDonnell (2010), Estimating the deep seepage component of the hillslope and catchment water balance within a measurement uncertainty framework, *Hydrol. Process.*, 24(25), 3631–3647, doi:10.1002/hyp.7788.
- Grant, G. E., C. L. Tague, and C. D. Allen (2013), Watering the forest for the trees: an emerging priority for managing water in forest landscapes, *Frontiers in Ecology and the Environment*, 11(6), 314–321, doi:10.1890/120209.
- Gulick, E. (2016), Analyzing heterogeneous landscapes to reveal ecological processes (Undergraduate Honors Thesis), 1–38 pp. University of Colorado, Boulder.
- Guo, Q., and R. C. Bales (2012), Snow-on and snow-off Lidar point cloud data and digital elevation models for study of topography, snow, ecosystems and environmental change at Southern Sierra Critical Zone Observatory, California, *Southern Sierra CZO*, doi:10.5069/G9BP00QB.
- Hamlet, A. F., and D. Huppert (2002), Economic value of long-lead streamflow forecasts for Columbia River hydropower, *Journal of Water Resources Planning and Management*, 128(2), 91–101, doi:10.1061/(ASCE)0733-9496(2002)128:2(91).
- Hamlet, A. F., P. W. Mote, M. P. Clark, and D. P. Lettenmaier (2005), Effects of Temperature and Precipitation Variability on Snowpack Trends in the Western United States, *Journal of Climate*, 18(21), 4545–4561, doi:10.1175/JCLI3538.1.
- Hamlet, A., and D. Lettenmaier (1999), Columbia River Streamflow Forecasting Based on ENSO and PDO Climate Signals, *Journal of Water Resources Planning and Management*, 125(6), 333–341, doi:10.1061/(ASCE)0733-9496(1999)125:6(333).
- Harpold, A. A. et al. (2014), LiDAR-derived snowpack data sets from mixed conifer forests across the Western United States, *Water Resources Research*, 50(3), 2749–2755, doi:10.1002/2013WR013935.
- Harpold, A. A., and N. P. Molotch (2015), Sensitivity of soil water availability to changing snowmelt timing in the western US, *Geophysical Research Letters*, 42(19), 8011–8020, doi:10.1002/2015gl065855.
- Harpold, A. A., P. Brooks, S. Rajagopal, I. Heidbuchel, A. Jardine, and C. Stielstra (2012), Changes in snowpack accumulation and ablation in the intermountain west, *Water Resources Research*, 48(W11501), 1–11, doi:http://dx.doi.org/10.1029/2012WR011949.
- Harsch, M. A., P. E. Hulme, M. S. McGlone, and R. P. Duncan (2009), Are treelines advancing? A global meta-analysis of treeline response to climate warming, *Ecology Letters*, 12(10), 1040–1049, doi:10.1111/j.1461-0248.2009.01355.x.
- Hartman, M. D., J. S. Baron, R. B. Lammers, D. W. Cline, L. E. Band, G. E. Liston, and C. L.

- Tague (1999), Simulations of snow distribution and hydrology in a mountain basin, *Water Resources Research*, 35(5), 1587–1603, doi:10.1029/1998WR900096.
- Holbrook, W. S., C. S. Riebe, M. Elwaseif, J. L. Hayes, K. Basler-Reeder, D. L. Harry, A. Malazian, A. Dosseto, P. C. Hartsough, and J. W. Hopmans (2014), Geophysical constraints on deep weathering and water storage potential in the Southern Sierra Critical Zone Observatory, *Earth Surface Processes and Landforms*, 39(3), 366–380, doi:10.1002/esp.3502.
- Hood, E., M. Williams, and D. Cline (1999), Sublimation from a seasonal snowpack at a continental, mid-latitude alpine site, *Hydrol. Process.*, 13(12-13), 1781–1797, doi:10.1002/(SICI)1099-1085(199909)13:12/13<1781::AID-HYP860>3.0.CO;2-C.
- Hunsaker, C. T., T. W. Whitaker, and R. C. Bales (2012), Snowmelt runoff and water yield along elevation and temperature gradients in California's southern Sierra Nevada, *JAWRA Journal of the American Water Resources Association*, 48(4), 667–678, doi:10.1111/j.1752-1688.2012.00641.x.
- Huntington, J. L., and R. G. Niswonger (2012), Role of surface-water and groundwater interactions on projected summertime streamflow in snow dominated regions: An integrated modeling approach, *Water Resources Research*, 48(11), 1–20, doi:10.1029/2012WR012319.
- Huxman, T. E., A. A. Turnipseed, J. P. Sparks, P. C. Harley, and R. K. Monson (2003), Temperature as a control over ecosystem CO<sub>2</sub> fluxes in a high-elevation, subalpine forest, *Oecologia*, doi:10.1007/s00442-002-1131-1.
- IPCC (2014), *Climate Change 2014: Synthesis Report*, edited by Core Writing Team, R. K. Pachauri, and L. A. Meyer, IPCC, Geneva, Switzerland.
- Iverson, L. R., A. M. Prasad, S. N. Matthews, and M. Peters (2008), Estimating potential habitat for 134 eastern US tree species under six climate scenarios, *Forest Ecology and Management*, 254(3), 390–406, doi:10.1016/j.foreco.2007.07.023.
- Jefferson, A., A. W. Nolin, S. Lewis, and C. L. Tague (2008), Hydrogeologic controls on streamflow sensitivity to climate variation, *Hydrol. Process.*, 22(22), 4371–4385, doi:10.1002/hyp.7041.
- Jencso, K. G., B. L. McGlynn, M. N. Gooseff, S. M. Wondzell, K. E. Bencala, and L. A. Marshall (2009), Hydrologic connectivity between landscapes and streams: Transferring reach- and plot-scale understanding to the catchment scale, *Water Resources Research*, 45(4), 1944–1973, doi:10.1029/2008WR007225.
- Jennings, K., T. G. F. Kittel, and N. P. Molotch (2017), Quality-controlled, infilled, hourly meteorological data for the Niwot Ridge Long Term Ecological Research site (1990–2013), Available from: <http://niwot.colorado.edu/data/data/infilled-climate-data-for-c1-saddle-d1-1990-2013-hourly> (Accessed 3 June 2017)
- Jepsen, S. M., N. P. Molotch, M. W. Williams, K. E. Rittger, and J. O. Sickman (2012), Interannual variability of snowmelt in the Sierra Nevada and Rocky Mountains, United States: Examples from two alpine watersheds, *Water Resources Research*, 48(2), 1–15, doi:10.1029/2011WR011006.
- Jeton, A. E., M. D. Dettinger, and J. Smith (1996), *Potential effects of climate change on streamflow, eastern and western slopes of the Sierra Nevada, California and Nevada*, U.S. Geological Survey, Sacramento, CA.
- Jones, J. A. et al. (2012), Ecosystem Processes and Human Influences Regulate Streamflow Response to Climate Change at Long-Term Ecological Research Sites, *BioScience*, 62(4),

- 390–404, doi:10.1525/bio.2012.62.4.10.
- Knowles, J. F., A. A. Harpold, R. Cowie, M. Zeff, H. R. Barnard, S. P. Burns, P. D. Blanken, J. F. Morse, and M. W. Williams (2015), The relative contributions of alpine and subalpine ecosystems to the water balance of a mountainous, headwater catchment, *Hydrol. Process.*, 29(22), 4794–4808, doi:10.1002/hyp.10526.
- Knowles, N., M. D. Dettinger, and D. R. Cayan (2006), Trends in snowfall versus rainfall in the Western United States, *Journal of Climate*, 19(18), 4545–4559, doi:10.1175/JCLI3850.1.
- Liang, X., D. P. Lettenmaier, E. F. Wood, and S. J. Burges (1994), A simple hydrologically based model of land surface water and energy fluxes for general circulation models, *Journal of Geophysical Research: Atmospheres (1984–2012)*, 99(D7), 14415–14428, doi:10.1029/94JD00483.
- Liston, G. E., J. P. Mcfadden, M. Sturm, and R. A. Pielke (2002), Modelled changes in arctic tundra snow, energy and moisture fluxes due to increased shrubs, *Global Change Biology*, 8(1), 17–32, doi:10.1046/j.1354-1013.2001.00416.x.
- Liu, F., C. T. Hunsaker, and R. C. Bales (2012), Controls of streamflow generation in small catchments across the snow-rain transition in the Southern Sierra Nevada, California, *Hydrol. Process.*, 27(14), 1959–1972, doi:10.1002/hyp.9304.
- Liu, F., M. W. Williams, and N. Caine (2004), Source waters and flow paths in an alpine catchment, Colorado Front Range, United States, *Water Resources Research*, 40(9), 1–16, doi:10.1029/2004WR003076.
- Liu, F., R. C. Bales, M. H. Conklin, and M. E. Conrad (2008), Streamflow generation from snowmelt in semi-arid, seasonally snow-covered, forested catchments, Valles Caldera, New Mexico, *Water Resources Research*, 44(12), 3432, doi:10.1029/2007WR006728.
- Livneh, B., D. S. Pierce, T. J. Bohn, F. Munoz-Ariola, B. Nijssen, D. R. Cayan, R. Vose, and L. D. Brekki (2015), Development of a spatially comprehensive, daily hydrometeorological data set for Mexico, the conterminous U.S., and southern Canada: 1950–2013, *Nature Scientific Data*.
- Livneh, B., E. A. Rosenberg, C. Lin, and B. Nijssen (2013), A Long-Term Hydrologically Based Dataset of Land Surface Fluxes and States for the Conterminous United States: Update and Extensions, *Journal of Climate*, 26, 9384–9392, doi:10.1175/JCLI-D-12-00508.s1.
- Livneh, B., J. S. Deems, D. Schneider, J. J. Barsugli, and N. P. Molotch (2014), Filling in the gaps: Inferring spatially distributed precipitation from gauge observations over complex terrain, *Water Resources Research*, 50(11), 8589–8610, doi:10.1002/2014WR015442.
- Loudermilk, E. L., R. M. Scheller, P. J. Weisberg, J. Yang, T. E. Dilts, S. L. Karam, and C. Skinner (2013), Carbon dynamics in the future forest: the importance of long-term successional legacy and climate-fire interactions, *Global Change Biology*, 106, 3502–3515, doi:10.1111/gcb.12310.
- Luce, C. H., J. T. Abatzoglou, and Z. A. Holden (2013), The Missing Mountain Water: Slower Westerlies Decrease Orographic Enhancement in the Pacific Northwest USA, *Science*, 342(6164), 1360–1364, doi:10.1126/science.1242335.
- Luce, C. H., V. Lopez-Burgos, and Z. Holden (2014), Sensitivity of snowpack storage to precipitation and temperature using spatial and temporal analog models, *Water Resources Research*, 50(12), 9447–9462, doi:10.1002/2013WR014844.
- Lukas, J., J. J. Barsugli, N. Doesken, I. Rangwala, and K. Wolter (2014), *Climate Change in*

- Colorado, Western Water Assessment, Cooperative Institute for Research in Environmental Sciences, University of Colorado, Boulder, CO.
- Maurer, E. P., A. W. Wood, J. C. Adam, D. P. Lettenmaier, and B. Nijssen (2002), A long-term hydrologically based dataset of land surface fluxes and states for the conterminous United States, *Journal of Climate*, 15(22), 3237–3251, doi:10.1175/1520-0442(2002)015<3237:ALTHBD>2.0.CO;2.
- McNamara, J. P., D. Chandler, M. Seyfried, and S. Achet (2005), Soil moisture states, lateral flow, and streamflow generation in a semi-arid, snowmelt-driven catchment, *Hydrol. Process.*, 19(20), 4023–4038, doi:10.1002/hyp.5869.
- Meromy, L., N. P. Molotch, M. W. Williams, K. N. Musselman, and L. M. Kueppers (2015), Snowpack-climate manipulation using infrared heaters in subalpine forests of the Southern Rocky Mountains, USA, *Agricultural and Forest Meteorology*, 203, 142–157, doi:10.1016/j.agrformet.2014.12.015.
- Meybeck, M., P. Green, and C. Vörösmarty (2001), A New Typology for Mountains and Other Relief Classes: An Application to Global Continental Water Resources and Population Distribution, *Mountain Research and Development*, 21(1), 34–45, doi:https://doi.org/10.1659/0276-4741(2001)021[0034:ANTFMA]2.0.CO;2.
- Mezentsev, V. S. (1955), More on the calculation of average total evaporation, *Meteorol. Gidrol.*, 5, 24–26.
- Milly, P. C. D., J. Betancourt, M. Falkenmark, R. M. Hirsch, Z. W. Kundzewicz, D. P. Lettenmaier, and R. J. Stouffer (2008), Stationarity Is Dead: Whither Water Management? *Science*, 319(5863), 573–574, doi:10.1126/science.1151915.
- Moore, D. J., J. Hu, W. J. Sacks, D. S. Schimel, and R. K. Monson (2008), Estimating transpiration and the sensitivity of carbon uptake to water availability in a subalpine forest using a simple ecosystem process model informed by measured net CO<sub>2</sub> and H<sub>2</sub>O fluxes, *Agricultural and Forest Meteorology*, 148(10), 1467–1477, doi:10.1016/j.agrformet.2008.04.013.
- Morin, X., D. Viner, and I. Chuine (2008), Tree species range shifts at a continental scale: new predictive insights from a process-based model, *Journal of Ecology*, 96(4), 784–794, doi:10.1111/j.1365-2745.2008.01369.x.
- Mote, P. W., A. F. Hamlet, M. P. Clark, and D. P. Lettenmaier (2005), Declining Mountain Snowpack in Western North America, *Bull. Amer. Meteor. Soc.*, 86(1), 39–49, doi:10.1175/BAMS-86-1-39.
- Musselman, K. N., M. P. Clark, C. Liu, K. Ikeda, and R. M. Rasmussen (2017), Slower snowmelt in a warmer world, *Nature Climate change*, 7(3), 214–219, doi:10.1038/nclimate3225.
- Nash, J. E., and J. V. Sutcliffe (1970), River flow forecasting through conceptual models part I—A discussion of principles, *Journal of Hydrology*, 10, 282–290, doi:https://doi.org/10.1016/0022-1694(70)90255-6.
- Newman, A. J. et al. (2015), Development of a large-sample watershed-scale hydrometeorological data set for the contiguous USA: data set characteristics and assessment of regional variability in hydrologic model performance, *Hydrol. Earth Syst. Sci.*, 19(1), 209–223, doi:10.5194/hess-19-209-2015.
- Nolin, A. W., and C. Daly (2006), Mapping “At Risk” Snow in the Pacific Northwest, *J. Hydrometeor.*, 7, 1164–1171, doi:https://doi.org/10.1175/JHM543.1.

- Ol'Dekop, E. M. (1911), On evaporation from the surface of river basins, *Trans. Meteorol. Obs. Univ. Tartu*, 4, 200.
- Öztürk, M., N. K. Coptý, and A. K. Saysel (2013), Modeling the impact of land use change on the hydrology of a rural watershed, *Journal of Hydrology*, 497(C), 97–109, doi:10.1016/j.jhydrol.2013.05.022.
- Perktold, J., S. Seabold, and J. Taylor (2016), StatsModels, *statsmodels.org*. Available from: <http://www.statsmodels.org/> (Accessed 3 June 2016)
- Pike, J. G. (1964), The estimation of annual run-off from meteorological data in a tropical climate, *Journal of Hydrology*, 2(2), 116–123, doi:10.1016/0022-1694(64)90022-8.
- Rasmussen, R. M. et al. (2011), High-Resolution Coupled Climate Runoff Simulations of Seasonal Snowfall over Colorado: A Process Study of Current and Warmer Climate, *Journal of Climate*, 24(12), 3015–3048, doi:10.1175/2010JCLI3985.1.
- Richardson, J. J., L. M. Moskal, and S.-H. Kim (2009), Modeling approaches to estimate effective leaf area index from aerial discrete-return LIDAR, *Agricultural and Forest Meteorology*, 149(6-7), 1152–1160, doi:10.1016/j.agrformet.2009.02.007.
- Rood, S. B., G. M. Samuelson, J. K. Weber, and K. A. Wywrot (2005), Twentieth-century decline in streamflows from the hydrographic apex of North America, *Journal of Hydrology*, 306(1-4), 215–233, doi:10.1016/j.jhydrol.2004.09.010.
- Rother, M. T., and T. T. Veblen (2016), Limited conifer regeneration following wildfires in dry ponderosa pine forests of the Colorado Front Range, *Ecosphere*, 7(12), 1–17, doi:10.1002/ecs2.1594.
- Saksa, P. C., M. H. Conklin, J. J. Battles, C. L. Tague, and R. C. Bales (2017), Forest thinning impacts on the water balance of Sierra Nevada mixed-conifer headwater basins, *Water Resources Research*, 53(7), 5364–5381, doi:10.1002/2016WR019240.
- Scheller, R. M., and D. J. Mladenoff (2004), A forest growth and biomass module for a landscape simulation model, LANDIS: design, validation, and application, *Ecological Modelling*, 180(1), 211–229, doi:10.1016/j.ecolmodel.2004.01.022.
- Scheller, R. M., J. B. Domingo, B. R. Sturtevant, J. S. Williams, A. Rudy, E. J. Gustafson, and D. J. Mladenoff (2007), Design, development, and application of LANDIS-II, a spatial landscape simulation model with flexible temporal and spatial resolution, *Ecological Modelling*, 201(3-4), 409–419, doi:10.1016/j.ecolmodel.2006.10.009.
- Schimel, D. S., T. G. F. Kittel, S. Running, R. Monson, A. Turnipseed, and D. Anderson (2002), Carbon sequestration studied in western U.S. mountains, *Eos, Transactions American Geophysical Union*, 83(40), 445–449, doi:10.1029/2002EO000314.
- Schreiber, P. (1904), Über die Beziehungen zwischen dem Niederschlag und der Wasserführung der Flüsse, *Z. Meteorol.*, 21, 441–452.
- Serra-Diaz, J. M., R. M. Scheller, A. D. Syphard, and J. Franklin (2015), Disturbance and climate microrefugia mediate tree range shifts during climate change, *Landscape Ecology*, 30(6), 1–15, doi:10.1007/s10980-015-0173-9.
- Serreze, M. C., M. P. Clark, R. L. Armstrong, D. A. McGinnis, and R. S. Pulwarty (1999), Characteristics of the western United States snowpack from snowpack telemetry(SNOTEL) data, *Water Resources Research*, 35(7), 2145–2160, doi:10.1029/1999WR900090.
- Sharif, H. O., W. T. Crow, N. L. Miller, and E. F. Wood (2007), Multidecadal High-resolution Hydrologic Modeling of the Arkansas/Red River Basin, *J. Hydrometeorol.*, 8(5), 1111–1127, doi:10.1175/JHM622.1.

- Shuttleworth, W. J. (1993), Evaporation, in *Handbook of Hydrology*, edited by D. R. Maidment, pp. 4.1–4.53, New York.
- Sivapalan, M., M. A. Yaeger, C. J. Harman, X. Xu, and P. A. Troch (2011), Functional model of water balance variability at the catchment scale: 1. Evidence of hydrologic similarity and space-time symmetry, *Water Resources Research*, 47(2), 411–18, doi:10.1029/2010WR009568.
- Soil Survey Staff (2016), Web Soil Survey, *National Resource Conservation Service, United States Department of Agriculture*. Available from: <https://websoilsurvey.sc.egov.usda.gov/> (Accessed 10 December 2016)
- Son, K. (2015), The importance of sub-watershed variability for predicting ecohydrologic responses to inter- annual climate variability and climate warming in California’s Sierra Nevada watersheds (Doctoral dissertation), 1–183 pp. University of California Santa Barbara, Santa Barbara, CA.
- St Clair, J., S. Moon, W. S. Holbrook, J. T. Perron, C. S. Riebe, S. J. Martel, B. Carr, C. Harman, K. Singha, and D. D. Richter (2015), Geophysical imaging reveals topographic stress control of bedrock weathering, *Science*, 350(6260), 534–538, doi:10.1126/science.aab2210.
- Stewart, I. T. (2009), Changes in snowpack and snowmelt runoff for key mountain regions, *Hydrol. Process.*, 23(1), 78–94, doi:10.1002/hyp.7128.
- Stewart, I. T., D. R. Cayan, and M. D. Dettinger (2004), Changes in snowmelt runoff timing in western North America under a “business as usual” climate change scenario, *Climatic Change*, 62(1-3), 217–232, doi:10.1023/B:CLIM.0000013702.22656.e8.
- Stewart, I. T., D. R. Cayan, and M. D. Dettinger (2005), Changes toward Earlier Streamflow Timing across Western North America, *Journal of Climate*, 18(8), 1136–1155, doi:10.1175/JCLI3321.1.
- Sturm, M., M. A. Goldstein, and C. Parr (2017), Water and life from snow: A trillion dollar science question, *Water Resources Research*, 1–27, doi:10.1002/2017WR020840.
- Tabler, R. D. (2003), *Controlling Blowing and Drifting Snow with Snow Fences and Road Design*, National Cooperative Highway Research Program Transportation Research Board of the National Academies, Project 20-7(147).
- Tague, C. L., and G. E. Grant (2009), Groundwater dynamics mediate low-flow response to global warming in snow-dominated alpine regions, *Water Resources Research*, 45(7), 181, doi:10.1029/2008WR007179.
- Tague, C. L., and H. Peng (2013), The sensitivity of forest water use to the timing of precipitation and snowmelt recharge in the California Sierra: Implications for a warming climate, *J. Geophys. Res. Biogeosci.*, 118(2), 875–887, doi:10.1002/jgrg.20073.
- Tague, C. L., and L. E. Band (2004), RHESys: regional hydro-ecologic simulation system-an object-oriented approach to spatially distributed modeling of carbon, water, and nutrient cycling, *Earth Interactions*, 8(19), 1–42, doi:https://doi.org/10.1175/1087-3562(2004)8<1:RRHSSO>2.0.CO;2.
- Tague, C. L., G. E. Grant, M. Farrell, J. Choate, and A. Jefferson (2007), Deep groundwater mediates streamflow response to climate warming in the Oregon Cascades, *Climatic Change*, 86(1-2), 189–210, doi:10.1007/s10584-007-9294-8.
- Tague, C. L., J. S. Choate, and G. E. Grant (2013), Parameterizing sub-surface drainage with geology to improve modeling streamflow responses to climate in data limited environments, *Hydrol. Earth Syst. Sci.*, 17(1), 341–354.

- Tague, C. L., K. Heyn, and L. Christensen (2009), Topographic controls on spatial patterns of conifer transpiration and net primary productivity under climate warming in mountain ecosystems, *Ecohydrol.*, 554(October), 541–554, doi:<http://dx.doi.org/10.1002/eco.88>.
- Thornton, P. E., S. W. Running, and M. A. White (1997), Generating surfaces of daily meteorological variables over large regions of complex terrain, *Journal of Hydrology*, 190(3-4), 214–251, doi:10.1016/S0022-1694(96)03128-9.
- Troch, P. A., T. Lahmers, A. Meira, R. Mukherjee, J. W. Pedersen, T. Roy, and R. Valdés-Pineda (2015), Catchment coevolution: A useful framework for improving predictions of hydrological change? *Water Resources Research*, 51(7), 4903–4922, doi:10.1002/2015WR017032.
- Trujillo, E., and N. P. Molotch (2014), Snowpack regimes of the Western United States, *Water Resources Research*, 50(7), 5611–5623, doi:10.1002/2013WR014753.
- Turc, L. (1955), Le bilan d’eau des sols. Relations entre le précipitations, l’évapotranspiration potentielle, *Ann. Agron. Serie A*, 5, 491–595.
- van Oldenborgh, G. J., M. Collins, J. Arblaster, J. H. Christensen, J. Marotzke, S. B. Power, M. Rummukainen, and T. Zhou (2013), Annex I, in *Climate Change 2013*, edited by T. F. Stocker, D. Qin, G. K. Plattner, M. Tignor, S. K. Allen, J. Boschung, A. Nauels, Y. Xia, V. Bex, and P. M. Midgley, pp. 1–84, Cambridge University Press, Cambridge, United Kingdom and New York, NY, USA.
- Vano, J. A., and D. P. Lettenmaier (2012), Hydrologic Sensitivities of Colorado River Runoff to Changes in Precipitation and Temperature, *J. Hydrometeor.*, 13(3), 932–949, doi:10.1175/JHM-D-11-069.1.
- Vano, J. A., B. Nijssen, and D. P. Lettenmaier (2015), Seasonal hydrologic responses to climate change in the Pacific Northwest, *Water Resources Research*, 51(4), 1959–1976, doi:10.1002/2014WR015909.
- Viviroli, D., H. H. Dürr, B. Messerli, M. Meybeck, and R. Weingartner (2007), Mountains of the world, water towers for humanity: Typology, mapping, and global significance, *Water Resources Research*, 43(7), 1–13, doi:10.1029/2006WR005653.
- Vörösmarty, C. J., C. Lévêque, C. Revenga, R. Bos, C. Caudill, and J. Chilton (2005), Fresh Water, in *Ecosystems and Human Well-being Current State and Trends*, BSI British Standards, London.
- Wagener, T., M. Sivapalan, P. Troch, and R. Woods (2007), Catchment Classification and Hydrologic Similarity, *Geography Compass*, 1(4), 901–931, doi:10.1111/j.1749-8198.2007.00039.x.
- White, J. D., S. W. Running, and R. Nemani (1997), Measurement and remote sensing of LAI in Rocky Mountain montane ecosystems, *Can. J. For. Res.*, doi:<https://doi.org/10.1139/x97-142>.
- Wilcox, B. P., B. D. Newman, D. Brandes, D. W. Davenport, and K. Reid (1997), Runoff from a semiarid Ponderosa pine hillslope in New Mexico, *Water Resources Research*, 33(10), 2301–2314, doi:10.1029/97WR01691.
- Williams, M. W., R. T. Barnes, J. N. Parman, M. Freppaz, and E. Hood (2011), Stream Water Chemistry along an Elevational Gradient from the Continental Divide to the Foothills of the Rocky Mountains, *Vadose Zone Journal*, 10(3), 900, doi:10.2136/vzj2010.0131.
- Winchell, T. S., D. M. Barnard, R. K. Monson, S. P. Burns, and N. P. Molotch (2016), Earlier snowmelt reduces atmospheric carbon uptake in midlatitude subalpine forests, *Geophysical Research Letters*, 43(15), 8160–8168, doi:10.1002/2016GL069769.

- Winstral, A., K. Elder, and R. E. Davis (2002), Spatial snow modeling of wind-redistributed snow using terrain-based parameters, *J. Hydrometeorol*, 3(5), 524–538, doi:10.1175/1525-7541(2002)003<0524:SSMOWR>2.0.CO;2.
- Xia, Y. et al. (2012), Continental-scale water and energy flux analysis and validation for the North American Land Data Assimilation System project phase 2 (NLDAS-2): 1. Intercomparison and application of model products, *JGR*, 117(D3), D03109, doi:10.1029/2011JD016048.
- Yang, H., D. Yang, Z. Lei, and F. Sun (2008), New analytical derivation of the mean annual water-energy balance equation, *Water Resources Research*, 44(3), 1–9, doi:10.1029/2007WR006135.
- Zhang, L., K. Hickel, W. R. Dawes, F. H. S. Chiew, A. W. Western, and P. R. Briggs (2004), A rational function approach for estimating mean annual evapotranspiration, *Water Resources Research*, 40(2), 1–14, doi:10.1029/2003WR002710.
- Zhang, L., W. R. Dawes, and G. R. Walker (2001), Response of mean annual evapotranspiration to vegetation changes at catchment scale, *Water Resources Research*, 37(3), 701–708, doi:10.1029/2000WR900325.
- Zhou, S., B. Yu, Y. Huang, and G. Wang (2015), The complementary relationship and generation of the Budyko functions, *Geophysical Research Letters*, 42(6), 1781–1790, doi:10.1002/2015GL063511.

## Appendix A: Chapter 2 Supporting Information

### A.1 Calculation of Plant Available Water Storage

For each of the fifteen plant available water storage (PAWS) ensemble members, PAWS was computed as follows. PAWS was computed for each parameter set by first computing the soil column porosity as

$$\phi_{rd} = \int_0^{z_{rd}} \phi_0 e^{\frac{-z_{rd}}{p}} \quad (\text{A.1})$$

where  $\phi_{rd}$  is the soil column porosity integrated from the surface to the bottom of the root zone,  $z_{rd}$  is the depth of the root zone,  $\phi_0$  is the porosity at the surface, and  $p$  is the decay of  $\phi_0$  with depth [Tague and Band, 2004]. Soil water content at the wilting point,  $\theta_{wp}$ , was computed as

$$\theta_{wp} = \phi_{rd} \left( \frac{|\psi_{ae}|}{150} \right)^{\frac{1}{b}} \quad (\text{A.2})$$

where  $\psi_{ae}$  is the air entry pressure, 150 is the pressure head in meters, and  $b$  is the pore size index [Dingman, 2002]. Soil water content at field capacity,  $\theta_{fc}$ , was computed as

$$\theta_{fc} = \phi_{rd} \left( \frac{|\psi_{ae}|}{3.4} \right)^{\frac{1}{b}} \quad (\text{A.3})$$

where 3.4 is the pressure head in meters [Dingman, 2002]. PAWS,  $\theta_{PAWS}$ , was then computed as

$$\theta_{PAWS} = \theta_{fc} - \theta_{wp} \quad (\text{A.4})$$

# Appendix B: Chapter 4 Supporting Information<sup>1</sup>

## B.1 Introduction

In this document, we provide expanded tables and figures documenting relationships summarized in the article text.

## B.2 Snow Fall Fraction Calculation

We computed long-term snowfall fraction ( $Sf_j$ ) for each grid cell such that:

$$Sf_j = \frac{\sum P_{jt} C_{jt}}{\sum P_{jt}} \quad (\text{B.1})$$

where  $C_{jt}$  is the proportion of the day's precipitation that falls as snow. Similar to Hamlet et al. [2005],  $C_{jt}$  is determined as:

$$\begin{aligned} C_{jt} &= 1 & T_{max_{jt}} < 0 \text{ }^\circ\text{C} \\ C_{jt} &= 0 & T_{min_{jt}} > 0 \text{ }^\circ\text{C} \\ C_{jt} &= \frac{0 - T_{min_{ji}}}{|T_{max_{ji}} - T_{min_{ji}}|} & T_{max_{jt}} \geq 0 \text{ }^\circ\text{C} \geq T_{min} \end{aligned} \quad (\text{B.2})$$

where 0 °C is the threshold between liquid and solid precipitation for pure water,  $T_{max}$  is daily maximum temperature and  $T_{min}$  is daily minimum temperature. We chose 0 °C because it is the melting point of pure water. We recognize that this threshold varies around 0 °C and, as a result,

---

<sup>1</sup> Published as: Barnhart, T. B., N. P. Molotch, B. Livneh, A. A. Harpold, J. F. Knowles, and D. Schneider (2016), Snowmelt rate dictates streamflow, *Geophysical Research Letters*, 43(15), 8006–8016, doi:10.1002/2016GL069690. Reproduced here with the permission of John Wiley and Sons: License Number 4271020375886.

we computed snowfall fractions across a range of threshold temperature from -2 to 2 °C to assess if our results are sensitive to the threshold temperature selected.

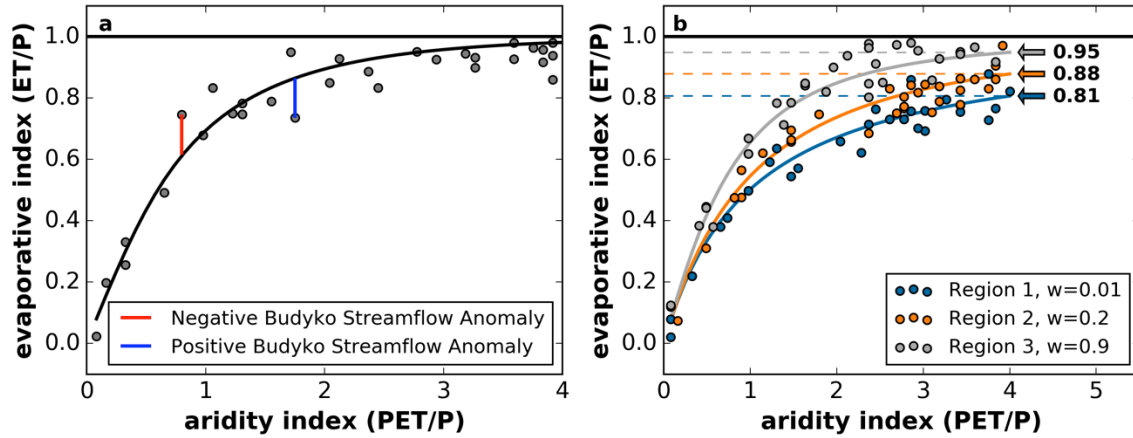


Figure B.1: a) Conceptual diagram showing the hypothetical relationship between aridity and evaporative indices with a Budyko-type curve fit to the data. Points that lie below the curve (black line) have positive BSA values (e.g. vertical blue line) and over-produce streamflow relative to the Budyko-type equation. Points that plot above the curve have negative BSA values (e.g. vertical red line) and under-produce streamflow relative to the Budyko-type equation. b) Conceptual diagram illustrating the evaporative index (y-axis) asymptotes from Zhang et al. [2001] fitted Budyko-type equations for three hypothetical regions (colored arrows).

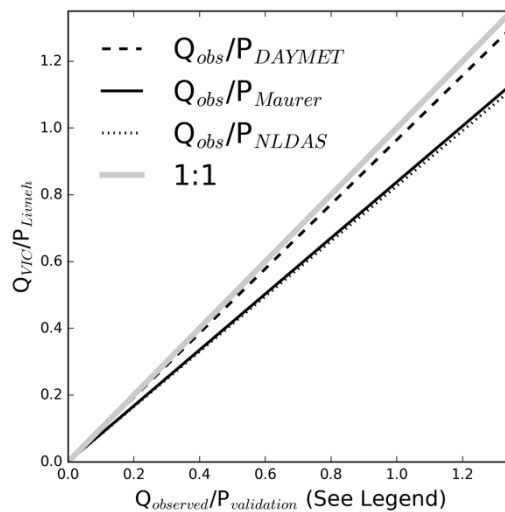


Figure B.2: Regressions of streamflow efficiencies from observed Q and the three gridded precipitation products from Newman et al. [2015] versus VIC simulated streamflow efficiencies from the Livneh et al. [2015] hydrometeorological data set used for this study. The same x-axis is used for each independent variable shown in the legend.

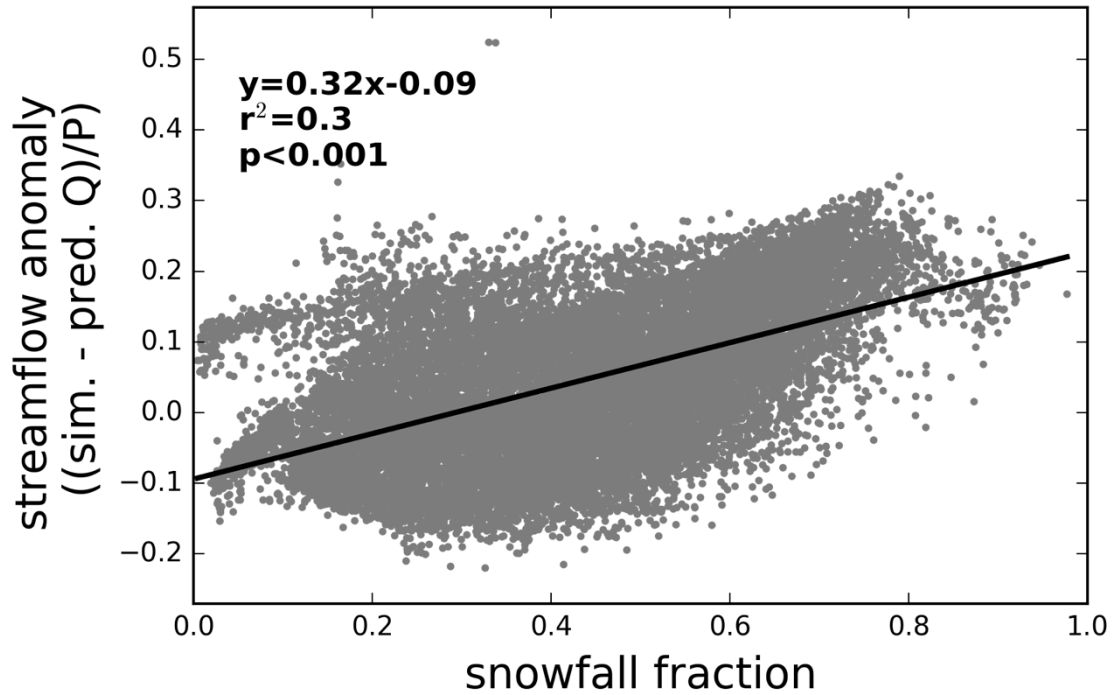


Figure B.3: Regressions of mean BSA and snowfall fraction.

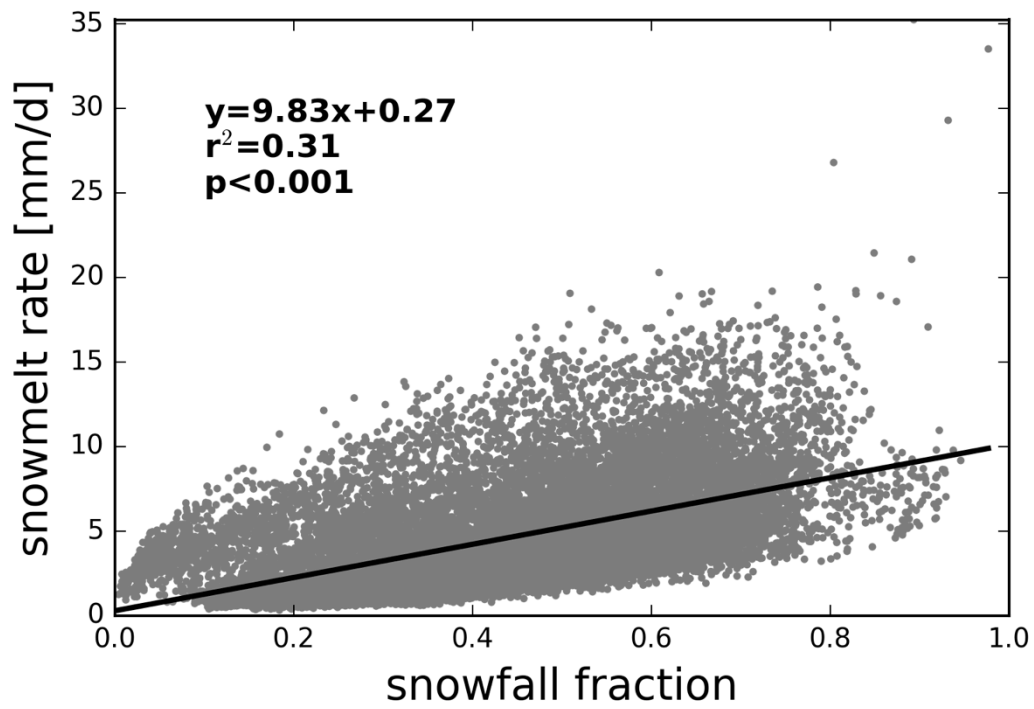


Figure B.4: Collinearity of snowfall fraction and snowmelt rate.

Table B.1: Statistical data and fitting parameters, if applicable, for the ensemble of nine Budyko-type equations.

Equation	$r^2$	RMSE	Fitting Parameter
Schreiber, 1904	0.8	0.1	-
Ol'Dekop, 1911	0.47	0.17	-
Turc, 1955; Pike, 1964	0.65	0.13	-
Budyko, 1974	0.68	0.13	-
Mezentsev, 1955; Choudhury, 1999; Yang et al., 2008	0.78	0.11	1.46
Fu, 1981; Zhang et al., 2004	0.78	0.11	2.17
Zhang et al., 2001	0.8	0.1	0.56
Sharif et al., 2007	0.65	0.14	-
Zhou et al., 2015	0.7	0.13	1.59

Table B.2: BSA – snowmelt rate relationship statistics for each Budyko-type equation.

Equation	Slope	Intercept	p	$r^2$
Schreiber, 1904	0.015	-0.029	<0.001	0.27
Ol'Dekop, 1911	0.021	0.035	<0.001	0.36
Turc, 1955; Pike, 1964	0.019	0.002	<0.001	0.35
Budyko, 1974	0.018	0.002	<0.001	0.32
Mezentsev, 1955; Choudhury, 1999; Yang et al., 2008	0.022	-0.09	<0.001	0.44
Fu, 1981; Zhang et al., 2004	0.023	-0.091	<0.001	0.45
Zhang et al., 2001	0.021	-0.087	<0.001	0.4
Sharif et al., 2007	0.032	-0.109	<0.001	0.62
Zhou et al., 2015	0.03	-0.146	<0.001	0.59

Table B.3: BSA – baseflow efficiency relationship statistics for each Budyko-type equation.

Equation	Slope	Intercept	p	r <sup>2</sup>
Schreiber, 1904	0.422	-0.049	<0.001	0.45
Ol'Dekop, 1911	0.553	0.01	<0.001	0.57
Turc, 1955; Pike, 1964	0.517	-0.021	<0.001	0.57
Budyko, 1974	0.482	-0.02	<0.001	0.52
Mezentsev, 1955; Choudhury, 1999; Yang et al., 2008	0.578	-0.112	<0.001	0.66
Fu, 1981; Zhang et al., 2004	0.585	-0.114	<0.001	0.67
Zhang et al., 2001	0.538	-0.109	<0.001	0.62
Sharif et al., 2007	0.803	-0.133	<0.001	0.84
Zhou et al., 2015	0.758	-0.17	<0.001	0.82

Table B.4: BSA – snowmelt rate relationship statistics for each equation and ecoregion. Ecoregion codes are the same as in Figure 4.1.

Equation	Ecoregion Code	$r^2$	p	Intercept	Slope
Budyko, 1974	1	0.042	<0.001	0.119	0.004
	2	0.657	<0.001	-0.093	0.02
	3	0.086	<0.001	0.055	0.011
	4	0.407	<0.001	0.1	0.016
	5	0.326	<0.001	-0.025	0.023
	6	0.531	<0.001	-0.083	0.041
	7	0.447	<0.001	-0.046	0.034
	8	0.459	<0.001	-0.043	0.028
	9	0.009	<0.001	0.098	0.003
	10	0.418	<0.001	0.037	0.015
Fu, 1981; Zhang et al., 2004	1	0.237	<0.001	0.04	0.008
	2	0.759	<0.001	-0.132	0.021
	3	0.136	<0.001	-0.037	0.014
	4	0.508	<0.001	0.011	0.019
	5	0.327	<0.001	-0.111	0.025
	6	0.556	<0.001	-0.174	0.045
	7	0.49	<0.001	-0.136	0.038
	8	0.526	<0.001	-0.141	0.032
	9	0.067	<0.001	0.001	0.007
	10	0.553	<0.001	-0.056	0.02
Mezentsev, 1955; Choudhury, 1999; Yang et al., 2008	1	0.243	<0.001	0.04	0.008
	2	0.764	<0.001	-0.132	0.021
	3	0.119	<0.001	-0.032	0.013
	4	0.512	<0.001	0.011	0.019
	5	0.29	<0.001	-0.105	0.023
	6	0.536	<0.001	-0.17	0.043
	7	0.475	<0.001	-0.133	0.037
	8	0.519	<0.001	-0.142	0.032
	9	0.063	<0.001	0.001	0.007
	10	0.561	<0.001	-0.06	0.021

Table B.4 continued.

Equation	Ecoregion Code	r <sup>2</sup>	p	Intercept	Slope
Ol'Dekop, 1911	1	0.017	<0.001	0.166	0.003
	2	0.553	<0.001	-0.045	0.019
	3	0.218	<0.001	0.063	0.018
	4	0.413	<0.001	0.142	0.019
	5	0.547	<0.001	-0.024	0.036
	6	0.656	<0.001	-0.075	0.053
	7	0.557	<0.001	-0.025	0.042
	8	0.533	<0.001	-0.006	0.031
	9	0.045	<0.001	0.138	0.005
	10	0.336	<0.001	0.111	0.013
Schreiber, 1904	1	0.079	<0.001	0.075	0.005
	2	0.733	<0.001	-0.136	0.021
	3	0.011	<0.001	0.046	0.004
	4	0.377	<0.001	0.06	0.014
	5	0.099	<0.001	-0.027	0.012
	6	0.37	<0.001	-0.092	0.031
	7	0.323	<0.001	-0.067	0.027
	8	0.387	<0.001	-0.08	0.025
	9	0	0.472	0.059	0
	10	0.479	<0.001	-0.032	0.017
Sharif et al., 2007	1	0.569	<0.001	0.059	0.015
	2	0.808	<0.001	-0.049	0.022
	3	0.329	<0.001	-0.069	0.024
	4	0.582	<0.001	0.006	0.027
	5	0.501	<0.001	-0.143	0.037
	6	0.668	<0.001	-0.203	0.058
	7	0.614	<0.001	-0.156	0.049
	8	0.644	<0.001	-0.163	0.042
	9	0.309	<0.001	-0.016	0.017
	10	0.663	<0.001	-0.048	0.029

Table B.4 continued.

Equation	Ecoregion Code	r <sup>2</sup>	p	Intercept	Slope
Turc, 1955; Pike, 1964	1	0.049	<0.001	0.125	0.004
	2	0.648	<0.001	-0.081	0.02
	3	0.134	<0.001	0.047	0.013
	4	0.418	<0.001	0.104	0.017
	5	0.416	<0.001	-0.035	0.028
	6	0.584	<0.001	-0.091	0.046
	7	0.491	<0.001	-0.049	0.037
	8	0.488	<0.001	-0.04	0.029
	9	0.02	<0.001	0.101	0.004
	10	0.415	<0.001	0.049	0.015
Zhang et al., 2001	1	0.218	<0.001	0.036	0.008
	2	0.767	<0.001	-0.144	0.021
	3	0.075	<0.001	-0.023	0.01
	4	0.492	<0.001	0.011	0.018
	5	0.213	<0.001	-0.094	0.019
	6	0.484	<0.001	-0.161	0.04
	7	0.43	<0.001	-0.128	0.034
	8	0.486	<0.001	-0.139	0.03
	9	0.036	<0.001	0.002	0.005
	10	0.552	<0.001	-0.068	0.02
Zhou et al., 2015	1	0.56	<0.001	0.013	0.014
	2	0.812	<0.001	-0.104	0.022
	3	0.268	<0.001	-0.099	0.021
	4	0.582	<0.001	-0.035	0.026
	5	0.425	<0.001	-0.171	0.033
	6	0.63	<0.001	-0.234	0.054
	7	0.579	<0.001	-0.19	0.046
	8	0.62	<0.001	-0.202	0.04
	9	0.251	<0.001	-0.056	0.015
	10	0.657	<0.001	-0.098	0.028

Table B.5: Ecoregion mean snowmelt rates and Zhang et al. [2001] fitted Budyko-type curve asymptotes. Ecoregion codes are the same as in Figure 4.1.

<b>Ecoregion Code</b>	<b>Fitting Parameter (w)</b>	<b>Asymptote</b>	<b>Mean Snowmelt Rate [mm/d]</b>
1	-0.03	0.74	9.07
2	0.3	0.76	8.18
3	0.48	0.91	3.58
4	0.07	0.86	5.48
5	0.87	0.97	2.85
6	1.06	0.97	2.47
7	0.76	0.96	2.89
8	0.38	0.89	5.93
9	0.38	0.9	5.57
10	0.13	0.7	7.47

Table B.6: Snowfall fraction – BSA relationship statistics for each Budyko-type equation.

<b>Equation</b>	<b>Slope</b>	<b>Intercept</b>	<b>p</b>	<b>r<sup>2</sup></b>
Schreiber, 1904	0.244	-0.064	<0.001	0.219
Ol'Dekop, 1911	0.361	-0.027	<0.001	0.357
Turc, 1955; Pike, 1964	0.321	-0.048	<0.001	0.317
Budyko, 1974	0.299	-0.046	<0.001	0.294
Mezentsev, 1955; Choudhury, 1999; Yang et al., 2008	0.31	-0.122	<0.001	0.278
Fu, 1981; Zhang et al., 2004	0.317	-0.125	<0.001	0.287
Zhang et al., 2001	0.289	-0.118	<0.001	0.258
Sharif et al., 2007	0.39	-0.13	<0.001	0.29
Zhou et al., 2015	0.366	-0.166	<0.001	0.279